Title

Measuring the Metabolic Changes that Occur with Prostate Cancer Progression Using HR-MAS and Hyperpolarized ^{13}C MR Spectroscopy

Author

Albers, Mark J.

Publication Date

2008-04-04

Peer reviewed|Thesis/dissertation

Measuring the Metabolic Changes that Occur with Prostate Cancer Progression Using HR-MAS and Hyperpolarized ^{13}C MR Spectroscopy

by

Mark J. Albers

DISSERTATION

Submitted in partial satisfaction of the requirements for the degree of

DOCTOR OF PHILOSOPHY

in

Bioengineering

in the

GRADUATE DIVISION

of the

UNIVERSITY OF CALIFORNIA, SAN FRANCISCO

AND

UNIVERSITY OF CALIFORNIA, BERKELEY

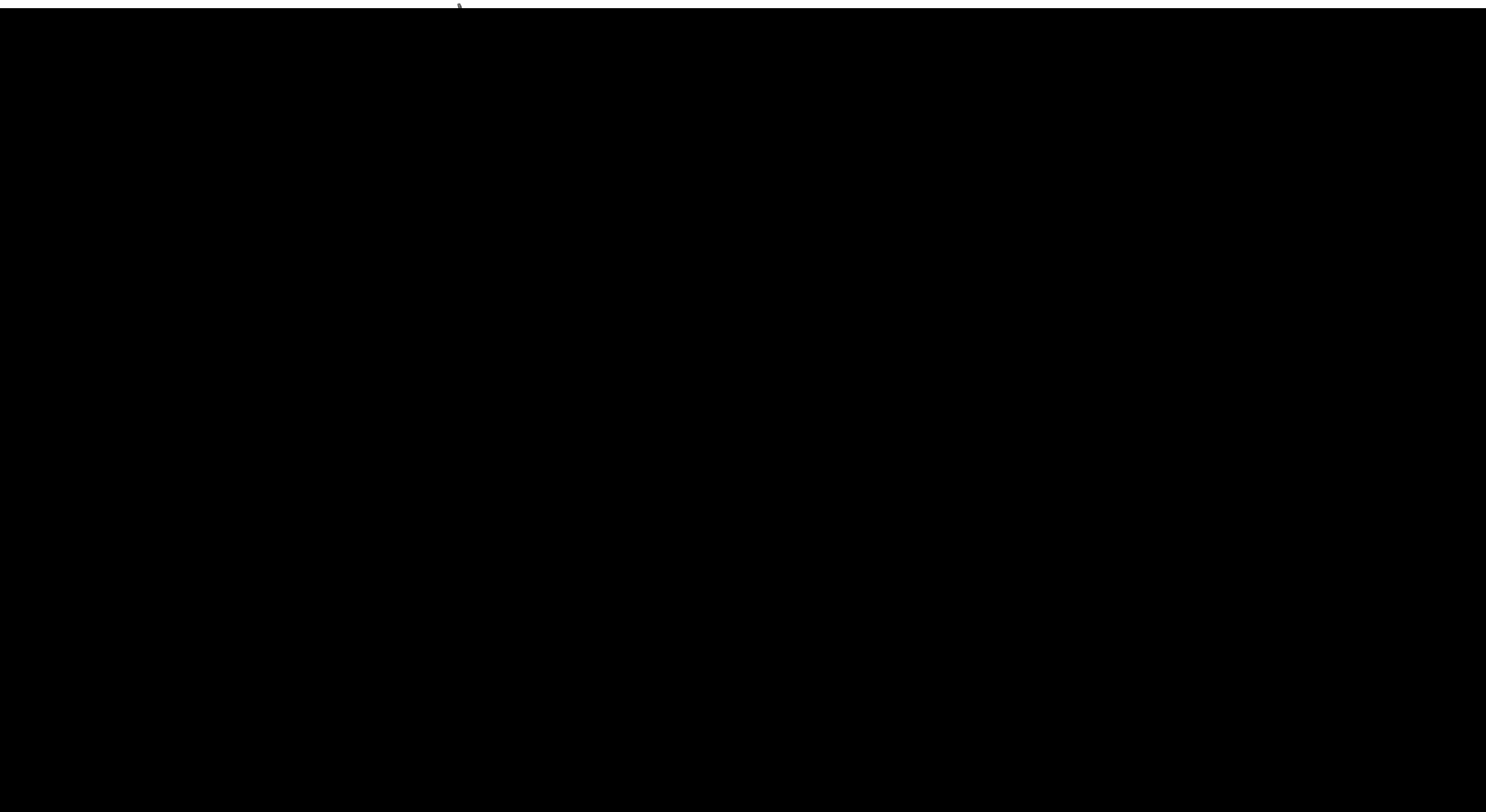

Dedicated to:

Cathleen Enrqiuez, my rock

and

Urban and Violet Albers, my grandparents

and

the memory of Tom Raidy, a dear friend and honorable scientist

Acknowledgements

I would like to thank my advisor, Professor John Kurhanewicz, for giving me the opportunity to work in his lab and for supporting me during my graduate research. I also want to thank the other members of his lab and the Prostate Imaging Group for their support during the last several years. Namely, Robert Bok, Mark Swanson, and Sue Noworolski for their helpful discussions on the latest prostate cancer biology and imaging research. I would like to acknowledge Carissa Santos, Akpene Gbegnon, and Tom Butler for their hard work and assistance in the lab. Without their help, my research would have taken much more time. I especially want to thank May-Britt Tessem and Samson Jarso for sharing their experiences with me while they were in John's lab and for their enthusiasm about our research.

Outside of John's lab, I want to thank Professors Steve Conolly and John Gross for taking the time to mentor me through my graduate research and to critic my thesis. The knowledge I gained from them was essential for my success.

I am extremely grateful to Helene Ratiney and Herald Rabeson for a productive and enjoyable research collaboration on the QUEST fitting algorithm, which spans the Atlantic Ocean and was not directly included in my thesis. Nonetheless, it was and continues to be a centerpiece of my research. For several years, Helene has spent enormous amounts of her spare time working with me on this project, without hesitation.

I want to recognize Professor Donna Peehl from Stanford Medical Center and Rosie Nolley, Larry Hooser, and Robert Sellers from her lab for welcoming me into Donna's lab and collaborating with us on the primary cell culture and tissue culture projects. I truly admire Donna's wonderful attitude and expertise in prostate cancer research and primary cultures. Her commitment to our collaboration and her adventurous, yet well-planned research style ensured that we produced useful results. I

also want to thank Yakir Levin from Stanford Medical Center for his willingness to work with us on a challenging cell culture project.

Of course, none of our NMR experiments would have happened without the unwavering support of Bao Nguyen from Varian, Inc. and Arvin Moser from Advanced Chemistry Development. Bao's delightful attitude, focused work ethic, and balanced approach to life are truly inspirational. Not to mention, his assistance was essential to the success of the ERETIC project and to the day-to-day operation of the HR-MAS probe. Arvin was equally as enjoyable to work with and his knowledge of ACD's software an important reference. I could count on Arvin for solutions to our problems, not excuses. I also want to thank Mark Dixon from Varian for his helpful discussions on ERETIC and his guidance in using VNMRJ.

The hyperpolarization experiments would have never happened at UCSF without the hard word and dedication of Ralph Hurd, Susan Kohler, and Yi-Fen Yen from GE Healthcare, whose tireless efforts made the project a reality. In addition, I want to recognize all the collaborators at UCSF that also made a significant contribution to the hyperpolarization project, John Kurhanewicz, Robert Bok, Vickie Zhang, Ilwoo Park, Charles H. Cunningham, Albert P. Chen, Matt L. Zierhut, Sarah J. Nelson, Daniel B. Vigneron, Pieter Pels, Lucas Carvajal, Ying Lu, and Helena Gurascier. I especially want to acknowledge Robert Bok for the countless hours he spent surgically preparing all the animals included in the study and performing all the histological analysis. I also want to recognize James Tropp, Paul Calderon, Jan Henrik Ardenkjaer-Larsen, Jan Wolber, Hubert Dirven, Andreas Gram, and Jonathan Murray from GE Healthcare for their support of this project.

Going back to the beginning of my graduate career. I want to thank Tom Raidy, Stefan Bluml, Catherine Rafter, and Tom Mantei for their encouragement as I

transitioned back into academia. Also, I want to thank Carmen Taylor, Suchandrima Banerjee, Tobias Henning, Jason Crane, and Mike Wendland from UCSF, Pierre-Gilles Henry and Melissa Terpstra from the University of Minnesota, and Renty Franklin and Leslie Costello from the University of Maryland for their helpful and informative discussions on topics that were pertinent to my research. I am grateful that they took the time to describe important techniques to me even though they had nothing to gain from it.

Last but certainly not least, I want to thank the people in my personal life whose support was enormously appreciated. I am eternally grateful to Cathleen Enriquez who was with me day-in and day-out, on the good days and the bad ones. I would not have made it without her. I want to thank my family, especially my grandparents, Urban and Violet Albers, who have supported me my entire life and have always been concerned about my well-being. I also want to thank my friends in the bay area, Denny Lau, Diana and Ted Fong, and Aashish and Charu Malhotra, who made it possible for me to have fun while I was working on my Ph.D.

Measuring the Metabolic Changes that Occur with Prostate Cancer Progression Using HR-MAS and Hyperpolarized ^{13}C MR Spectroscopy

by

Mark J. Albers

Abstract

The accurate detection and characterization of prostate cancer remains a major problem for the clinical management of individual prostate cancer patients and for monitoring their response to therapy. In-vivo ^{1}H Magnetic Resonance Spectroscopic Imaging (MRSI) has demonstrated that secretory prostatic tissue contains uniquely high levels of citrate, which decrease as prostate cancer evolves. It is unclear whether the decrease is caused by an increase in fatty acid biosynthesis, an increase in citrate oxidation in the citric acid cycle, an increase in glycolytic lactate production, or a combination of these mechanisms. In this project, ^{13}C labeling protocols and measurement techniques were developed to simultaneously interrogate these pathways in primary cultured prostate epithelial cells and tissue slice cultures as well as transgenic mice. The primary cultures were labeled using thermally polarized ^{13}C-3 pyruvate and analyzed using High Resolution – Magic Angle Spinning (HR-MAS) spectroscopy. Subsequently, the exceptional 80,000-fold enhancement in signal provided by Dynamic Nuclear Polarization (DNP) was used to investigate the same metabolic pathways in the TRansgenic Adenocarcinoma of Mouse Prostate (TRAMP) model by injecting the mice with hyperpolarized ^{13}C-1 pyruvate. The spatial distribution of the hyperpolarized pyruvate and its metabolic products were measured in just 14 seconds using a rapid ^{13}C MRSI technique. Furthermore, the time course of the conversion of pyruvate to lactate and alanine was measured in the mice. The prostate cancer cell cultures demonstrated that the citric acid cycle consumed significantly more pyruvate than lactate synthesis or

fatty acid biosynthesis. In addition, the tissue cultures indicated that the citric acid cycle utilization of pyruvate was higher in prostate cancer than in normal secretory tissue, along with higher lactate synthesis in cancer. Moving towards the clinic, the *in-vivo* hyperpolarized studies demonstrated that the conversion of pyruvate to lactate was grade dependent with late stage tumors having the highest lactate levels. Since there was minimal overlap between the lactate levels from normal prostates and early and late stage tumors, hyperpolarized ^{13}C pyruvate has great potential as a new biomarker capable of non-invasively staging prostate cancer and great potential for future studies of prostate cancer patients.

Table of Contents:

CHAPTER 1 STATE OF THE ART AND NEW OPPORTUNITIES FOR PROSTATE CANCER IMAGING AND PROSTATE BIOCHEMISTRY 1

1.1 Motivation and Specific Aims of the Project 1

1.2 Clinical Importance 2

1.3 Current In-Vivo MR Techniques 3

1.4 Prostate Anatomy 6

1.5 Unique Biochemistry of Prostate 8

1.6 Creating Metabolic Tracers for Studying Prostate Biochemistry with ^{13}C Labeling 16

CHAPTER 2 STUDYING PROSTATE BIOCHEMISTRY USING ^{13}C LABELED METABOLIC SUBSTRATES 20

2.1 Measuring Incorporation of ^{13}C Labeled Metabolic Substrates in Model Systems using HR-MAS 20

2.2 Measuring Incorporation and Metbolism of ^{13}C Labeled Substrates in Live Transgenic Mice using Hyperpolarization 29

CHAPTER 3 DEVELOPMENT OF HR-MAS TECHNIQUES NECESSARY FOR MEASURING AND QUANTIFYING METABOLISM OF ^{13}C LABELED COMPOUNDS 37

3.1 Quantification References for One Dimensional ^{1}H HR-MAS Spectroscopy 37

3.2 Quantification References for ^{13}C HSQC Experiments 58

3.3 Decoupling Optimization 61

CHAPTER 4 INVESTIGATING METABOLIC CHANGES IN NEW HUMAN PROSTATE CANCER MODEL SYSTEMS WITH ^{13}C LABELING 70

4.1 Requirements for a Model System of Prostate Metabolism 70

4.2 Primary Cultured Epithelial Cells 73

4.3 Human Tissue Cultures 97

CHAPTER 5 USING HYPERPOLARIZED ^{13}C-1 PYRUVATE, LACTATE, AND ALANINE TO NON-INVASIVELY DETECT AND STAGE PROSTATE CANCER IN TRANSGENIC MICE 107

CHAPTER 6 REFERENCES 129

List of Figures:

Figure 1.1 *In-vivo* ^{1}H spectra taken from an MRSI exam of a human prostate showing an example of the spectral profile for healthy peripheral zone prostate tissue **(A)** and prostate cancer **(B)**. The ^{1}H HR-MAS spectra of prostate tissue samples taken from healthy peripheral zone prostate tissue **(C)** and prostate cancer **(D)** exhibit a similar metabolic profile with more detailed spectral information. The spectra were adapted from reference (35). Cho: Choline, PA: Polyamines, Cr: Creatine, GPC: Glycerophosphocholine, PC: Phosphocholine. **5**

Figure 1.2 Sagittal cross section of the human prostate depicting the zonal anatomy of the prostate. S: Superior, I: Inferior, A: Anterior, P: Posterior, SV: Seminal Vesicles, CZ: Central Zone, PZ: Peripheral Zone, AFB: Anterior Fibromuscular Band. **8**

Figure 1.3 Diagram of pertinent intracellular metabolic pathways that exist in secretory prostatic cells. The red lines represent the pathways that are active in healthy secretory prostatic cells and the black lines along with the gray background highlight the metabolic adaptations proposed to occur with prostate cancer. The orange metabolites are in the cytosol and the green metabolites are in the mitochondria. While the diagram illustrates the reactions that affect the various metabolites, it does not document the entire reaction. As a result, several of the reactions are not balanced. AAT: Aspartate Aminotransferase, ACC: Acetyl-CoA Carboxylase, ACL: ATP-Citrate Lyase, CS: Citrate Synthase, FAS: Fatty Acid Synthase, Glut: Glutamate, α-KG: α-Ketoglutarate, LDH: Lactate Dehydrogenase, PDH: Pyruvate Dehydrogenase. **13**

Figure 1.4 Diagram of the fate of ^{13}C labeled pyruvate in the pertinent intracellular metabolic pathways that exist in secretory prostatic cells. The pink, blue, and yellow boxes highlight the fates of ^{13}C-1, ^{13}C-2, and ^{13}C-3 pyruvate, respectively, as they pass through the various pathways. The hatched yellow and blue boxes on oxaloacetate indicate which positions will be labeled if it is derived from malate following the incorporation of a ^{13}C labeled pyruvate molecule. The labeling of oxaloacetate in this case is split between two carbon positions because succinate is a symmetric molecule. The red lines represent the pathways that are active in healthy secretory prostatic cells and the black lines along with the gray background highlight the metabolic adaptations proposed to occur with prostate cancer. While the diagram illustrates the reactions that affect the various metabolites, it does not document the entire reaction. As a result, several of the reactions are not balanced. Glut: Glutamate, α-KG: α-Ketoglutarate, Zn: Zinc. **19**

Figure 2.1 High resolution NMR spectra recorded from rat brain cortex at 11.7T after it was placed in an NMR tube *(TOP)* and under HR-MAS conditions *(BOTTOM)*. The spectrum acquired using HR-MAS exhibits a significant reduction in chemical shift anisotropy as demonstrated by the decrease in the linewidth of N-Acetyl-Aspartate (NAA) from 17.4 to 4.3 Hz. **24**

Figure 2.2 Photograph of an HR-MAS rotor. The rotors consisted of a T-shaped zirconium base, a plastic collar with machined groves on the underside, and an opaque plastic insert fitted with a rubber O-ring and a threaded head. The insert mated with the

plastic collar and provided a leak proof seal for the rotor. The groves in the collar served as a turbine and caused the rotor to spin when air was blown across it (40). **27**

Figure 2.3 Thermal polarization for ^{13}C nuclei, ^{1}H nuclei, and electrons (e^-) when they are exposed to a 3.35 T external magnetic field. The polarizations were computed using Eq. [2.7]. **32**

Figure 3.1 A) Pulse sequence diagram of the ERETIC sequence and **B)** system diagram of the Varian INOVA console highlighting the modifications required for generating an ERETIC signal at the ^{1}H frequency. The output of the ^{1}H synthesizer was shared between the waveform generators (WG) for channels 1 and 3. The ERETIC signal was taken directly from the output of the Programmable Attenuator (PA) module, combined with the output from channel 2 using a directional coupler, and transmitted through the X channel of the nanoprobe. The transmission of the ERETIC waveform and the data acquisition were synchronized in the pulse sequence. (d1: relaxation delay; satdly: presaturation delay; pw: pulse width; at: acquisition time; BP: bandpass) **40**

Figure 3.2 Linearity of ERETIC signal area with ERETIC power plot. The blue diamonds represent the average of three HR-MAS measurements taken on the same solution sample after they were normalized to remove arbitrary scaling factors introduced by the spectrometer's electronics. The black line is a plot of the fit obtained on the data from Matlab. The equation for the fit is written in the inset along with its R^2 value. Since the leading coefficient of the fitted model is 1.187, the model indicates that the ERETIC signal area does NOT exhibit the one-to-one correlation with the ERETIC power that would be expected from an ideal spectrometer. **47**

Figure 3.3 Relative standard deviation (RSD) of the ERETIC peak area and TSP peak area (corrected for mass) from identically prepared solution samples acquired **A** and **B)** on five consecutive days during three separate weeks and **C** and **D)** over five months. The solid line represents the mean peak area over the relevant time period, the dotted lines represent 5% deviations from the mean, and the small dashes in plots A and B represent the weekly means. Samples were prepared by adding 3 µL of D_2O+TSP (weighed to +/- 0.01 mg), and filling the remainder of the rotor volume with plain D_2O. The average weekly RSD of the ERETIC peak area was 4.25%, 3.29%, and 2.09% during each week respectively, while corrected TSP peak area RSD's were 4.30%, 6.76%, and 3.57% during the same periods. The average monthly RSD was 4.10% and 2.47% for ERETIC and TSP, respectively. **48**

Figure 3.4 Plot of the TSP peak area (A_{TSP}) / ERETIC peak area (A_E) versus micromoles of TSP protons determined by weight in the **A)** 20 µL and **B)** 35 µL rotors. Linear regression was performed on the data to calculate the rotor-specific conversion factors (M_E), as contained in Eq. [3.2]. M_E represents the equivalent amount of protons for the ERETIC peak and can be used for quantification of metabolites. The M_E for the 20µL rotor was 30% greater than the M_E for the 35µL rotor. **50**

Figure 3.5 Representative HR-MAS spectrum of prostate surgical tissue with the ERETIC signal generated at a frequency of -0.5 ppm and with a transmitter power of 0 dB. The phase of the ERETIC signal was matched to the metabolites before the acquisition and produced a peak that had a phase and amplitude comparable to those of the tissue

metabolites. The frequency of the ERETIC signal was well separated from the other peaks in the spectrum and allowed for accurate quantification of its peak. _____ **52**

Figure 3.6 Comparison of the **A)** TSP and **B)** ERETIC peaks from a prostate surgical sample and solution sample with a comparable amount of TSP. The surgical sample was amplified by 22.1% to correct for loading differences between the two spectra, determined by the differences in the ERETIC peak area and the 90° pulse width. The TSP peak from the solution spectrum was apodized by 2.9Hz to match the linewidths of the TSP peaks in the two spectra. Since the TSP peak area in the tissue spectrum was 28.7% of the peak area in the solution spectrum, a significant amount of the TSP was not detected in the HR-MAS experiment. _____ **53**

Figure 3.7 A diagram of the PWXCAL pulse sequence used to perform an indirect calibration of the ^{13}C 90° pulse width. The numbers in white are in seconds, the numbers in yellow are in milliseconds, and the numbers in light blue are in microseconds. The ^{1}H channel is displayed at the top of the diagram, labeled as Tx, and the ^{13}C channel is displayed at the bottom of the diagram, labeled as Dec. _____ **65**

Figure 3.8 **(A)** Carbon decoupling profile plot and **(B)** decoupling bandwidth vs. decoupling power plot for several permutations of GARP and adiabatic decoupling. All the data are taking from $^{1}H[^{13}C]$ spectra collected from a solution sample of ^{13}C-2 glycine. The top panel depicts how well the glycine was decoupled as function of the decoupler offset frequency. The small depressions in the flattops of the profiles indicate that the decoupling performance was slightly degraded at certain frequencies. The bottom panel illustrates the tradeoff between the decoupling bandwidth and the decoupling power. The best combination, large bandwidth and low power, is shaded white on the plot and the worst combination is shaded red. The adiabatic scheme with 1,400μsec pulses exhibited the largest decoupling bandwidth with the least amount of decoupling power. _____ **68**

Figure 3.9 Decoupling sidebands for various decoupling schemes. The $^{1}H[^{13}C]$ spectra were obtained from a solution of ^{13}C-2 glycine. _____ **69**

Figure 4.1 A photograph of a sample tube just after fabrication. The sample tube was assembled from a modified Pasteur pipette and a modified blood caraway tube. ____ **78**

Figure 4.2 **(A)** Proton HR-MAS spectra of DME medium *(TOP)* and PFMR-4A medium *(BOTTOM)*. The PFMR-4A spectrum contains several large peaks (★) that ultimately contaminated the spectra of the cells cultured in this medium prior to harvesting the cells as shown in the bottom of **(B)**. By culturing the cells in DME for the last 24 hours *(TOP of B)*, the spectral contamination caused by the PFMR-4A medium was significantly reduced as indicated by the black arrows. In addition, the glutamine levels were significantly reduced because the DME medium contained less glutamine. Note the large glycine peak in the DME cell spectrum was produced by the reference compound added for the HR-MAS experiment. Also, the chemical shifts of the contaminants were slightly different in the cells than in the medium solution, which was likely caused by binding differences. _____ **84**

Figure 4.3 $^{1}H[^{13}C]$ HR-MAS spectra of primary cultured prostate cancer cells after the cells were washed with cold PBS twice *(TOP)* and three times *(BOTTOM)*. The contaminant

at 3.18 ppm was residual contamination from PFMR-4A medium and was slightly higher when the cells were only washed twice. However, the PC peak was also larger with two washes, suggesting that the additional wash removed metabolites as well. Ultimately, two washes were used in the experiments in order to avoid washing away metabolites at the expense of some minor additional contamination. **85**

Figure 4.4 Representative $^{1}H[^{13}C]$ HR-MAS spectrum from primary cultured prostate cancer cells. The spectrum was acquired from 25.6 mg of cells in 16.1 min. Prominent peaks include the glycine reference, lactate, phosphocholine (PC), aspartate, glutathione, glutamine, glutamate (Glu), and Glx (composite of glutamate, glutamine, and glutathione). Cho: choline; Cr: creatine; NA: N-acetyl peak. **86**

Figure 4.5 Representative ^{13}C HSQC spectrum from primary cultured prostate cancer cells using HR-MAS. Maximum intensity projections along ^{1}H and ^{13}C dimensions are shown at the top and left, respectively. The spectrum was acquired from 26.5 mg of cells in 2.78 hrs. It contains strong ^{13}C labeled signals from Glutamate-C4, Aspartate-C3, Alanine-C3, Lactate-C3, Aspartat-C2, and Glutamate-C2. Since the relative peak intensities for the prominent peaks in this spectrum are greater than their relative intensities in $^{1}H[^{13}C]$ spectrum (Figure 4.4), it is clear that the ^{13}C label is incorporated into the pathways of interest. **87**

Figure 4.6 (A) Fractional enrichment of the several metabolites following the delivery of ^{13}C-3 pyruvate to primary cultured prostate cancer cells derived from five different prostate cancer patients. The prostate cancers from patients 1-3 had a Gleason score of 3+3 and the patients 4 and 5 had a Gleason score of 4+3. **(B)** The average and standard deviation of the concentration of the ^{13}C pool for each of the metabolites is also presented. While all the metabolites were enriched above natural abundance, the ^{13}C-3 pyruvate was converted to glutamate more than any of the other metabolites during a 2 hour exposure to the pyruvate. Pt: Patient; Ala: Alanine; Glut: Glutamate; Asp: Aspartate; Lac: Lactate. **89**

Figure 4.7 Photograph of prostate tissue core *(Green Open Arrow)* after it has been embedded in agarose gel *(White Solid Arrow)* to attach it to a stainless steel microtome plunger *(White Star)*. **99**

Figure 4.8 A photograph of a sample tube designed for storing tissue cultures. The sample tube was fabricated from a plastic transfer pipette. **100**

Figure 4.9 $^{1}H[^{13}C]$ spectra acquired from ~25 mg of healthy *(TOP)* and cancerous *(BOTTOM)* prostate tissue slices after being cultured for 2 hours. Similar to *in-vivo* ^{1}H spectra, the healthy sample had high levels of citrate and polyamines and moderate levels of choline. Compare the cancer sample to the healthy sample, it had higher levels of PC and lactate as well as almost no citrate nor polyamines. **102**

Figure 4.10 Proton spectra acquired from ~5mg of healthy *(TOP)* and cancerous *(BOTTOM)* prostate biopsies. The cancer shows a significant reduction in Citrate, Polyamines, and an increase in GPC / PC and lactate. **103**

Figure 4.11 Prostate tissue slices viewed under 10X magnification after they were cut into 10μm thick sections and stained with Heomatoxylin & Eosin. Based on the histology, the cancer sample was graded as a Gleason 3+4 cancer. **103**

Figure 4.12 Metabolite averages and standard deviations for 10 healthy and 8 cancerous prostate biopsies *(LEFT)*. Averages and standard deviations for 8 healthy and 10 cancerous prostate tissue cultures *(RIGHT).* Total choline (tCho) was computed by summing choline, PC, and GPC. Asterisks indicate statistical differences. **104**

Figure 4.13 ^{13}C HSQC spectra acquired from healthy *(LEFT)* and cancerous *(RIGHT)* prostate tissue slices after being cultured for 2 hours with ^{13}C-3 pyruvate. The cancer sample was graded as a Gleason 3+4 cancer. **105**

Figure 5.1 Diagram of the ^{13}C-1 pyruvate and the metabolic pathways relevant to this study **(A)**. The hyperpolarized ^{13}C spectra **(B)** and peak height plots **(C)** show the time course for the hyperpolarized ^{13}C-1 pyruvate and its metabolic products following the injection of 350 μL of hyperpolarized pyruvate. The pyruvate was injected at a constant rate from 0 to 12 seconds. The MR spectra were acquired every 3 seconds from a 28 week old TRAMP mouse with a late stage tumor using a 5° flip angle and a 10 mm thick slice. The peak height plot was corrected for the amount of magnetization used to record the previous n spectra by dividing each peak height by $\cos^n(5°)$. The hyperpolarized pyruvate quickly reached a maximum at 24 seconds before being converted to lactate and alanine. Based on this time course, the subsequent MRSI data were recorded between 35 and 49 seconds, a time when the hyperpolarized lactate signal was roughly constant. Glut: Glutamate; α-KG: α-ketoglutarate; LDH: Lactate Dehydrogenase; ALT: Alanine Transaminase. **113**

Figure 5.2 Axial T_2 weighted ^1H image depicting the primary tumor and lymph node metastasis from a Late Stage TRMP mouse **(A)** and the overlay of an interpolated hyperpolarized ^{13}C lactate image following the injection of 350 μL of hyperpolarized ^{13}C-1 pyruvate **(B)**. After spatially zero-filling and voxel shifting the ^{13}C spectra to maximize the amount of tumor in the voxels, a subset of the spectral grid was selected **(C)** and displayed **(D)**. The 3D MRSI was acquired with a nominal voxel resolution of 135 mm^3 and zerofilled to a resolution of 17 mm^3. The spectra show substantially elevated lactate in the late stage tumor as compared to the early stage tumor shown in Figure 5.3. In addition, the metabolite signal is significantly lower in the necrotic regions of the primary tumor. Lac: Lactate, Ala: Alanine, Pyr: Pyruvate. **119**

Figure 5.3 Axial T_2 weighted ^1H image depicting the primary tumor from an Early Stage TRMP mouse **(A)** and the overlay of an interpolated hyperpolarized ^{13}C lactate image following the injection of 350 μL of hyperpolarized ^{13}C-1 pyruvate **(B)**. The numerical range of the color map in the lactate image was reduced to half the range used in Figure 5.2 to allow visualization of the lower hyperpolarized lactate levels. After spatially zero-filling and voxel shifting the ^{13}C spectra to maximize the amount of tumor in the voxels, one voxel from the primary tumor was selected **(C)** and displayed **(D)**. The 3D MRSI was acquired with a nominal voxel resolution of 135 mm^3 (dashed white box) and zerofilled to a resolution of 17 mm^3 (solid white box). The spectrum shows prominent signals from lactate and pyruvate and smaller signals from alanine and pyruvate-hydrate. **120**

Figure 5.4 Representative H&E stained sections and hyperpolarized ^{13}C spectra for one case from each of the histologically defined groups. The histology slides were processed using 5 μm thick sections and photographed with 40X magnification. The hyperpolarized ^{13}C spectra represent voxels taken from MRSI datasets and normalized to correct for differences in polarization and receiver sensitivity. The normalized spectra illustrate the strong correlation that exists between the amount of hyperpolarized ^{13}C lactate and the progression of the disease from the normal prostates to the early stage tumors and the late stage tumors. **122**

Figure 5.5 Numerical comparisons of hyperpolarized ^{13}C metabolites with the pathologically defined groups. A bar plot summarizes the peak area to noise ratios (average $\pm$ standard deviation) of the ^{13}C labeled lactate, pyruvate, and alanine for the four histologically defined groups **(A)**. The lactate peak area SNR values were statistically different for all four groups, except that early stage tumors were not different from lymph node metastases ($p < 0.05$). While the alanine SNR values were not quite statistically different, they exhibited similar trends to the lactate values as shown by the lactate versus alanine plot **(B)**. The box plot of the individual values for the lactate SNR **(C)** shows that there was almost no overlap between the normal prostates, early stage tumors, and late stage tumors. The plot of lactate versus total hyperpolarized carbon **(D)** suggests that much of the within group scatter of the lactate SNR may be related to variability in the amount of hyperpolarized carbon delivered to the tissue. **124**

List of Tables:

Table 2.1 Key biological and NMR properties for water and lactate in humans. The concentrations ([C]) refer to the concentrations of the specified nucleus within the molecule of interest. In the case of lactate, the concentrations are for C-3 lactate. Since these values are for natural conditions, the fractional enrichment (FE) values are equivalent to the nuclei's natural abundance. The polarization values (P) were determined using Eq. [2.7] and assuming the nuclei were in a 3.0 T magnetic field at body temperature (310°K). **32**

Table 3.1: Precision and accuracy of the number of TSP protons (μmol) measured using the ERETIC method from solution samples of equal volume. The left column shows the number of TSP protons calculated using the mass of TSP in the rotor (weighed to +/- 0.01 mg). The second column shows the mean and standard deviations of the same protons calculated using M_E and the ERETIC and TSP peak areas from five consecutive acquisitions. The third column shows the precision of the measurement expressed as the RSD. The fourth column shows the accuracy obtained using Eq. [3.4]. **51**

Table 3.2: Relative standard deviations (RSD) of the TSP peak area (corrected for mass) and ERETIC peak area in solution and prostate biopsy and surgical tissues. **53**

Table 3.3 The measured decoupling bandwidth for various permutation of the GARP and adiabatic decoupling schemes. **69**

Table 5.1: Histological classification and average hyperpolarized 13C metabolite SNR for each mouse. *The histological classifications were defined as Well Differentiated (WD), Moderately Well Differentiated (MWD), and Poorly Differentiated (PD). &The histological index ranges between 0 and 3, where 0 indicates that 100% of the tissue was normal and 3 indicates that 100% of the tissue was PD. The values for the small tumors were corrected for partial volume effects. §The normal mice were assumed to have a 100% normal prostate based on histological analysis of separate mice. †Due to the large size of the late stage tumors, the histological classification for these tumors was estimated from 3-5 sections taken from the tumor. ††The percentage of necrosis for the late stage tumors was estimated from the anatomical MR images because it was not practical to estimate it from the histology. **116**

Chapter 1
State of the Art and New Opportunities for Prostate Cancer Imaging and Prostate Biochemistry

1.1 Motivation and Specific Aims of the Project

The accurate detection and characterization of prostate cancer remains a major problem for the clinical management of individual prostate cancer patients and for monitoring their response to therapy. During the past several years, technological advances in Magnetic Resonance Spectroscopic Imaging (MRSI) have made it possible to correlate in-vivo prostatic citrate concentrations with the presence and grade of prostate cancer. Based on the analysis of human prostate tissue samples and results obtained from animal models of prostate cancer, it has been hypothesized that the observed decrease in citrate with prostate cancer is associated with increased citrate oxidation in the citric acid cycle, increased fatty acid synthesis, and/or increased glycolytic lactate production. By using ^{13}C labeled pyruvate to study prostate cancer, it is may be possible to simultaneously and noninvasively assess changes in metabolic intermediates from all the biochemical pathways (glycolysis, citric acid cycle, and fatty acid synthesis) of interest and thereby explain the observed changes in prostatic citrate concentrations. In this project, these hypotheses will be investigated with ^{13}C labeled pyruvate in two types of prostate cancer model systems to accomplish the following specific aims.

A. Incorporate synthetically enriched ^{13}C-3 pyruvate in a prostate cancer culture model system and measuring the labeling of pyruvate and its products using HR-MAS.

   A1. Devise a spectral quantification strategy for the HR-MAS experiments.

   A2. Develop an HR-MAS protocol for efficiently detecting the ^{13}C labeled metabolites.

   A3. Establish a protocol for incorporating ^{13}C-3 pyruvate into the pathways of interest within primary cultured prostate cancer cells and prostate tissue cultures and detecting the uptake of the label with HR-MAS.

B. Measure the amount of ^{13}C labeling in the products of ^{13}C-1 pyruvate within prostate cancer tissue following the injection of hyperpolarized ^{13}C-1 pyruvate into a transgenic mouse prostate cancer model.

   B1. Develop an *in-vivo* MRSI protocol for injecting hyperpolarized ^{13}C-1 pyruvate into a mouse and detecting its metabolic products before the polarization is lost.

   B2. Quantify the changes in hyperpolarized ^{13}C-1 pyruvate and its metabolic products that occur as prostate cancer develops and progresses in a transgenic mouse prostate cancer model.

The results from this project will help explain the changes in citrate concentrations that occur with prostate cancer and may provide new biomarkers for detecting the cancer and monitoring therapy. The new biomarkers will likely be clinically useful in the near future because of recent advances in high field in-vivo scanners and ^{13}C hyperpolarization techniques. In this chapter the clinical need for new imaging biomarkers of prostate cancer and the unique metabolism that leads to these biomarkers are described.

1.2 Clinical Importance

The American Cancer Society estimates that 222,389 males will be newly diagnosed with prostate cancer in the United States alone in 2007 (1). This makes prostate cancer the most commonly diagnosed non-cutaneous cancer among American men in the United States, with an incidence rate higher than breast cancer in women (1). At this rate, 1 out 6 men in the U.S. will develop prostate cancer during their lifetime (1). While the use of PSA (Prostate Specific Antigen) screening and TRUS (transrectal ultrasound) guided biopsies has lead to an increase in early detection of prostate cancer (2), the decision on how to manage prostate cancer once diagnosed poses a great dilemma for patients and their clinicians because it possesses a tremendous range in malignancy and risk. It is one of the only cancers that can grow so slowly that it will never threaten the lives of some patients. However, if the cancer metastasizes, there is no cure and it becomes lethal, causing an estimated 26,059 deaths in the United States

in 2007 (1). Consequently, it is treated with a broad spectrum of approaches ranging from routine monitoring, referred to as active surveillance, and hormone deprivation therapy to aggressive treatments, such as surgery, radiation, and cryosurgical therapies (3, 4). The less aggressive treatments will not eradicate the metastatic cancers and, the more aggressive treatments present a significant risk for life altering side effects, such as incontinence or impotence. Clearly, early detection of the cancer's metastatic potential or therapeutic response and selecting the appropriate treatment for the type of cancer is necessary. Unfortunately, the metastatic potential of the prostate cancer cannot be reliably predicted in individual patients with current prognostic markers (5-9). Currently, the risk assessment of individual patients at diagnosis primarily relies on a number of clinical parameters including serum PSA, clinical stage (determined by means of digital rectal examination and TRUS), and systematic TRUS-guided biopsy results (number and percentage of positive cores and grade of the core) (2). However, these are often inaccurate or inadequate, particularly when used alone for individual patients. Therefore, prostate cancer management, in contrast to the management of most other cancers, requires accurate imaging information to select the most appropriate treatment for individual patients.

1.3 Current In-Vivo MR Techniques

The use of magnetic resonance imaging (MRI) and magnetic resonance spectroscopic imaging (MRSI) has provided a new approach for non-invasively diagnosing and staging prostate cancer. Conventional MR imaging of the prostate relies on abnormal signal intensities that result from morphologic changes within the prostate to define the presence and extent of cancer (10, 11). Unfortunately, the morphologic changes observed by MRI often do not accurately reflect the presence and spatial extent of active tumor (10, 11). When ^{1}H MRSI is performed in conjunction with high-resolution anatomic imaging, it can non-invasively detect changes in cytosolic and extracellular

metabolites caused by prostate cancer, such as decreased citrate, increased choline, and decreased spermine (see Figure 1.1) (12). Studies in pre-prostatectomy patients have indicated that when ^{1}H MRSI is combined with MRI (13) there are significant improvements in the assessment of the cancer's location and extent within the prostate (14-19), extracapsular spread (20, 21), and the cancer's aggressiveness (22, 23). MRI/MRSI has also been shown to provide a direct measure of the presence and spatial extent of prostate cancer after therapy (24-31), a measure of the time course of therapeutic response (25, 28), and information concerning the mechanism of therapeutic response (25, 28). While the combined imaging technique has shown great promise for improving *in-vivo* prostate cancer detection and characterization prior to and following therapy, it still has several limitations. Namely, 1) it is unable to measure a couple of key Krebs cycle intermediates as well as lactate and alanine because of their low concentrations, and overlapping lipid in the case of lactate and alanine, 2) it is unable to detect and characterize small amounts of cancer (< 0.5cc) (32), and 3) it is unable to discriminate a number of benign conditions (stromal BPH, prostatitis) from prostate cancer (33, 34).

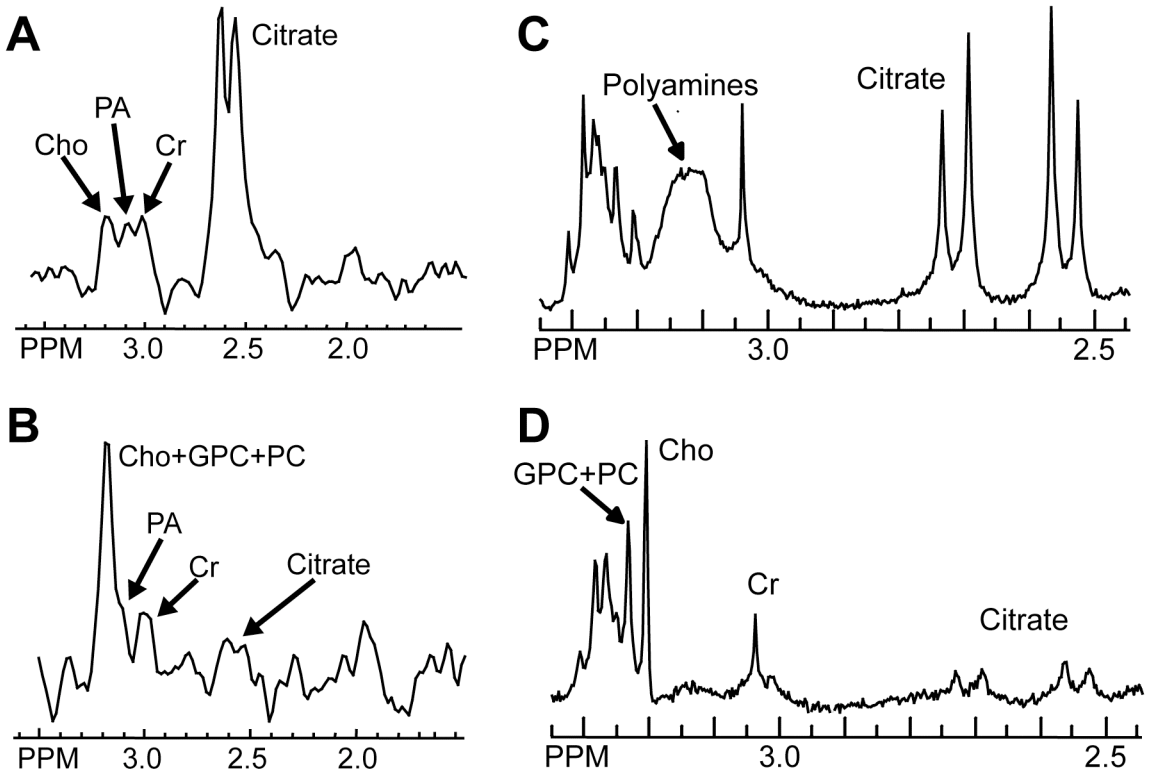

Figure 1.1 *In-vivo* ^{1}H spectra taken from an MRSI exam of a human prostate showing an example of the spectral profile for healthy peripheral zone prostate tissue **(A)** and prostate cancer **(B)**. The ^{1}H HR-MAS spectra of prostate tissue samples taken from healthy peripheral zone prostate tissue **(C)** and prostate cancer **(D)** exhibit a similar metabolic profile with more detailed spectral information. The spectra were adapted from reference (35). Cho: Choline, PA: Polyamines, Cr: Creatine, GPC: Glycerophosphocholine, PC: Phosphocholine.

More recently, high resolution magic angle spinning (HR-MAS) spectroscopic techniques have been developed that allow solution-like nuclear magnetic resonance (NMR) spectra to be obtained from intact tissue specimens while preserving the tissue for further pathologic and genetic study (35-42). Historically, high-resolution NMR systems have produced spectra with larger spectral peak separations because of their stronger magnetic field. However, metabolite peaks from prostate tissue samples are still relatively broad (43) due to chemical shift anisotropy (CSA) and dipolar coupling. The CSA can almost be eliminated by using perchloric acid tissue extracts as previously shown (44-46). Unfortunately, labile metabolites can be lost during extraction and it

makes it impossible to histologically analyze the tissue. High resolution – magic angle spinning (HR-MAS) is another technique that reduces CSA by spinning the sample at an angle (54.7°) relative to the main field. This approach is completely nondestructive to the tissue if performed at low enough spin rates. Swanson *et al.* have shown that ^{1}H HR-MAS can be used to detect the known metabolic changes in prostate cancer (decreased citrate, decreased polyamines, increased choline containing compounds, etc. as shown in Figure 1.1). Furthermore, they were able to correlate the metabolic changes with the histopathological analysis performed on the prostate tissue samples following the HR-MAS experiments (35). More recently, the group has shown that surgical (40) and biopsy (47) specimens taken from prostate cancer exhibit higher levels of lactate and alanine relative to benign specimens using HR-MAS as well. Therefore, HR-MAS produces spectra with great spectral resolution (narrow peaks with large separations) from small tissue samples (5-40mg) and allows correlation with quantitative histopathology data from the same tissue sample. In addition, the improved sensitivity afforded by the higher magnetic field strength and improved filling factor of the RF coil make it possible to detect changes in metabolites, such as lactate and alanine, which historically haven't been investigated using in-vivo ^{1}H MRS for technical reasons. These findings indicate that HR-MAS provides an excellent platform for investigating new biomarkers that may eventually be translatable to clinic MR exams. On the down side, the technique cannot be directly applied to in-vivo studies. Thus, the clinical translation of HR-MAS discoveries may necessitate the development of new MR techniques that probe the same biomarker using a slightly different approach.

1.4 Prostate Anatomy

The prostate is a pale firm exocrine gland shaped like an inverted pyramid that surrounds the urethra between the bladder neck and genitourinary membrane, lying just anteriorly of the rectum. The ejaculatory ducts pass obliquely through the gland to enter

the prostatic urethra at the verumontanum. The normal adult gland is about the size of a walnut, measuring approximately 4 (left-right) x 3 (anterior-posterior) x 3 (superior-inferior) cm, and weighing 15 to 20 grams. The contemporary approach to prostate anatomy describes the internal structure in terms of zones. The simplest conceptual approach to the zonal anatomy of the prostate is the two-compartment model, where the prostate is likened to a cone containing a scoop of ice cream (48). The cone is the peripheral zone, and makes up 70% of the prostate gland by volume in young men. The ducts of the peripheral zone glands drain to the distal prostatic urethra. The scoop of ice cream is the central zone, and makes up 25% of the prostate gland volume in young men (Figure 1.2). The ejaculatory ducts traverse the central zone, and the ducts of the central zone drain to the region of the verumontanum clustered around the entry of the ejaculatory ducts. The final 5% of the prostate consists of the transition zone, which is composed of two small bulges of tissue that surround the anterior and lateral parts of the proximal urethra in a horseshoe-like fashion. This two-compartment model is deficient anteriorly, where the peripheral zone is interrupted by the anterior fibromuscular stroma, a band of smooth muscle mixed with fibrous tissue that forms a thick shield over the anterior aspect of the gland as shown in Figure 1.2. As a result, the peripheral zone lies predominantly lateral and posterior to the central zone.

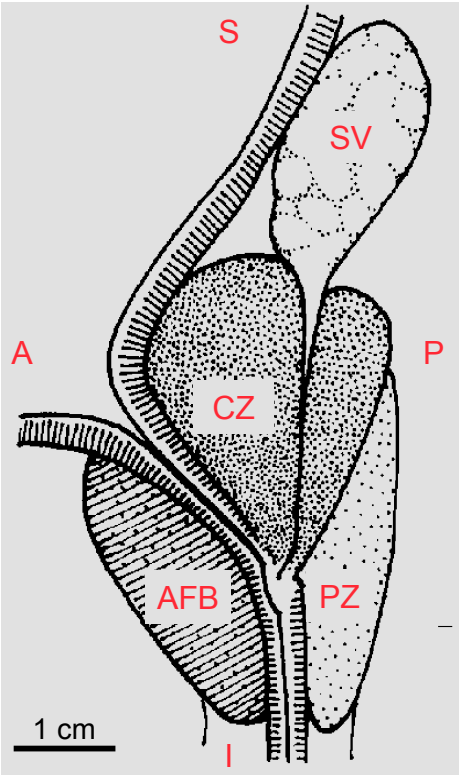

Figure 1.2 Sagittal cross section of the human prostate depicting the zonal anatomy of the prostate. S: Superior, I: Inferior, A: Anterior, P: Posterior, SV: Seminal Vesicles, CZ: Central Zone, PZ: Peripheral Zone, AFB: Anterior Fibromuscular Band.

1.5 Unique Biochemistry of Prostate

Normal secretory epithelial cells in the peripheral zone of the human prostate uniquely synthesize very high amounts of citrate causing them to have higher citrate concentrations than any other human tissue type (49). In addition, prostate tissue has zinc levels that are 2-10 times higher than other organs with the lateral lobes of the prostate's peripheral zone having the highest levels at 211 μg of zinc per gram of tissue wet weight (50). The zinc levels have been shown to be at least 2 times higher in the epithelial cells of the prostate as compared to the stromal cells (51) and it increases with exposure to testosterone (50). The high zinc levels are a direct result of an increase in the number of high velocity zinc transporters present in the secretory epithelial cells. Costello and Franklin have shown that hZIP1 is a zinc transporter that is strongly expressed in normal peripheral zone tissue and the velocity of zinc uptake is significantly

enhanced in cells over-expressing hZIP1 (52, 53). Interestingly, the citrate levels are tightly coupled to the zinc levels because zinc slows the conversion of citrate to isocitrate in the citric acid cycle by inhibiting mitochondrial (m-) aconitase (54, 55), the enzyme that converts citrate to isocitrate. As shown in Figure 1.3, the inhibition of m-aconitase by zinc produces high citrate concentrations in the cytosol and even higher concentrations in the prostatic fluid secreted by the epithelial cells into the lumen of the prostate gland. As a result, high levels of citrate can be observed in ex-vivo and in-vivo ^{1}H (35) and ex-vivo ^{13}C MR spectra (56) of healthy glandular prostate tissues as shown in Figure 1.1. While its exact role is not definitely known, citrate is a major component in prostatic secretions and it is believed to be involved in sperm activation and motility. More specifically, it has been suggested that the citrate may serve as a buffer to maintain the pH of semen; as a chelator for zinc and other cations which are also highly concentrated and involved in liquefaction of semen; as an energy source for the viability of sperm and/or the capacitation process of fertilization (49).

The ability to produce high amounts of citrate distinguishes normal secretory epithelial cells in the peripheral zone of the prostate, which will be referred to as secretory prostatic cells from this point forward, from all other human epithelial cells. In all healthy epithelial cells, glycolysis converts glucose into pyruvate, which is subsequently oxidized into acetyl-CoA (AcCoA) by pyruvate dehydrogenase. Within all healthy epithelial cells that are NOT secretory prostatic cells, the AcCoA enters the citric acid cycle by condensing with oxaloacetate to form citrate that is subsequently converted to isocitrate by m-aconitase. In these cells, the oxaloacetate is derived from malate by malate dehydrogenase, the last step in the citric acid cycle. Whereas, in secretory prostatic cells, the high zinc levels inhibit m-aconitase from converting citrate to isocitrate and oxaloacetate is derived from aspartate by mitochondrial aspartate

aminotransferase (AAT) as shown in Figure 1.3. The secretory prostatic cells require an alternate source of oxaloacetate because the citrate production deprives these cells of the citric acid cycle intermediates downstream from citrate. The inhibition of m-aconitase results in a cellular steady-state citrate/isocitrate ratio between 20:1 and 40:1 in healthy prostate tissue (57). In contrast, most other mammalian cells have a citrate/isocitrate ratio on the order of 10:1. Thus, citrate is accumulated in the cytosol of the cell (~ 1.2mM) and secreted into extracellular ducts where it reaches 150 mM concentrations (54, 55) (Figure 1.3). When the citrate is secreted into the ducts instead of being oxidized, the prostate epithelial cells sacrifice up to 63% of their potential energy production.

Once the cells become cancerous, the affected secretory prostatic cells produce significantly less citrate. Early biochemical studies have indicated that citrate levels in prostatic adenocarcinomas are grade dependent, with citrate levels being low in well-differentiated, low-grade prostate cancer and effectively absent in poorly-differentiated high-grade prostate cancer (46, 58). In more recent *in-vivo* proton MRSI studies, decreases in citrate also correlated with increasing cancer aggressiveness (Gleason grade) (22). The hypotheses that explain these changes involve perturbations to the citric acid cycle, fatty acid synthesis, and glycolysis and serve as the basis for the metabolic labeling studies being proposed in this work.

Changes in the Citric Acid Cycle: When secretory prostatic cells become cancerous, zinc levels are dramatically reduced, and the malignant epithelial cells demonstrate a diminished capacity for net citrate production and secretion (50, 59). The zinc levels in prostate cancer tissue are reduced to the levels found in other soft tissues as a result of a down-regulation in the hZIP1 transporters present in the secretory prostatic cells (49, 53). Lower zinc levels lead to a reduction in m-aconitase inhibition

causing an increase in the conversion of citrate to isocitrate and subsequent oxidation in the citric acid cycle. As a result, the citrate-to-isocitrate ratio in prostate cancer may be reduced to ~10:1 ratio observed in other normal mammalian cells. The Bioenergetic Theory of prostate cancer suggests that the transformation of secretory prostate cells to citrate oxidizing cells, which dramatically increases energy production capability of the cell, is essential to the process of malignancy and metastasis (60). For some cells, the normal cellular energy metabolism may be sufficient to meet the energy requirements associated with the neoplastic transformation to a malignant and/or metastatic state, but there is evidence that is not the case for prostate cancer (60). Healthy prostate tissue has been described as having a low rate of respiration, high anaerobic glycolysis and considerable aerobic glycolysis (glycolytic lactate production). It has been proposed that this low level of energy production is insufficient for cells to perform the activities associated with the process of malignancy (60). An increase in citrate oxidation would provide the cancer cells with 171% more ATP per glucose molecule than what is available to citrate producing prostatic cells, which may provide the energy they need for their malignant activities and proliferation.

Changes in Fatty Acid Synthesis: An increase in fatty acid synthesis may also contribute to the decrease in citrate levels observed in prostate cancer. An ex-vivo ^{13}C NMR study of prostate tissue samples taken from surgical specimens demonstrated that triacylglycerol, a molecule composed of three fatty acid chains, levels were higher in prostate cancer samples relative to benign samples (56). In addition, the androgen-regulated enzyme fatty acid synthase (FAS), required for *de novo* lipogenesis, is overexpressed in several cancers including prostate carcinoma and has been associated with aggressive disease (61). Both of these findings can be linked back to citrate through fatty acid synthesis, which begins with lipogenesis, a process that utilizes

cytosolic AcCoA to assembly fatty acid chains. Since the inner mitochondrial membrane is impermeable to AcCoA and AcCoA is typically produced inside the mitochondria, the bulk of the AcCoA used for *de novo* fatty acid synthesis is derived from citrate that has been transported out of the mitochondria as shown in Figure 1.3. After the citrate is exported to the cytosol, it is cleaved into AcCoA and Oxaloacetate (OAA) by ATP-citrate lyase. The cytosolic AcCoA is carboxylated by acetyl-CoA carboxylase (ACC) to form malonyl-CoA and combined with a second AcCoA molecule by FAS, which completes the first two steps of lipogenesis and fatty acid synthesis. The OAA is converted to malate and imported back into the mitochondria, where it reenters the citric acid cycle and replaces 4 of the 6 carbons lost when citrate was exported. Since this process consumes cytosolic citrate, it reduces the citrate levels from those observed in healthy secretory prostatic tissue. Also, it reduces the epithelial cells need to import aspartate because fatty acid synthesis returns 4 of citrate's 6 carbons to the citric acid cycle, whereas net citrate production utilizes all 6 carbons. The increase in *de novo* fatty acid biosynthesis may support the desire of these parasitic cancer cells to grow and proliferate (62). Prior studies have shown that alterations in distinct phospholipids and fatty acid levels are associated with malignant transformation and metastasis of prostate cancer (63-65). In recent proton HR-MAS studies of human prostate tissue samples taken from surgical specimens, there is strong evidence documenting elevation of choline compounds, key phospholipid membrane components, in prostate cancer (40). These studies provide further evidence that prostate cancer is tightly coupled with an increase in *de novo* fatty acid synthesis.

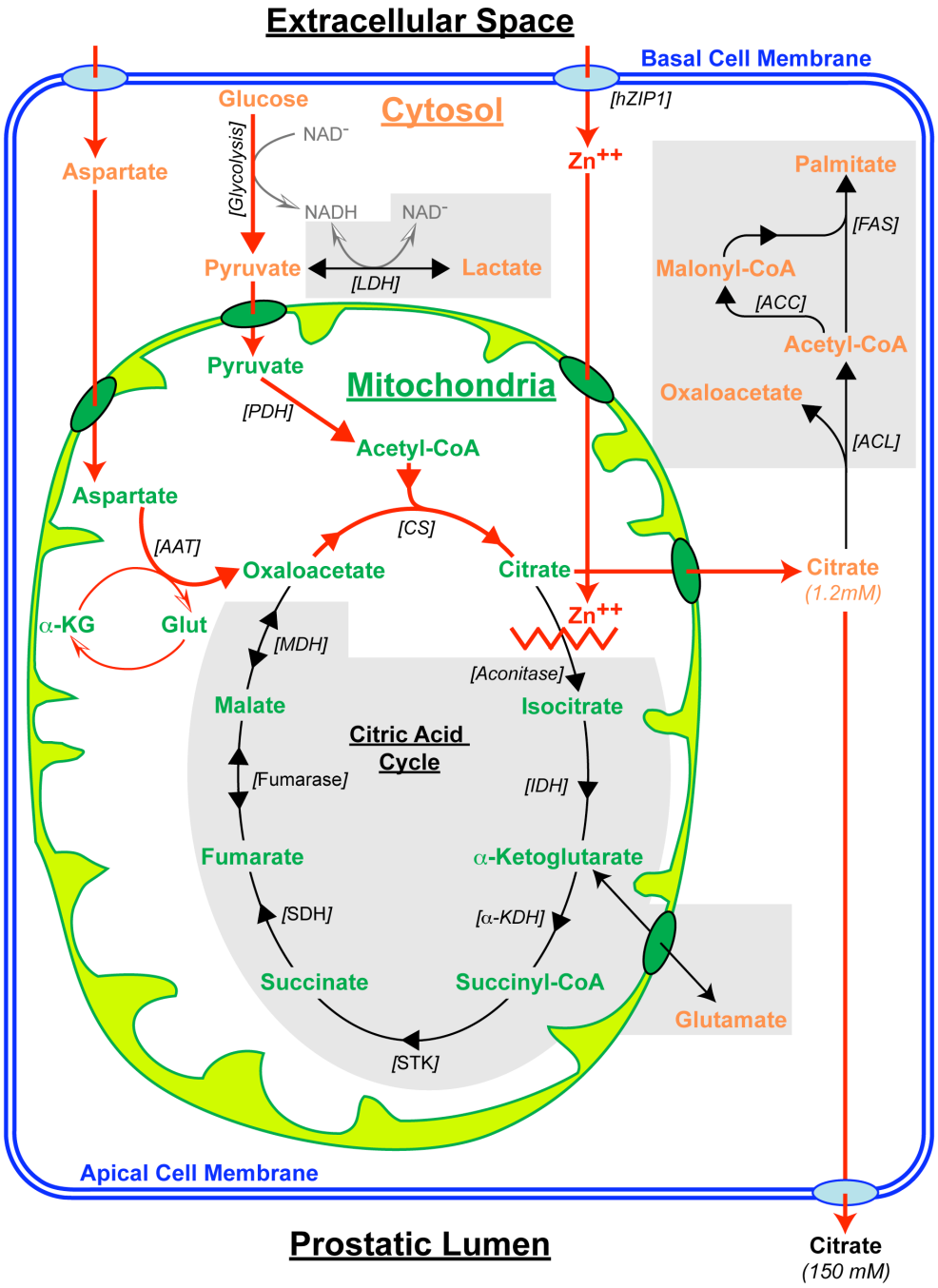

Figure 1.3 Diagram of pertinent intracellular metabolic pathways that exist in secretory prostatic cells. The red lines represent the pathways that are active in healthy secretory prostatic cells and the black lines along with the gray background highlight the metabolic adaptations proposed to occur with prostate cancer. The orange metabolites are in the cytosol and the green metabolites are in the mitochondria. While the diagram illustrates the reactions that affect the various metabolites, it does not document the entire reaction. As a result, several of the reactions are not balanced. AAT: Aspartate Aminotransferase, ACC: Acetyl-CoA Carboxylase, ACL: ATP-Citrate Lyase, CS: Citrate Synthase, FAS: Fatty Acid Synthase, Glut: Glutamate, α-KG: α-Ketoglutarate, LDH: Lactate Dehydrogenase, PDH: Pyruvate Dehydrogenase.

Changes in Glycolysis: A third explanation for the decrease in citrate levels observed in prostate cancer may be an increase in glycolysis that results in an increase in lactate production. ^{18}F-2-deoxy-2-fluoro-D-glucose (FdG) positron emission tomography (PET) studies have shown there is an increase in glucose uptake with prostate cancer that is dependent on the histological grade and clinical stage of the disease (66, 67). In addition, ^{1}H NMR spectroscopic studies performed on extracts of transurethral resection specimens (44) and HR-MAS spectroscopic studies of intact surgical (40) and biopsy (47) samples taken from human prostate tissue have demonstrated significantly higher levels of lactate in prostate cancer samples than in normal prostate samples. Typically, an increase in glycolysis would only cause an increase in lactate production under anaerobic conditions. However, the well known observations by Otto Warburg demonstrated that cancer cells produce high amounts of lactate even when they have plenty of oxygen, a behavior often referred to as the Warburg Effect (68) or aerobic glycolysis (69). More recently, it has been hypothesized that the cellular evolution associated with carcinogenesis selects for lactate-producing glycolytic cells because they can withstand the intermittent hypoxic that malignant cells likely endure and it supports the microenvironmental acidosis they need to breakdown and invade healthy tissues (69). Additionally, the increase in lactate production may provide the parasitic cancer cells with a rapid energy source since the glycolytic production of ATP is 100 times faster than the mitochondrial production of ATP (62). Initially, it may seem rather inefficient to rely on lactate production to generate energy since it requires 18 times more glucose than if the energy were produced within the mitochondria. However, the wasteful consumption of glucose is more of a problem for the neighboring healthy cells, which use the glucose for net citrate production as well as energy production in the case of normal prostatic secretory epithelial cells, than the

parasitic cancer cells. For the parasitic cancer cells, a rapid energy source is likely more important as it supports their primary desire to grow and proliferate (62).

Clearly, there are many metabolic adaptations that may occur as the healthy prostate secretory epithelial cells transform into neoplastic, parasitic cancer cells and may impact the unique ability of healthy prostate secretory cells to produce citrate. At a high level, the decrease in citrate levels associated with prostate cancer could be a result of an increase in citrate oxidation within the mitochondria, an increase in fatty acid synthesis, or an increase in lactate production. Since there is strong supporting evidence for each of these possibilities, it is very likely that prostate cancer development is dependent upon or requires a combination of these metabolic adaptations. For example, it has been hypothesized that the increase in lactate production may also support lipogenesis and fatty acid synthesis by providing a readily available carbon source that can quickly be converted to AcCoA (62). Thus, the increase in fatty acid synthesis and glycolytic production of lactate may be linked to one another. Unfortunately, to date, it has not been possible to directly investigate the metabolic adaptations that may explain the reduction in citrate *in-vivo*. Therefore, it is not known if the mechanisms behind the citrate reduction could provide a more sensitive (able to detect more smaller amounts of disease) and/or specific biomarker for prostate cancer detection and/or therapeutic monitoring than what is currently available. In fact, identifying the actual mechanism in humans may provide a new opportunity for therapeutic intervention if it turns out that the mechanism is essential to the development or progression of the disease. Fortunately, recent advances in high field in-vivo scanners and ^{13}C hyperpolarization techniques may allow the simultaneous investigation of these pathways *in-vivo* by providing a measurement of the metabolism of ^{13}C labeled substrates through these pathways. As result, the overall goal for the studies included in

this thesis will be to investigate how ^{13}C labeled pyruvate could be used to interrogate these metabolic adaptations and to develop clinically translatable measurement techniques for ^{13}C labeled pyruvate and its products.

1.6 Creating Metabolic Tracers for Studying Prostate Biochemistry with ^{13}C Labeling

While ^{12}C is the most common form of carbon, ^{13}C is the isotope of choice for any carbon based NMR experiments because it is the only NMR active (detectable) isotope of carbon. Since ^{13}C, like ^{1}H, possesses a spin ½ nucleus, its nucleus resides in one of two energy states when placed inside of a magnetic field and can be detect using the same NMR techniques developed for ^{1}H. Unfortunately, the natural abundance of ^{13}C is only 1.1%. Even worse, only 0.94% of the atoms in the human body are carbon, often referred to as the biological abundance. Combining these two factors, ^{13}C is only 0.01% of the atoms in a typical human, whereas 63% of the atoms are ^{1}H's. Since the human body contains so much water, ^{1}H NMR has a huge signal to noise ratio (SNR) advantage over ^{13}C NMR. On the flip side, carbon atoms are present in every metabolite found in the human body. Consequently, ^{13}C NMR techniques have been used to investigate non-focal diseases in human beings for many years. In an attempt to overcome the lower SNR of ^{13}C, a typical experiment requires averaging many acquisitions and rather large volumes resulting in long scan times and poor spatial resolution. Additionally, many biologically relevant compounds have been synthetically enriched with ^{13}C to 99% and can be purchased from Isotec, a subsidiary of Sigma-Aldrich, or Cambridge Isotope Laboratories. With the added SNR from the enriched substrate, it has been possible to perform kinetic metabolic studies *in-vivo* following the infusing of a synthetically enriched compound. A typical infusion study involves infusing a synthetically enriched, metabolic active substrate, such as glucose, and following it through the pathway of interest by measuring the increase in the ^{13}C signal from a downstream metabolite, such as

glutamate. The low natural abundance of ^{13}C is actually beneficial for these studies because it ensures that the majority of the recorded ^{13}C signal is from the synthetically enriched substrate and its products because the background or baseline ^{13}C signal is very small. Furthermore, the relatively small atomic mass difference between ^{12}C and ^{13}C ensures that the ^{13}C labeled compound will be metabolized in the same manner as its ^{12}C counterpart.

Despite the long history of ^{13}C NMR and MR, it has not yet been used to investigate the metabolic adaptations that may occur as secretory prostatic cells transform into malignant cancer cells. Since all the metabolic adaptations described in the previous section have glycolysis as a common starting point, it should be possible to simultaneously investigate these three proposed changes by incorporating a ^{13}C label into glycolysis. For example, ^{13}C-1 pyruvate would produce C-1 labeled lactate if the pyruvate were converted to lactate or ^{13}C labeled bicarbonate (derived from CO_2) if the pyruvate were converted to AcCoA and subsequently oxidized in the citric acid cycle or ultimately used for fatty acid synthesis as shown in Figure 1.4. ^{13}C-2 or ^{13}C-3 pyruvate would provide an even more detailed interrogation of the potentially aberrant pathways in that the label could be directly followed into lactate, a citric acid cycle intermediate such as glutamate, or a fatty acid synthesis intermediate such as AcCoA as shown in Figure 1.4. These pyruvate derivates could be used as reporter metabolites to noninvasively detect an increase in glycolytic lactate production, an increase in citrate oxidation in the TCA cycle, or an increase in fatty acid synthesis, respectively. A direct measure of these pathways in-vivo will improve the understanding of the mechanisms that cause the reduction in citrate that occurs with prostate cancer development and evolution. More importantly, the experiments may reveal a new biomarker for prostate

cancer detection and/or therapeutic monitoring that is more sensitive and/or specific than the current biomarkers.

Investigating the aberrant metabolic pathways in prostate cancer with ^{13}C labeling will require navigating around a few obstacles, as is often the case in research. The gyromagnetic ratio (usually denoted γ) for ^{13}C is ¼ the γ of ^{1}H causing its resonant frequency to be ¼ that of ^{1}H. The large difference in resonant frequency requires fabricating or procuring a special RF coil that functions at the ^{13}C frequency. In practice, it is usually necessary to have both a ^{1}H RF coil to obtain anatomical information and a ^{13}C RF coil to record the carbon data. Furthermore, in high-resolution NMR and HR-MAS, the SNR is proportional to $\gamma_E * \gamma_O^{1.5}$, where γ_E and γ_O are the gyromagnetic ratio for the excited and observed nucleus, respectively. Therefore, the SNR for ^{13}C will be another factor of 32 lower than that of ^{1}H, in addition to the reduction caused by its lower natural abundance and biological abundance of ^{13}C. In the case of *in-vivo* MRI and MRSI, the SNR is proportional to $\gamma_E^{0.5} * \gamma_O^{1.5}$, resulting in ^{13}C being another factor of 16 lower than that of ^{1}H. Since the thermal MR noise produced by the sample is the dominant noise source for *in-vivo* MR and it increases with γ, the *in-vivo* SNR is slightly less dependent on γ than the high-resolution SNR causing the SNR difference between ^{13}C and ^{1}H to be smaller. For high-resolution experiments, the dominant noise source is the RF coil and the electronics. In the past, synthetically enriched substrates have been infused in an attempt to improve the SNR of ^{13}C experiments. While the enriched substrates have reduced the scan times and/or increased the spatial resolution for ^{13}C studies, the scan times and spatial resolution have not been sufficient for routine clinical use. More recently, new developments in hyperpolarization techniques and improvements in high field *in-vivo* scanners have invigorated ^{13}C MR and NMR with new enthusiasm.

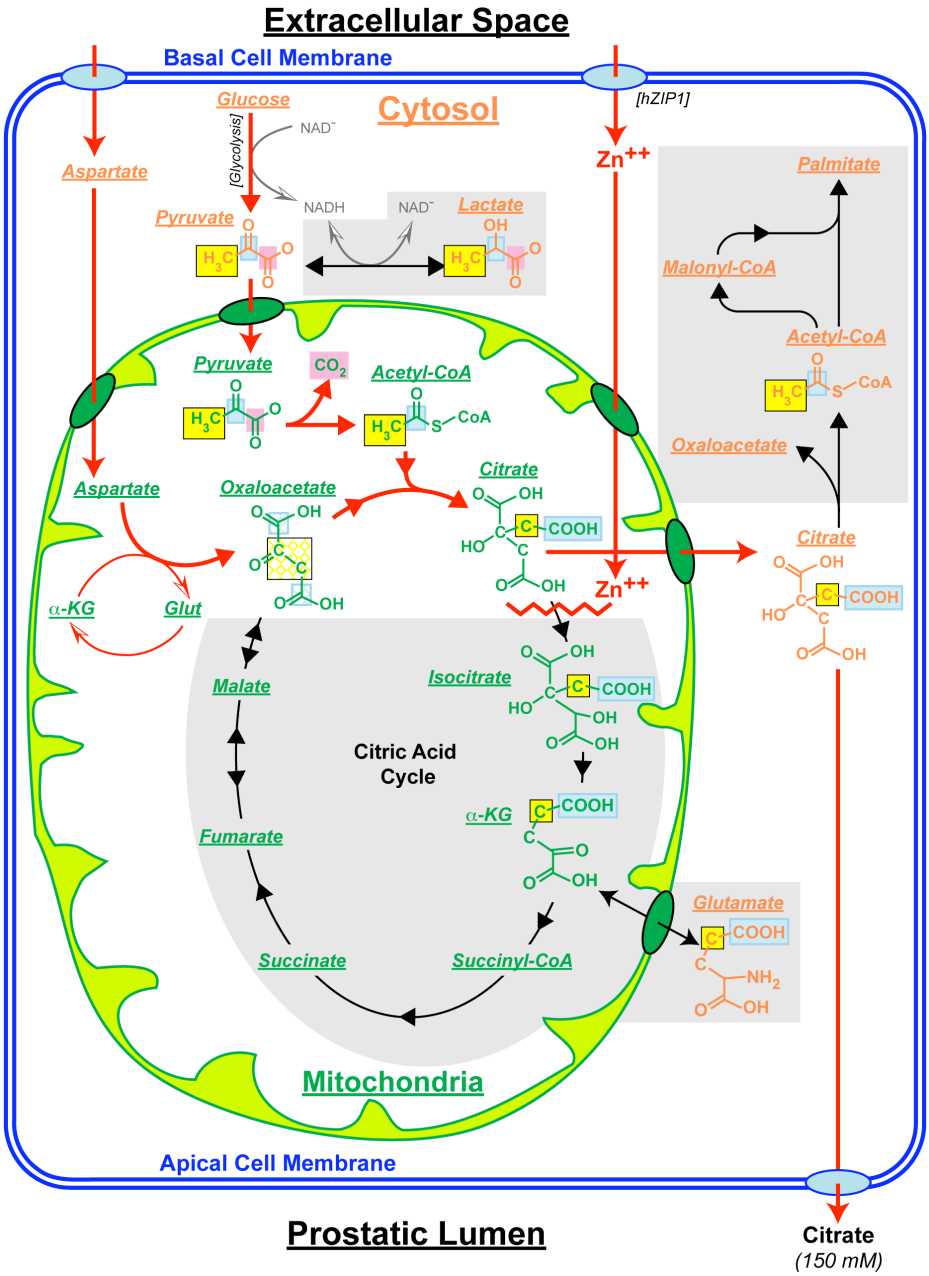

Figure 1.4 Diagram of the fate of ^{13}C labeled pyruvate in the pertinent intracellular metabolic pathways that exist in secretory prostatic cells. The pink, blue, and yellow boxes highlight the fates of ^{13}C-1, ^{13}C-2, and ^{13}C-3 pyruvate, respectively, as they pass through the various pathways. The hatched yellow and blue boxes on oxaloacetate indicate which positions will be labeled if it is derived from malate following the incorporation of a ^{13}C labeled pyruvate molecule. The labeling of oxaloacetate in this case is split between two carbon positions because succinate is a symmetric molecule. The red lines represent the pathways that are active in healthy secretory prostatic cells and the black lines along with the gray background highlight the metabolic adaptations proposed to occur with prostate cancer. While the diagram illustrates the reactions that affect the various metabolites, it does not document the entire reaction. As a result, several of the reactions are not balanced. Glut: Glutamate, α-KG: α-Ketoglutarate, Zn: Zinc.

Chapter 2
Studying Prostate Biochemistry Using ^{13}C Labeled Metabolic Substrates

The use of ^{13}C labeled pyruvate appears to be very promising approach for investigating the metabolic adaptations proposed to occur with the development and evolution of prostate cancer. In an attempt to explore these possibilities, the metabolism of ^{13}C labeled pyruvate will be investigated in two newer prostate cancer model systems. For the first round of experiments, ^{13}C-3 pyruvate will be added to the culture medium for primary cultured human prostate cancer cells and prostate tissue slices. The ^{13}C labeling of pyruvate and its metabolic products will be measured using HR-MAS spectroscopy after the culture samples have been quickly frozen. For the second set of experiments, pyruvate will be injected into anesthetized, transgenic mice that develop prostate cancer. The uptake of the hyperpolarized pyruvate and its metabolic conversion will be measured in real time using MR spectroscopy. In this chapter, a brief description of HR-MAS and ^{13}C hyperpolarized imaging techniques will be given, along with an overview of ^{13}C labeling experiments used for each set of experiments.

2.1 Measuring Incorporation of ^{13}C Labeled Metabolic Substrates in Model Systems using HR-MAS

High Field and HR-MAS Background

Since the advent of nuclear magnetic resonance, the quest to improve the sensitivity of the technique has motivated the use of magnets with stronger magnetic fields (B_0) because the SNR of NMR spectroscopy is directly proportional to $B_0^{3/2}$. As a side note, in theory, the SNR for a whole body MRI is directly proportional to B_0. The SNR of whole body MR measurements is slightly less dependent on B_0 because the noise is dominated by sample noise. At any rate, the stronger magnetic fields have also improved the spectral resolution of NMR and MR spectra. This benefit is easily

understood by reviewing the relationship that defines the resonant frequency (ω) of a nucleus when it is exposed to an external magnet field

Eq. [2.1] $$\omega = \gamma B_0(1 - \sigma)$$

where γ is there gyromagnetic ratio for that nucleus and σ is the molecule specific shielding constant for that nucleus. Since the shielding is produced by the electrons in the electron cloud surrounding the nucleus, the shielding constant is not only nuclei dependent, it is also affected by the neighboring atoms in the molecule and their impact on the electron cloud's density and shape. The difference in the resonant frequency ($\Delta\omega$) for two like nuclei that have different shielding constants (σ_1 and σ_2) can be calculated by subtracting the resonant frequencies that were determined for the two nuclei by using Eq. [2.1].

Eq. [2.2] $$\Delta\omega = \gamma B_0(\sigma_1 - \sigma_2)$$

Since the difference in the resonant frequencies of the nuclei scales linearly with B_0, an improvement in the spectral resolution is observed in the spectrum. While the improvement in spectral resolution is very evident in spectra obtained from solution samples, it is not so obvious in spectra from tissue samples because the increase in B_0 also increases the effect of chemical shift anisotropy (CSA), leading to an decrease in the nucleus' T_2 and an increase in its spectral line width. CSA occurs when the σ in Eq. [2.1] is dependent upon the orientation of the molecule relative to the external magnetic field. This situation can occur whenever the electron cloud surrounding a nucleus is not spherical and the molecule's mobility is restricted either because the molecule's mass or because its environment is hindering its motion. For most molecules, the electron clouds surrounding its nuclei are not spherical and the net magnetic field experienced by

the nucleus is orientation dependent. However, as long as the molecule is tumbling at a fast rate relative to the timescale of the NMR experiment while it is inside the magnet, the observed shielding constant is a weighted average of the shield constants for each orientation. Whereas, when the molecule's motion is restricted, the different shielding constants for the molecule are actually observed in the NMR experiment, resulting in a broadening of the molecule's linewidth in the frequency domain (70). In these cases, the σ in Eq. [2.1] becomes a tensor ($\bar{\sigma}$) and was defined by Andrew (71) as:

Eq. [2.3] $$\sigma_{Avg} = \frac{1}{2}\sin^2(\beta) * \mathrm{tr}(\bar{\sigma}) + \frac{1}{2}\left[3\cos^2(\beta) - 1\right]\sum_p \sigma \cos^2(\chi_p)$$

σ_{Avg} is the time average of σ. β is the angle of the sample's primary axis relative to the axis of the magnetic field. χ is the azimuthal angle between the primary axis of $\bar{\sigma}$ and the axis of the magnetic field. As shown in the top portion of Figure 2.1, increasing the magnetic field strength to 11.7 T permits the observation of several metabolites that are not easily observed in 1.5 T spectra of tissue. However, the resonances are still relative broad because of CSA. Since the CSA is virtually nonexistent for small molecular weight compounds in solution, it can almost be eliminated from the tissue spectra by using perchloric acid extracts of the tissue as previously shown (44-46). Unfortunately, labile metabolites can be lost during extraction. In addition, the extraction requires rather large amounts of tissue for each sample and, it makes it impossible to histologically analyze the tissue sample since it is digested as part of the extraction process.

HR-MAS is another technique that reduces CSA by spinning the sample at an angle (54.7°) relative to the main field (B_0), referred to as the magic angle. Generally speaking, Magic Angle Spinning (MAS) is a technique applied to solid samples, and it

reduces the impact of CSA and dipolar interactions on the measured spectra from these samples (71-73). For MAS, the samples are held at the magic angle inside the magnet and spun about this slanted axis at very high speeds, typically between 20 and 70 kHz. HR-MAS is the slow speed counterpart of MAS because it typically involves spinning the sample at 500 to 5,000 Hz. At these spin rates, the CSA of small molecules present in tissue samples can be significantly reduced, which can be understood using Eq. [2.3]. When β in Eq. [2.3] is set to 54.7°, σ_{Avg} reduces to

Eq. [2.4] $$\sigma_{Avg} = \frac{1}{3}\,\mathrm{tr}(\bar{\sigma}) = \sigma$$

Thus, the observed shielding constant for these molecules (σ_{Avg}) under HR-MAS conditions is equivalent to the molecule's shielding constant when it is in solution, despite the presence of CSA. Qualitatively, the magic angle is the diagonal of a cube and it has the unique property that the effect of CSA is averaged away when the sample is spun fast enough about this angle.

After comparing the HR-MAS and standard NMR spectra from rat brain tissue in Figure 2.1, it is clear that HR-MAS substantially improves the spectral resolution of high field tissue spectra. The high spectral resolution enables the quantification of compounds with similar chemical shifts. For example, choline can be distinguished from the other choline containing compounds (glycerophosphocholine (GPC) and phosphocholine (PC)). In addition, this approach is completely nondestructive to the tissue if performed at low enough spin rates and, the high filling factor achieved with the HR-MAS probe permits measurement of metabolites from small samples, ranging from 3 to 40 mg. Swanson *et al.* have shown that ^{1}H HR-MAS can be used to detect the known metabolic changes in prostate cancer (decreased citrate, decreased polyamines,

increased choline containing compounds, etc.). Furthermore, they were able to correlate the metabolic changes with the histopathological analysis performed on the same prostate tissue samples following the HR-MAS experiments (35). Therefore, by using HR-MAS, spectra with great spectral resolution (narrow peaks with large separations) can be generated from small tissue samples and correlated with quantitative histopathology data.

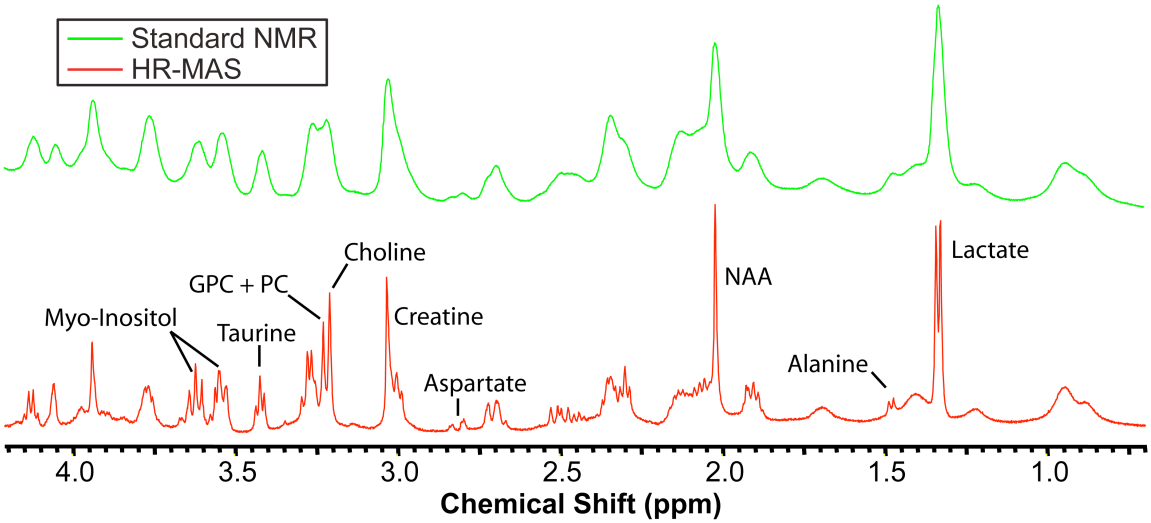

Figure 2.1 High resolution NMR spectra recorded from rat brain cortex at 11.7T after it was placed in an NMR tube *(TOP)* and under HR-MAS conditions *(BOTTOM)*. The spectrum acquired using HR-MAS exhibits a significant reduction in chemical shift anisotropy as demonstrated by the decrease in the linewidth of N-Acetyl-Aspartate (NAA) from 17.4 to 4.3 Hz.

Incorporating and Measuring ^{13}C Labeling in Prostate Cell and Tissue Cultures

Using the current culture techniques, it is possible to grow human prostate cancer cells and prostate tissue slices in primary culture. Since primary cultures have not been immortalized, they more accurately represent the cells and tissue type from which they were derived. Both culture techniques begin with a radical prostatectomy being performed on a prostate cancer patient. Once the man's prostate has been surgically removed, the cells or tissue are harvested from the region of interest in the prostate specimen. The cells or tissue are then cultured in a serum-free medium that has been

supplemented with a custom blend of nutrients and growth factors (74). Peehl et al. developed the custom medium specifically for the primary culture of prostate epithelial cells. Using the custom medium it has been shown that the prostate epithelial cells can be grown in primary culture for approximately 30 days, during which they will double in number every 24 hours (75, 76). Similarly, functional prostate tissue slices have been maintained in the custom medium for up to 5 days (77).

These prostate model systems provide a great platform for conducting the ^{13}C labeling experiments described in Chapter 1 since the ^{13}C labeled pyruvate can be delivered to the cells or tissue by simply adding it to their medium. Additionally, it is easy to control and vary the amount of labeled pyruvate delivered to the cells or tissue as it only requires varying the pyruvate concentration in the medium. Therefore, the metabolic adaptations described in Chapter 1 will be investigated in these two prostate model systems by adding ^{13}C-3 pyruvate to their media. After the culturing is complete, the cells or tissue slices will be rinsed, quickly frozen, and stored at -80°C. While the culture process will be described in more detail in Chapter 4, it is important to point out that the samples must be rinsed to remove the residual culture medium from the sample. Otherwise, its component molecules will contaminate the HR-MAS spectra. The optimal washing procedure and culture duration for these experiments will be described in Chapter 4. By cooling the samples down immediately after the culture process was completed and storing the samples at -80°C, the cells or tissue should have minimal to no metabolic activity during this time. As a result, the samples' metabolite levels and their ^{13}C labeling should represent the metabolism that occurred during the culture process and not any aberrant metabolism that could have occurred while samples were being harvested or stored.

Ultimately, the amount of activity in the metabolic pathways of interest will be measured using HR-MAS spectroscopy to analyze the samples. At the time of the HR-MAS experiment, the cell or tissue samples will need to be transferred to the HR-MAS rotor (sample holder) shown in Figure 2.2. Ideally the sample will be kept frozen during the transfer to simplify the process and to minimize any metabolism that may occur during the transfer. In order to achieve this goal, the cell and tissue samples were stored in custom sample holders, as described in Chapter 4, which as part of the harvesting procedure molded the samples into a shape that was similar to the shape of the sample cavity in the HR-MAS rotors. Additionally, the custom sample tubes were designed to facilitate transfer of the frozen samples into an HR-MAS rotor in 30 s or less. Once the sample was loaded into the HR-MAS rotor and positioned inside the magnet, it was spun about the magic angle at 2,250 Hz and maintained at 1°C. By keeping the sample at 1°C, the metabolic activity of the cells or tissue was reduced as much as possible without freezing the sample. Unfortunately, once the sample becomes a solid, the CSA and dipole-dipole interactions significantly increase resulting in extremely short T_2's. Therefore, the sample was cooled down as much as possible without freezing them. The HR-MAS spin rate was chosen as a compromise between mechanical degradation imposed on the tissue by the centrifugal force of the spinning, the overlap of spinning side bands with metabolites of interest, and the reduction of CSA and associated increase in T_2 provided by HR-MAS. At higher spin rates, more of the molecules' CSA is removed from the experiment, along with the dipole-dipole interactions at extremely high spin rates. The higher spin rates also increase the spacing of the spinning sidebands observed in HR-MAS spectra, which occur at the frequency of the nuclei's primary resonance determined by Eq. [2.1] plus/minus integer multiples of the spin rate. Unfortunately, the high spin rates also degrade the tissue, leading to metabolic profiles that are different from those measured in *in-vivo* conditions

and eliminating the possibility of histologically and/or genetically analyzing the tissue after the HR-MAS experiment. Swanson et al. have shown that it is possible to record high quality high-resolution spectra at 11.7 T by spinning the sample at 2,250 Hz and to subsequently obtain high quality histopathological analysis from the same samples (35, 40). Furthermore, at this spin rate, the spinning sidebands are 4.5 ppm apart in a 500 MHz spectrometer. Since the dominant metabolite resonances span a 3.2 ppm range in the ^{1}H spectrum and are within 4 ppm of water, no significant spinning sidebands overlap with the metabolites of interest at this spin rate.

Figure 2.2 Photograph of an HR-MAS rotor. The rotors consisted of a T-shaped zirconium base, a plastic collar with machined groves on the underside, and an opaque plastic insert fitted with a rubber O-ring and a threaded head. The insert mated with the plastic collar and provided a leak proof seal for the rotor. The groves in the collar served as a turbine and caused the rotor to spin when air was blown across it (40).

The amount of ^{13}C labeling present in the samples was evaluated by estimating the concentration of the ^{13}C labeled pool for the reporter metabolites along with fractional enrichment of these metabolites. While a detailed description for these calculations will be presented in Chapter 4, for now it is sufficient to point out that computing the fractional enrichment requires a measurement of the metabolite concentrations and the concentrations of the ^{13}C label pools for the metabolites. Furthermore, as mentioned in

Chapter 1, ^{13}C spectroscopy of biological specimens is severely SNR limited. Since the SNR of high resolution spectroscopy is proportional to $\gamma_E * \gamma_O^{1.5}$ and γ of ^{13}C is ¼ the γ of ^{1}H, the SNR of the ^{13}C measurements can be improved by a factor of 32 if ^{1}H's are excited and observed instead of ^{13}C nuclei. However, in order for this to provide a measure of the ^{13}C labeled pools, the detected or observed ^{1}H's must be weighted by the presence of a ^{13}C atom, an approach referred to as indirect detection. One such NMR experiment that achieves this goal is the heteronuclear single quantum coherence (HSQC) experiment. Since the HSQC detects the presence of ^{13}C atoms through their directly attached ^{1}Hs, the metabolites of interest must be ^{13}C labeled in carbon positions that have directly attached ^{1}Hs. By using the ^{13}C-3 pyruvate as the ^{13}C labeling substrate this will be the case for all the reporter metabolites. Therefore, the HR-MAS spectroscopy protocol used for the experiments described in Chapter 4 will consist of a ^{1}H spectrum to provide a measure of the total metabolite pools and a ^{13}C HSQC spectrum to provide a measure of the ^{13}C labeled metabolite pools. As a quality assurance measure and a sanity check, a second ^{1}H spectrum was acquired after the rather time consuming HSQC experiment, which was used to quantify any changes in metabolite concentrations that might have occurred during the HR-MAS experiments. Since the ^{1}H spectra from prostate tissue are already relatively crowded, the spectra were acquired with ^{13}C decoupling. The decoupling has the added benefit of increasing the individual peak SNR for the ^{13}C labeled resonances by combining the J-coupled resonances. The optimal ^{13}C decoupling scheme for these experiments will be described in Chapter 3

In order to calculate concentrations from the HR-MAS spectra recorded from the prostate cell and tissue cultures, it was necessary to add a quantification reference signal to the spectra. The Electronic Reference To access In-vivo Concentrations

(ERETIC) method produces an electronically generated reference signal that has been shown to provide an accurate and stable quantification reference for high resolution NMR spectra (78). In Chapter 3, the implementation of the ERETIC method on a Varian Inova console is described, and the method is evaluated as a quantification reference for HR-MAS spectra. Since this quantification reference was not available for the prostate cancer cell experiments conducted in Chapter 4, the HR-MAS spectra were quantified using a reference compound, ^{13}C-glycine, that was added to samples at the time of the HR-MAS experiments.

2.2 Measuring Incorporation and Metbolism of ^{13}C Labeled Substrates in Live Transgenic Mice using Hyperpolarization

The ^{13}C HR-MAS experiments performed on the prostate cancer cell culture and prostate tissue culture samples will provided useful information about the relative importance of the metabolic adaptations that have been proposed to occur with prostate cancer development and evolution. However, the experiments did not permit a real time measurement of the metabolism of the ^{13}C labeled pyruvate and, the HSQC is too time consuming to be carried out *in-vivo*. In order to obtain a real-time measurement of the metabolism in-vivo with ^{13}C, the SNR of the ^{13}C labeled metabolites must be significantly enhanced. Fortuitously, ^{13}C hyperpolarization techniques have been recently developed that may provide the SNR boost required to make these experiments a reality.

Motivation and Background for Hyperpolarization

The signal intensity produced by a population of nuclei exposed to an external magnet field is directly influenced by several factors as indicated in Eq. [2.5].

Eq. [2.5] $$\text{Signal} \propto \mu \times \omega_0 \times V \times \left[C\right] \times FE \times P$$

where μ is magnetic moment of an individual nucleus, ω_0 is the resonant frequency of the nucleus determined using Eq. [2.1], [C] is the concentration of the nuclei in a volume

(V), FE is the fractional enrichment of the nuclei or the percentage of the nuclei that are NMR active, and P is the polarization of the nuclei or the percentage of the extra nuclei that are aligned with B_0 as defined in Eq. [2.6].

Eq. [2.6]
$$P = \frac{N^- - N^+}{N^- + N^+}$$

N^+ and N^- are the number of nuclei anti-aligned with B_0 and aligned with B_0, respectively. Looking at the values of the parameters in Eq. [2.5] for some typical molecules of interest in human prostate tissue, it is obvious that the signal intensities for metabolites are tiny compared to the signal intensity of water because of the huge reduction in the [C] x FE x P product for metabolites (Table 2.1). The situation only gets worse when measuring the metabolites using ^{13}C instead of ^{1}H. As was mentioned in Chapter 1, the signal intensity for ^{13}C metabolic studies can be improved by injecting ^{13}C enriched metabolic substrates. While the enriched substrates will likely improve the ^{13}C signal from metabolites by a factor of 10-50, the improvement is miniscule compared to the 10^3 reduction in NMR signal obtained from lactate when measured with ^{13}C NMR instead of ^{1}H and the 10^8 reduction in signal intensity relative to the water signal (Table 2.1).

One reason the signal level from NMR is rather low is that the nuclear polarizations are ridiculously low at body temperature. From the data in Table 2.1, the nuclear polarization of ^{1}H and ^{13}C in a 3.0 T magnet field at 37°C are 9.34e-6 and 2.34e-6, respectively, or just 0.000934 and 0.000234%. The polarization of NMR active nuclei in an external magnet field is a function of μ, B_o, the Boltzmann constant (k_B), and the sample's temperature (T) as indicated in Eq. [2.7].

Eq. [2.7]
$$P = \tanh\left(\frac{\mu B_0}{k_B T}\right)$$

Based on this relationship, the polarization can be increased by increasing the magnetic field strength, by using a particle with a larger magnetic moment, or by decreasing the temperature. As shown in Figure 2.3, the polarization increases linearly on a log-log plot as the sample is cooled down. However, the sample temperature must be reduced by 4 orders of magnitude to the millikelvin range in order to increase the polarization of the ^{13}C or ^{1}H nuclei by 4 orders of magnitude. Interestingly, since the μ of an electron is 2,628 times larger than μ of a ^{13}C nucleus, electrons in a 3.35 T magnetic field are nearly 100% polarized at just 1°K. While this is a very cold temperature, it is far more obtainable than nearly absolute zero temperatures because helium, a liquid when kept between 0 and 4 °K, is already used to cool most superconducting NMR and MR magnets to 1 - 4°K. Therefore, if it were possible to cool the sample to 1°K and transfer the polarization from the electrons in the sample to the ^{13}C nuclei, a radical improvement in the polarization of the ^{13}C nuclei could be achieved. By combining this approach with synthetically enriched ^{13}C labeled substrates, it is possible to increase the [C] x FE x P product and consequently the MR signal by 10^5 to 10^6 for the polarized substrate and/or its metabolic products.

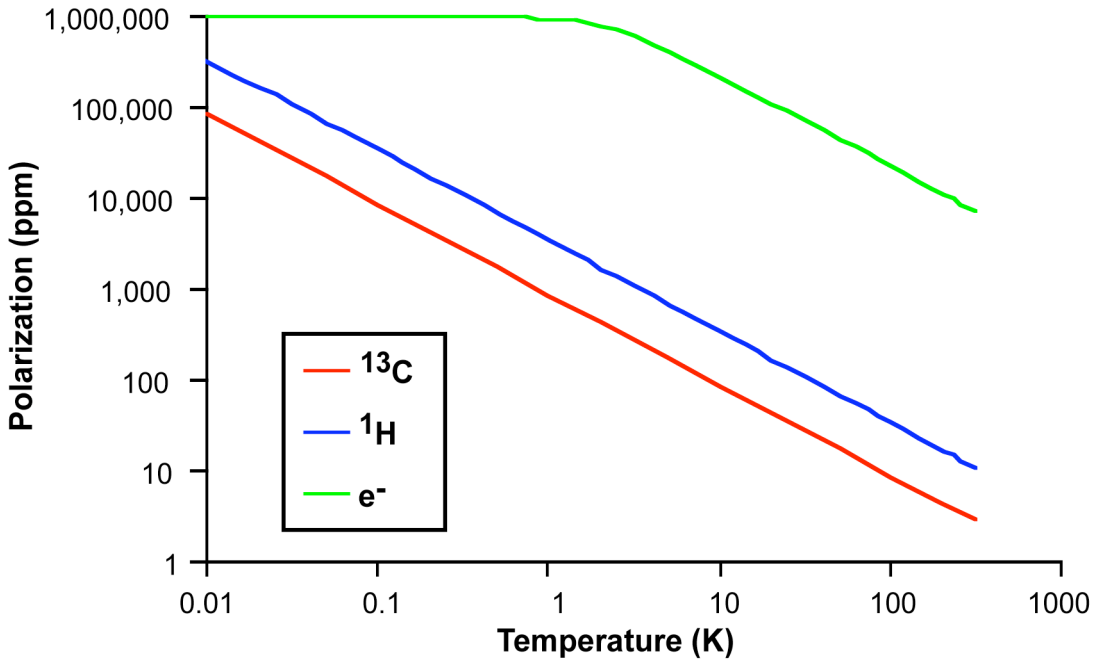

Figure 2.3 Thermal polarization for ^{13}C nuclei, ^{1}H nuclei, and electrons (e^-) when they are exposed to a 3.35 T external magnetic field. The polarizations were computed using Eq. [2.7].

Molecule	Nucleus	[C]	FE	P	[C] x FE x P
Water	^{1}H	~110M	99.985	9.34E-06	1.03e-1 M
Lactate	^{1}H	~3mM	99.985	9.34E-06	2.80e-6 M
Lactate	^{13}C	~1mM	1.11	2.34E-06	2.60e-9 M

Table 2.1 Key biological and NMR properties for water and lactate in humans. The concentrations ([C]) refer to the concentrations of the specified nucleus within the molecule of interest. In the case of lactate, the concentrations are for C-3 lactate. Since these values are for natural conditions, the fractional enrichment (FE) values are equivalent to the nuclei's natural abundance. The polarization values (P) were determined using Eq. [2.7] and assuming the nuclei were in a 3.0 T magnetic field at body temperature (310°K).

Dynamic Nuclear Polarization (DNP) is a polarization technique that is based on the concept of transferring the polarization from the electron's to the nuclei of interest at approximately 1°K. For DNP, the polarization substrate must be doped with unpaired electrons prior to cooling the substrate. This is usually done by adding an organic free radical to the polarization substrate. In addition, the radical must be homogeneously

distributed throughout the polarization sample for efficient polarization of it, which requires that the sample form an amorphous solid when it is cooled to 1°K. If the substrate does not do this naturally, a glassing agent must be added to the sample (79). Once the sample has been prepared, it must be cooled to ~1°K and exposed to an external magnetic filed. At the moment, this has been accomplished using a NMR magnet customized by adding a variable temperature insert (VTI) to the bore of the magnet which can be filled with liquid helium and pressurized (79). Using one of these polarizers with a magnetic field strength of 3.35 T, the sample is lowered into the liquid helium bath in the VTI and cooled to 1.1 – 1.4°K by lowering the pressure in the VTI. Since the unpaired electrons are briefly coupled to the protons in the sample, the nuclear polarization can be increased by stimulating the sample at a frequency equal to the difference in the resonant frequency of the electrons and the protons (from the nuclei of interest), which is ~94 GHz at 3.35 T. As a result, the polarizer is also equipped with a microwave source and transmission system that can irradiate the sample with a 94 GHz signal while it is in the VTI (79). The microwave stimulation converts an electron aligned with the external field and a proton anti-aligned with the field to an anti-aligned electron and an aligned proton. After the electron relaxes back to the aligned state, the process can be repeated again with another anti-aligned proton, resulting in an increase in the proton polarization. Since the electron polarization in the sample is very high and it relaxes back to the aligned state very quickly (T_1 ~ 1 μs), the polarization of the protons can be significantly increased for protons with long T_1's at ~1°K.

In order for the substrate to be used for biological experiments, it must be converted to an injectable form and warmed to the appropriate temperature without losing the polarization. Ardenkjaer-Larsen and co-workers have developed an apparatus that accomplishes this by dissolving the polarized sample with a hot solvent

while the sample is still inside the VTI. The apparatus mates with the sample holder inside the VTI and uses pressurized helium gas to force the hot solvent through a small diameter tube and mix the solvent with the sample (79). The warm solution is forced out of the VTI though a second tube and collected in a glass flask in ~ 10 s. Since the solvent contains a buffering system the pH of the final solution is neutralized and appropriate for injecting into a living organism. Similarly, the temperature of the solvent is such that once it is mixed with the frozen substrate, the temperature of the final solution is approximately 37°C. Therefore, the solution contains a substrate with a substantially enhanced nuclear polarization and is ready for injection. In theory, DNP can be performed on any NMR active nuclei. In practice, ^{13}C-1 pyruvate, ^{13}C urea, and ^{13}C-1 cyclo-propane have been polarized to 10 – 20% using DNP (80-83). As the technology is commercialized by GE Healthcare and Oxford Instruments, the technique will become readily available and it will likely be possible to produce ~20 mmol of hyperpolarized compound per hour with a single DNP system.

While DNP appears to be a very promising technique for hyperpolarizing a compound and producing an injectable solution, there are other techniques that may provide alternatives for hyperpolarization. As indicated in Eq. [2.7] and the plot in Figure 2.3, the polarization can be increased by decreasing the sample's temperature and increasing the magnetic field strength, the so called "Brute-Force" technique. Brute-force polarization is universally applicable and can be applied to all NMR active nuclei and all molecules. However, using magnetic field strengths available today, it requires cooling the sample to temperature very close to absolute zero in order to produce the hyperpolarization needed for ^{13}C labeled metabolic studies. In addition, the T_1's of the nuclei increase as the temperature is decreased, making the polarization times longer as the temperature is lowered. As a result, it has not been practical to use the brute-force

technique to routinely hyperpolarize samples. Another hyperpolarization technique involves incorporation of parahydrogen into the molecule of interest through catalytic hydrogenation and is referred to as ParaHydrogen-Induced Polarization (PHIP) (84, 85). The spin order in the resulting molecule is then used to polarize the nuclei of interest by cycling the magnetic field (86, 87). The technique requires less sophisticated equipment than DNP and is capable of polarizing a sample in a few seconds (88). Unfortunately, the substrate molecule must incorporate the nuclei of interest with a double or triple bond in order for the nuclei to be bonded with the parahydrogen at the time of polarization. As a result, PHIP can only be used to polarize ^{13}C, ^{15}N, and ^{1}H nuclei and only molecules that contain double or trip bonds. Since DNP can be applied to a broader range of molecules and nuclei and the polarizer is commercially available, it was used for the *in-vivo* hyperpolarized ^{13}C labeling studies included in this project.

Using Dynamic Nuclear Polarization to Investigate Prostate Cancer In-Vivo

Even though access to the DNP technology has been somewhat limited since its first *in-vivo* application was demonstrated four years ago (80), numerous studies have been published since that time. ^{13}C urea and ^{13}C-1 cyclo-propane have been hyperpolarized and used for coronary imaging, angiography, and perfusion imaging in rats (80, 81, 89). Hyperpolarized ^{13}C-1 pyruvate has been injected into rats and pigs and provided a measure of metabolic differences between tumors and muscle, metabolic differences between normal liver, kidney, and muscle, and therapeutic response in lymphoma (82, 83, 90-92). Typical polarizations for these studies were between 12 and 25%, providing sufficient SNR for *in-vivo* imaging at a resolution of ~0.135 cc. Although, the T_1 of the hyperpolarized nuclei and its products was a very important consideration for these studies because the polarization was exponentially reduced to the thermal equilibrium polarization with a time constant of $1/T_1$. While DNP can be used to polarize

any NMR active nuclei in any molecule when it is cooled to 1°K, the molecule is only useful for biological experiments if the polarization lasts for enough time after it has been dissolved to conduct the experiment. In response to this limitation, most of the *in-vivo* hyperpolarization studies to date have polarized ^{13}C labeled substrates in which the ^{13}C nucleus is rather distant from any fast relaxing nuclei such as ^{1}H's. The ^{13}C nuclei in these molecules often have T_1's on the order of 60 seconds and are capable of producing detectable signal *in-vivo* for several minutes as shown in Chapter 5.

As mentioned in section 1.6 and shown in Figure 1.4, ^{13}C-1 pyruvate could be used to investigate whether or not prostate cancer is connected with an increase in glycolytic lactate production. If pyruvate continues to enter the citric acid cycle in prostate cancer, the ^{13}C labeled carbon of pyruvate would be detected as bicarbonate. Additionally, ^{13}C-1 pyruvate is an excellent candidate for DNP experiments because it has a rather long T_1. Therefore, ^{13}C-1 pyruvate was polarized using DNP and injected into anesthetized transgenic mice that spontaneously develop prostate cancer. For these studies, synthetically enriched ^{13}C-1 pyruvic acid was mixed with the trityl radical (tris(8-carboxy-2,2,6,6,-tetra(methoxyethyl)benzo[1,2-d:4,5d′]bis(1,3)dithiole-4-yl)methyl sodium salt) (GE Healthcare, Oslo, Norway), which provided the unpaired electrons needed for DNP, and polarized using the DNP technique just described. The polarized substrate was quickly dissolved with a pH balanced TRIS buffer and injected into the transgenic mice. ^{13}C MR spectra were acquired from mice with different histologically classified stages of prostate cancer using a whole body 3T MR scanner. The spectra were quantified and signal levels of hyperpolarized ^{13}C-1 pyruvate and its metabolic products were compared across the histologically defined groups. A detailed description of the experiments and the results is presented in Chapter 5.

Chapter 3
Development of HR-MAS Techniques Necessary for Measuring and Quantifying Metabolism of ^{13}C Labeled Compounds

3.1 Quantification References for One Dimensional ^{1}H HR-MAS Spectroscopy

High resolution magic angle spinning (HR-MAS) spectroscopy is a rapidly developing technique that allows solution-like NMR spectra to be obtained from intact tissue specimens while preserving the tissue for further pathologic and genetic study (35-42). The measurement of absolute metabolite concentrations in tissue would provide important biochemical information and allow changes in individual metabolites to be compared directly between samples. Current methods of quantification often rely on relative ratios of metabolites, which are not ideal since they do not permit detection of individual metabolite changes that may occur with a particular disease state. Furthermore, metabolite ratios can yield ambiguously high or low values when one metabolite peak area approaches zero and thus skew the average among many samples. The measurement of absolute concentrations requires the presence of an endogenous reference, such as tissue water (36), or the addition of an external or internal reference standard to which other metabolites can be compared. Unsuppressed water is not ideal for quantitation because the water signal intensity is typically 1,000 to 10,000 times larger than the most concentrated metabolite in tissue and it assumes that the density of water does not change between pathologies. External silicone rubber beads produce an NMR signal close to 0 ppm (39, 93), but the peak area varies with spin rate and therefore must be calibrated (94). Additionally, the bead must be embedded in an insert, which isolates it from the tissue sample inside the HR-MAS rotor. Although these inserts reliably secure the silicone bead in the rotor and improve the B_0 homogeneity, tissue and associated fluids can be trapped under the insert, leading to cross contamination between samples.

Numerous internal chemical standards (e.g., formate, 3-(trimethylsilyl)propionic-2-2-3-3-d4 acid (TSP)) have also been described for quantitative analysis in conventional solution NMR and HR-MAS spectroscopy (95). An ideal internal standard in tissue should be highly reproducible from sample to sample, non-toxic to the tissue or cells in the sample, chemically inert (metabolically inactive), non-volatile, and nonhygroscopic. It should also resonate at a frequency that does not overlap with other peaks, possess a sufficiently long T_2 to allow good signal detection, and possess a short enough T_1 to prevent signal saturation when using a repetition time (TR) appropriate for the tissue. Unfortunately, most internal standards evaluated to date do not meet all of these criteria. Formate is metabolically inactive and reproducible; however, the T_1 and T_2 relaxation times of formate are much longer than those of endogenous metabolites and must be corrected for when analyzing the data (96). TSP is metabolically inactive, is non-toxic, and has desirable T_1 and T_2 relaxation times. While it has been used as a quantification reference in HR-MAS spectroscopy of tissue (40), there are concerns about its reproducibility due to protein binding (96) or other interactions with the tissue. Additionally, internal chemical standards, which are typically pre-mixed with deuterium oxide (D_2O) to provide a lock signal, may be inhomogeneously distributed within the rotor (40).

The Electronic REference To access In-vivo Concentrations (ERETIC) method is a promising alternative to the use of chemical reference standards in HR-MAS spectroscopy of tissue and has several unique advantages. Because the ERETIC method employs a synthesized RF pulse during the acquisition period to produce its signal, no chemical substance needs to be added to the sample. Thus, there are no concerns about toxicity or chemical activity. The frequency, linewidth, and amplitude of the ERETIC signal may also be modified easily by the experimentalist and, the lineshape

is independent of B_0 homogeneity. Furthermore, there are no relaxation time considerations when using ERETIC because the linewidth can be chosen freely. Also, if the spectrometer is configured correctly, the RF coil loading caused by the sample reduces the ERETIC signal by the same amount as the metabolite signals from the sample, as expected for a quantitation reference (97). The ERETIC method has previously been shown to provide reproducible and robust concentration measurements in solution and solid state NMR (97, 98); however, very little has been reported on the use of ERETIC with HR-MAS spectroscopy of tissue. The aim of this study was to evaluate the accuracy, precision, and reproducibility of ERETIC compared to TSP in HR-MAS spectroscopy of solutions and prostate tissues in order to establish its reliability as a quantitative reference.

Materials and Methods

Hardware and ERETIC parameters

Spectral data were acquired at 11.7 T (500 MHz for ^{1}H), 1 °C, and a 2,250 Hz spin rate using a Varian INOVA spectrometer equipped with a 4 mm gHX nanoprobe. All samples were analyzed inside custom designed 20 µl or 35 µl leak proof zirconium rotors which can be purchased from Varian, Inc. (Palo Alto, CA).

Generation of the ERETIC signal required the development of a custom pulse sequence and modification of the system configuration as shown in Figure 3.1. The output of the ^{1}H synthesizer was shared between channels 1 and 3 within the system cabinet by connecting the synthesizer ports (SYNTH) for the waveform generators on these two channels to the same synthesizer output. This parallel configuration ensured that the ^{1}H transmitter and receiver were phase locked with the ERETIC transmitter. Channel 3 was set up to produce a programmable, low power output capable of generating an electronic signal with an amplitude comparable to the NMR signal

produced by the sample. The low power signal was created by bypassing the amplifier on channel 3 and transmitting the signal from output #4 on the attenuator module. The channel 3 output and the filtered output from channel 2 were combined with a directional coupler (Varian Inc, Palo Alto), allowing the signals from both channels to be transmitted through the X channel of the nanoprobe as shown in Figure 3.1 (78, 97).

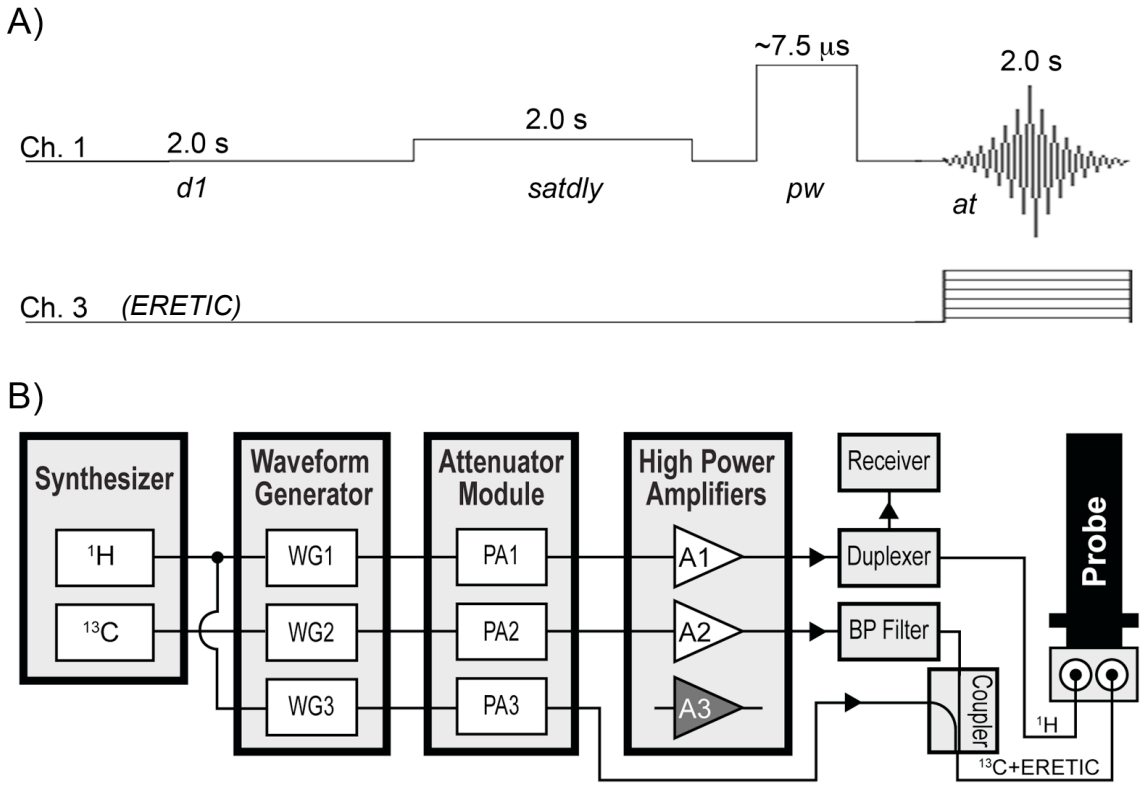

Figure 3.1 A) Pulse sequence diagram of the ERETIC sequence and **B)** system diagram of the Varian INOVA console highlighting the modifications required for generating an ERETIC signal at the ^{1}H frequency. The output of the ^{1}H synthesizer was shared between the waveform generators (WG) for channels 1 and 3. The ERETIC signal was taken directly from the output of the Programmable Attenuator (PA) module, combined with the output from channel 2 using a directional coupler, and transmitted through the X channel of the nanoprobe. The transmission of the ERETIC waveform and the data acquisition were synchronized in the pulse sequence. (d1: relaxation delay; satdly: presaturation delay; pw: pulse width; at: acquisition time; BP: bandpass)

The ERETIC signal was created using Pandora's Box (Pbox) software (Varian, Inc., Palo Alto) to generate an exponentially decaying waveform with a user-defined decay constant and offset frequency and synthesized using the waveform generator on

channel 3 as shown in Figure 3.1. The desired power and phase for the ERETIC signal were applied to channel 3, allowing independent control of the ERETIC signal's amplitude and phase relative to the rest of the spectrum. The ^{1}H RF pulses were transmitted on channel 1, the ERETIC signal was transmitted on channel 3 during the data acquisition and channel 2 was set and tuned to the ^{13}C frequency.

Because the ERETIC signal was transmitted through the RF coil tuned to the ^{13}C frequency, it was effectively transmitted through a detuned RF coil, and its transmission was unaffected by sample loading, as described by Ziarelli et al (97). In short, the quality factor (Q) of the X channel RF coil at the ERETIC frequency was insensitive to the sample loading differences because the X coil was tuned to the ^{13}C frequency, whereas the Q of the ^{1}H RF coil at the ERETIC (^{1}H) frequency was sensitive to sample loading differences. Thus, transmission of the ERETIC signal was constant for different loads. However, differences in sample loading or tuning of the ^{1}H RF coil attenuated the reception of the ERETIC signal by the same amount as the NMR signal originating from the sample. As a result, the ERETIC signal was equivalent to an NMR signal from a fixed amount of compound added to the sample. The ERETIC signal was phase cycled in synchronization with the receiver to maintain phase coherence across the scans.

Sample Preparation and Acquisition

Deuterium oxide (D_2O, 99.9% atom-D) and deuterium oxide containing 0.75 wt% 3-(trimethylsilyl)propionic-2-2-3-3-d_4 acid (D_2O+TSP) were purchased from a single batch manufactured by Sigma-Aldrich (St. Louis, MO). All solution samples were prepared by loading aliquots of D_2O+TSP (weighed to ±0.01 mg) into an HR-MAS rotor and filling the remainder of the rotor volume with D_2O containing no TSP. Samples containing 3.0 µL of D_2O+TSP were prepared and analyzed on five consecutive days over three separate weeks and monthly for five months to test the short term and long term stability of the

ERETIC and TSP peak areas. Calibrations were performed separately on 20 µL and 35 µL rotors spanning five TSP concentrations to determine rotor-specific conversion factors for ERETIC, which were later used to calculate metabolite amounts. Then, the precision and accuracy of measurements made using ERETIC were evaluated in a 35 µL rotor by acquiring five spectra on samples containing 1 µL, 15 µL, and 30 µL of D_2O+TSP. Spectra were also acquired at ERETIC transmitter power levels of -6, 0, 6, 12, and 18 dB to evaluate the linearity of the corresponding increase in ERETIC peak area.

One-dimensional spectra were acquired on all solution samples with a calibrated 90° pulse, 40,000 complex points, 20,000 Hz spectral window, 2 s delay (d1), 2 s water presaturation period (satdly), 2 s acquisition time (6 s repetition time, fully relaxed), 4 steady state pulses, and 64 transients as depicted in Figure 3.1. The phase and amplitude of the ERETIC peak were chosen to match other peaks in the spectrum, and the signal was transmitted during acquisition using 0 dB of power, a full width at half height of 3.5 Hz, and an offset frequency equivalent to -0.5 ppm.

This study was approved by the Institutional Review Board at our institution and informed consent was obtained from all patients. Tissue samples were obtained from patients undergoing transrectal ultrasound guided prostate biopsies (n=48) and radical prostatectomy surgeries (n=12), frozen on dry ice, and stored at -80 °C until the time of the HR-MAS experiment. The HR-MAS experiments were designed based on the methods described by Swanson et al. (40). In brief, to provide a lock signal and frequency reference, 3.0 µL of D_2O+TSP was pipetted into the bottom of a tared rotor and weighed to ±0.01 mg, after which a biopsy (mean = 5.90 ± 1.15 mg) or surgical (mean = 18.70 ± 3.44 mg) sample was weighed and added to a 20 µL (biopsy) or 35 µL (surgical) rotor. When necessary, the magnetic field homogeneity was optimized using

an automated routine. A presat sequence analogous to the one described for the solution samples was used for tissue samples, but with 128 transients to obtain a signal to noise sufficient for quantification. In addition, the TR was reduced to 4 s by setting the d1 = 0 s (Figure 3.1) because the metabolite T_1 relaxation times in tissue were shorter. As in previously published HR-MAS spectra of prostate tissue (40), a spin rate of 2.25 kHz was selected in order to minimize the overlap of the spinning sidebands with the metabolites of interest, while maintaining the pathologic integrity of the tissue. Moreover, as illustrated in Figure 3.5, with adequate water suppression, spinning sidebands due to residual water were usually not observed. Thus, the tissue HR-MAS experimental design minimized the impact of T_1 saturation and spinning sidebands on the results.

Data Analysis

Spectra were processed and analyzed using Advanced Chemistry Development's 1D NMR Processor, Version 9.15. (ACD/Labs, Toronto). Each FID was zero-filled to 262,144 complex points and Fourier transformed (FT). All tissue FIDs were multiplied by a 0.5 Hz exponential filter prior to the FT. The spectra were then phased manually, after which the baseline was corrected by fitting a 6th order polynomial curve to the spectrum and subtracting it from the spectrum. The TSP and ERETIC signals were quantified using peak areas, making the analysis less sensitive to sample-to-sample variations in B_0 homogeneity and T_2 that would affect the TSP lineshape. In the solution spectra, peak areas were measured by integrating a region spanning 100 Hz on each side of the peak's center, which was greater than 50 times the full width at half maximum of the peaks of interest (99). Whereas, peak areas in tissue spectra were measured using Lorentzian-Gaussian peak fitting as previously described (40) because the baseline near TSP was not flat enough to accurately measure its peak area with integration.

A conversion factor M_E equal to the number of protons equivalent to the ERETIC peak area was empirically derived in order to assess the quantification accuracy of ERETIC. M_E is related to the number of millimoles of TSP protons M_{TSP} as shown in Eq. [3.1]:

Eq. [3.1]
$$M_E = \frac{A_E}{A_{TSP}} * M_{TSP}$$

where A_{TSP} is the area of the TSP peak and A_E is the area of the ERETIC peak. In this study, M_E was determined separately for each rotor by plotting the ratio of (A_{TSP}/A_E) versus M_{TSP} calculated by weight for five concentrations of TSP and then performing a linear regression on the data. M_E was calculated by taking the inverse of the slope obtained from the linear regression. The plot used for the linear regression can be modeled by rewriting Eq. [3.1] as shown in Eq. [3.2]:

Eq. [3.2]
$$\frac{A_{TSP}}{A_E} = \frac{1}{M_E} * M_{TSP}$$

The precision and accuracy of the measured amount of TSP protons were assessed using a separate set of spectra recorded from solutions with varying TSP concentrations. The moles of TSP protons were calculated for these experiments using M_E, the measured peak areas from the spectra, and Eq. [3.3]:

Eq. [3.3]
$$M_{TSP} = \frac{A_{TSP}}{A_E} * M_E$$

The precision of the measured amount of TSP protons was evaluated by computing a relative standard deviation (RSD) for the measurements. The accuracy of the measured amount of TSP protons was then determined using Eq. [3.4]:

Eq. [3.4] $$\text{Accuracy} = \frac{\left(\overline{TSP_E} - TSP_W\right)}{TSP_W} * 100$$

where $\overline{TSP_E}$ is the average number of TSP protons measured using ERETIC, and TSP_W is number of TSP protons determined using the weight and concentration of D_2O+TSP.

The linearity of the increase in the ERETIC peak area with the increase in the ERETIC power as well as the slope of the increase was assessed by analyzing the data acquired with five different ERETIC power levels spanning -6 to 18 dB. In a spectrometer with ideal components, the area of the ERETIC peak (A_E) would be directly proportional to the voltage of the signal used to produce the ERETIC peak (V_L). In practice, the electronics used to generate the ERETIC signal are not perfectly linear causing the actual voltage range to be slightly different, usually smaller, than the expected voltage range. This reduction is often referred to as the compression factor (C) and can be modeled using the following relationship for A_E:

Eq. [3.5] $$A_E = R * C * V_L$$

In Eq. [3.5], R is the receiver conversion coefficient and it accounts for the amplification produced by the preamplifier as well as the attenuation caused by sensitivity of the RF coil. It is important to note that V_L is expressed on a linear scale and it is related to the voltage specified in the Varian software (V_{dB}) by:

Eq. [3.6] $$V_{dB} = 20 * \text{Log}\left(V_L\right)$$

Also, it should be noted that C is a function of V_L. In the treatment presented here, it will be modeled as two piecewise linear segments where C is 1 for $0 < V_L \leq 10^{-0.3}$

($V_{dB} \le -6$) and an unknown constant (C_1) for $10^{-0.3} < V_L \le 10^{0.9}$ ($-6 < V_{dB} \le 18$). After using Eq. [3.6] to replace V_L with V_{dB}, Eq. [3.5] becomes:

Eq. [3.7] $$A_E = R * C * 10^{\frac{V_{dB}}{20}}$$

Since C has been defined as 1 for V_{dB} = -6 ($V_L = 10^{-0.3}$), R can be determined from Eq. [3.7] using the A_E measured at V_{dB} = -6. This yields a value of 3.92e8 for R. Next Eq. [3.7] and the ERETIC power data were normalized by R to produce Eq. [3.8] and the data in Figure 3.2.

Eq. [3.8] $$\frac{A_E}{R} = C * 10^{\frac{V_{dB}}{20}}$$

The ERETIC peak area versus transmit power data shown in Figure 3.2 was fit to a linear model (y = ax + b) using the curve fitting toolbox in Matlab. The conversion of the power values from the dB scale to the linear scale was assumed to be perfect since it was computed by the spectrometer software and was applied to the data before fitting. If the ERETIC transmitter was a linear, one-to-one system, the slope of the fit (C_1) would be equal to one across the voltage range $-6 < V_{dB} \le 18$.

Finally, the variability of the TSP and ERETIC peak areas in the prostate tissue spectra were evaluated, as well as the error in the TSP peak areas. The variability in the TSP and ERETIC peak areas was evaluated by computing the RSD for spectra recorded from the biopsy and surgical samples, separately. The error of the TSP peak areas was calculated by comparing the measured amount of TSP protons determined using the spectra to the amount expected based on the mass of the TSP added to the rotor. The measured amount of TSP protons was calculated using the TSP and ERETIC peak areas, M_E, and Eq. [3.3]. These results were validated by comparing the TSP and

ERETIC signals in a representative prostate surgical spectrum to those in a solution spectrum acquired using the same HR-MAS protocol.

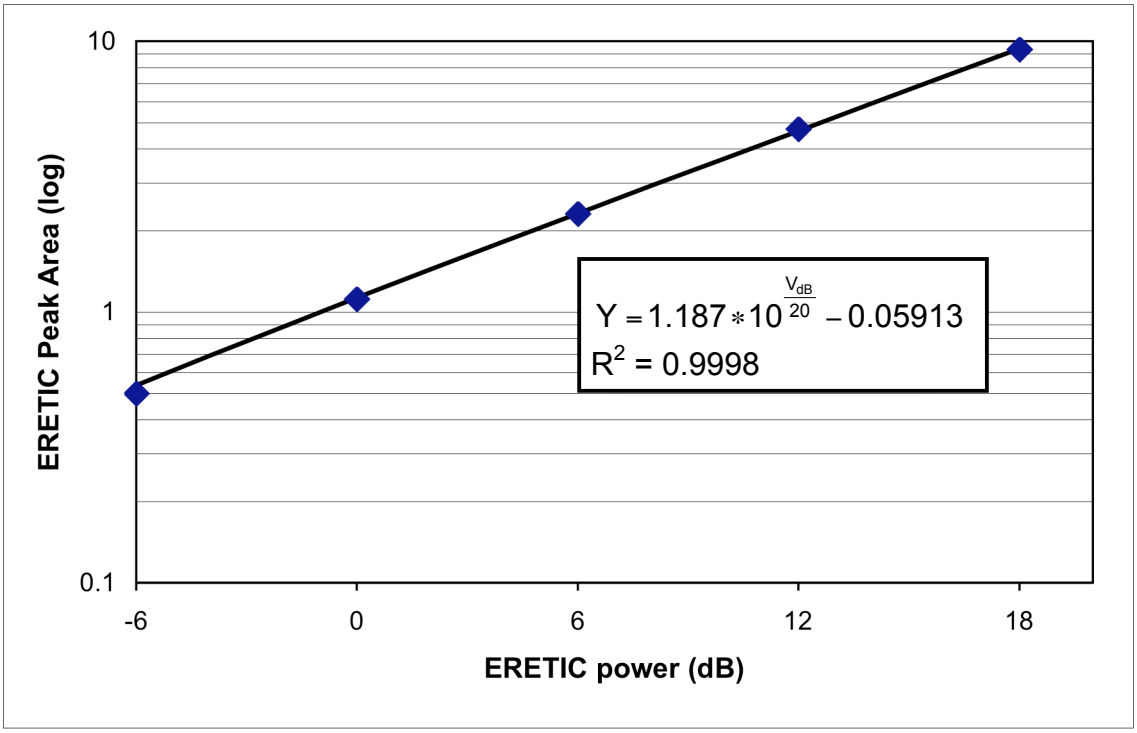

Figure 3.2 Linearity of ERETIC signal area with ERETIC power plot. The blue diamonds represent the average of three HR-MAS measurements taken on the same solution sample after they were normalized to remove arbitrary scaling factors introduced by the spectrometer's electronics. The black line is a plot of the fit obtained on the data from Matlab. The equation for the fit is written in the inset along with its R^2 value. Since the leading coefficient of the fitted model is 1.187, the model indicates that the ERETIC signal area does NOT exhibit the one-to-one correlation with the ERETIC power that would be expected from an ideal spectrometer.

Results

The weekly RSD of the ERETIC peak area in solution ranged from 2.09% to 4.25% over three weeks and was 4.10% over the five month period (Figure 3.3). The RSD of the TSP peak area corrected for mass was slightly higher than that of the ERETIC peak for the three weeks and slightly lower for the five months, but the difference was not significant in either case (combined $p<0.72$). ERETIC peak areas in individual spectra deviated from the long term peak area mean by a minimum of 0.98% and a maximum of

8.35%. The ERETIC peak area deviated by less than 5% of the mean peak area in 80% of the spectra.

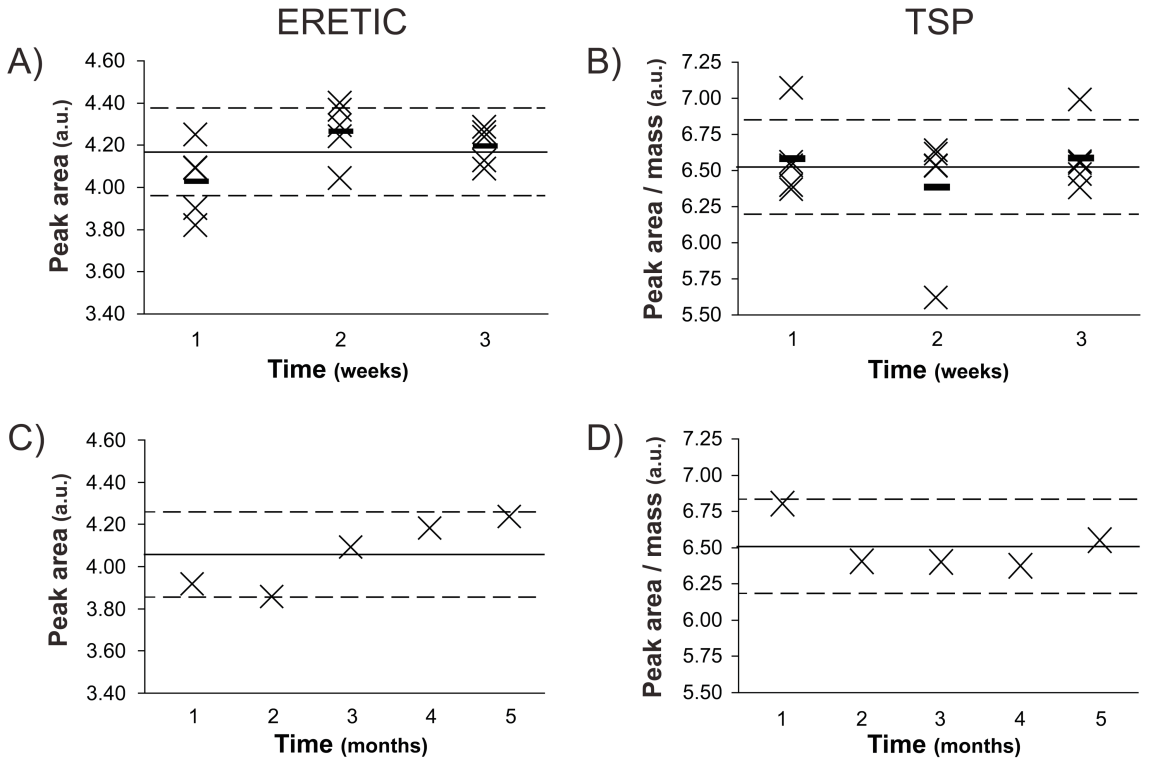

Figure 3.3 Relative standard deviation (RSD) of the ERETIC peak area and TSP peak area (corrected for mass) from identically prepared solution samples acquired **A** and **B)** on five consecutive days during three separate weeks and **C** and **D)** over five months. The solid line represents the mean peak area over the relevant time period, the dotted lines represent 5% deviations from the mean, and the small dashes in plots A and B represent the weekly means. Samples were prepared by adding 3 µL of D_2O+TSP (weighed to +/- 0.01 mg), and filling the remainder of the rotor volume with plain D_2O. The average weekly RSD of the ERETIC peak area was 4.25%, 3.29%, and 2.09% during each week respectively, while corrected TSP peak area RSD's were 4.30%, 6.76%, and 3.57% during the same periods. The average monthly RSD was 4.10% and 2.47% for ERETIC and TSP, respectively.

The ratio of TSP and ERETIC peak areas was plotted versus the number of µmols of equivalent protons for TSP (9 per molecule) determined by weight for each of the rotor sizes in Figure 3.4. A linear relationship was established with an R^2 of 0.999 for the 20 µL rotor and an R^2 of 0.998 for the 35 µL rotor using least squares regression. Next, M_E

was derived using Eq. [3.2]. At an ERETIC transmit power of 0 db, M_E equaled 0.393 µmol of protons in the 20 µL rotor and 0.269 µmols of protons in the 35 µL rotor.

Serial studies were then conducted to validate the accuracy and precision of these conversion factors. The number of µmoles of TSP protons was calculated using the mass of D_2O+TSP and compared to the number of protons calculated using ERETIC, as summarized in Table 3.1. For each amount of TSP, the ERETIC-derived number of protons was accurate to within 4.2% and precise to within 2.9% of the weighed measurement.

The ERETIC peak area increased linearly with the ERETIC transmitter power as the power was increased from -6 dB to 18 dB (Figure 3.2). However, the rate of the increase in the ERETIC peak areas was not one, as would be expected from an ideal spectrometer. The slope (C_1) of the Matlab fit to peak area data was 1.187 after the data was normalized to remove arbitrary scaling factors introduced by the spectrometer's electronics (R^2 = 0.9998). Since the slope was 18.7% greater than the theoretically expected value of 1, the increase in the ERETIC peak area is 18.7% greater than theoretically predicted for a 24 dB boost in power.

Figure 3.5 demonstrates the addition of the ERETIC signal to a representative prostate surgical tissue spectrum at a frequency of -0.5 ppm, where it does not overlap with other metabolite peaks. The peak had a Lorentzian lineshape, a full width at half height of 3.5 +/- 0.01 Hz, and a phase and amplitude comparable to the peaks originating from the tissue metabolites. In prostate biopsy and surgical tissues, the RSD of the ERETIC peak area was significantly lower than that of the TSP peak area corrected for TSP mass (4.53% compared to 20.1% in surgical tissue, $p < 0.001$; 3.33% compared to 31.7% in biopsy tissue, $p < 0.001$), while no significant difference was found between ERETIC and TSP peak area RSDs in solution (Table 3.2). A plot of

ERETIC peak area versus TSP peak area corrected for mass (plot not shown) showed no correlation (R^2 = .020), indicating that variation in TSP was not caused by differences in coil loading or coil tuning between samples.

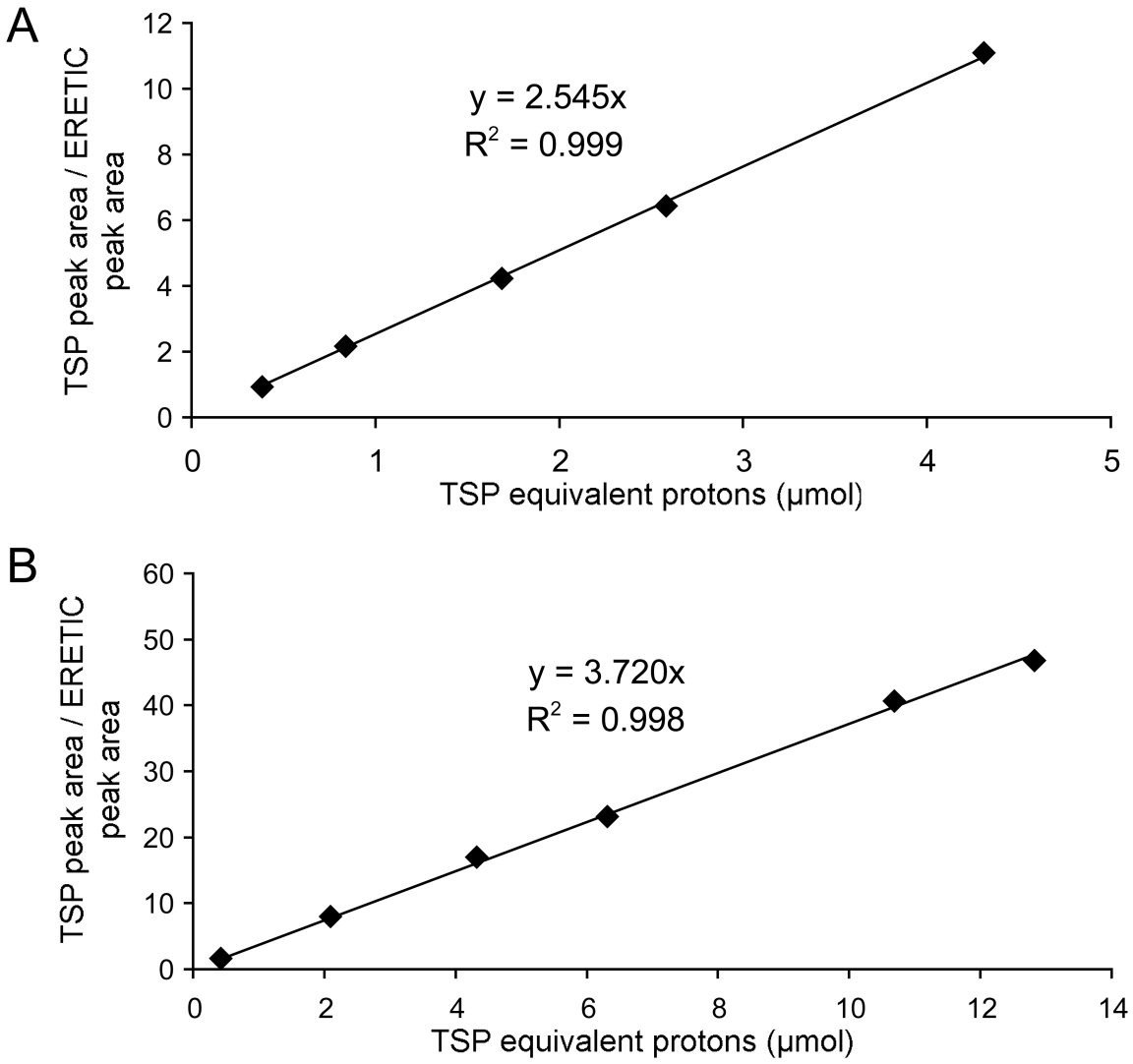

Figure 3.4 Plot of the TSP peak area (A_{TSP}) / ERETIC peak area (A_E) versus micromoles of TSP protons determined by weight in the **A)** 20 µL and **B)** 35 µL rotors. Linear regression was performed on the data to calculate the rotor-specific conversion factors (M_E), as contained in Eq. [3.2]. M_E represents the equivalent amount of protons for the ERETIC peak and can be used for quantification of metabolites. The M_E for the 20µL rotor was 30% greater than the M_E for the 35µL rotor.

TSP_W	TSP_E	Precision	Accuracy
0.408	0.425 ± 0.004	0.99%	4.16%
6.41	6.18 ± 0.18	2.91%	-3.60%
12.79	12.72 ± 0.30	2.36%	-0.49%

Table 3.1: Precision and accuracy of the number of TSP protons (μmol) measured using the ERETIC method from solution samples of equal volume. The left column shows the number of TSP protons calculated using the mass of TSP in the rotor (weighed to +/- 0.01 mg). The second column shows the mean and standard deviations of the same protons calculated using M_E and the ERETIC and TSP peak areas from five consecutive acquisitions. The third column shows the precision of the measurement expressed as the RSD. The fourth column shows the accuracy obtained using Eq. [3.4].

Additionally, the TSP peak areas in the tissue spectra were considerably smaller than what was expected based on the mass of the TSP added to the sample. For the prostate surgical spectra, the peak area was 73.4 ± 7.0% less than the expected area. The TSP peak area in the prostate biopsy spectra was 72.1 ± 14.4% less than the expected area. These large differences were verified by comparing the ERETIC and TSP peaks from a surgical spectrum to those from a solution spectrum acquired using the same HR-MAS protocol and a comparable amount of TSP. The ERETIC peak from the solution spectrum was 22.1% larger than the peak in the surgical spectrum due to lower RF coil loading caused by the solution sample, further substantiated by a 14.3% shorter 90° pulse width for the solution sample. After amplifying the surgical spectrum by 22.1% to correct for the loading difference, the ERETIC peaks were nearly identical, whereas the TSP peak was substantially smaller for the surgical spectrum (Figure 3.6). In order to match the linewidths of TSP peaks in the surgical and solution spectra, the TSP peak in the solution spectrum was apodized with a 2.9 Hz Lorentzian filter to facilitate the visual comparison present in Figure 3.6. The error in the TSP peak area for

the surgical spectrum in Figure 3.6 was 71.6% and its TSP peak area was 28.7% of the corresponding peak in the solution spectrum.

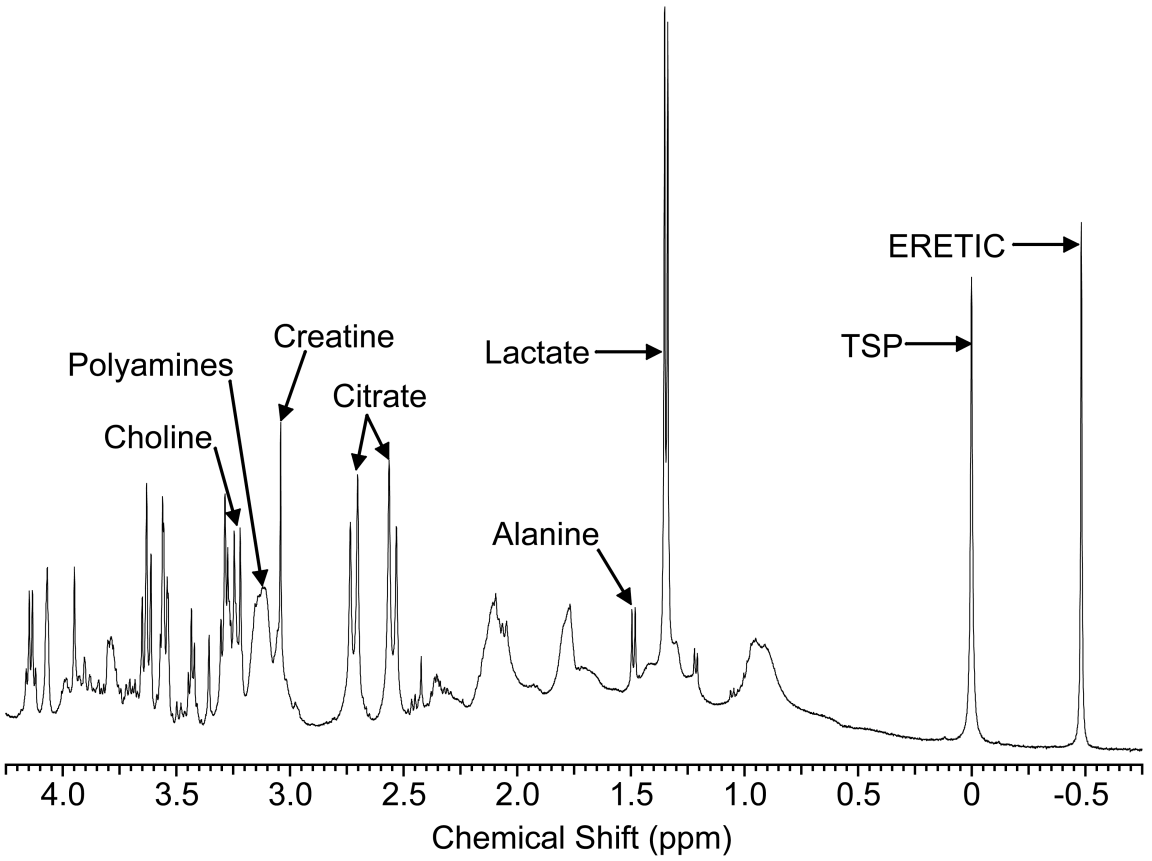

Figure 3.5 Representative HR-MAS spectrum of prostate surgical tissue with the ERETIC signal generated at a frequency of -0.5 ppm and with a transmitter power of 0 dB. The phase of the ERETIC signal was matched to the metabolites before the acquisition and produced a peak that had a phase and amplitude comparable to those of the tissue metabolites. The frequency of the ERETIC signal was well separated from the other peaks in the spectrum and allowed for accurate quantification of its peak.

Sample	TSP	ERETIC	p value
TSP Solution (n=19)	2.72%	3.69%	0.32
Prostate Surgical (n=12)	20.1%	4.53%	< 0.001
Prostate Biopsy (n=48)	31.8%	3.34%	< 0.001

Table 3.2: Relative standard deviations (RSD) of the TSP peak area (corrected for mass) and ERETIC peak area in solution and prostate biopsy and surgical tissues.

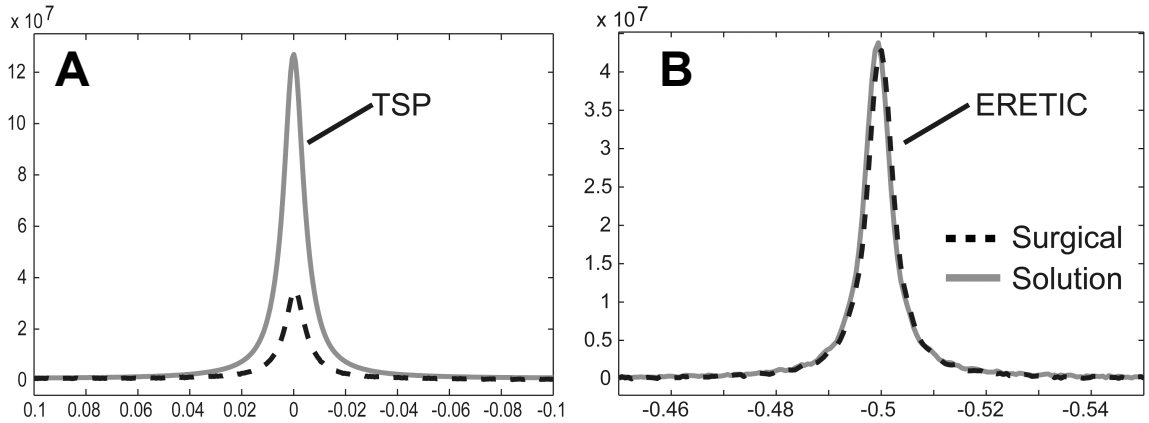

Figure 3.6 Comparison of the **A)** TSP and **B)** ERETIC peaks from a prostate surgical sample and solution sample with a comparable amount of TSP. The surgical sample was amplified by 22.1% to correct for loading differences between the two spectra, determined by the differences in the ERETIC peak area and the 90° pulse width. The TSP peak from the solution spectrum was apodized by 2.9Hz to match the linewidths of the TSP peaks in the two spectra. Since the TSP peak area in the tissue spectrum was 28.7% of the peak area in the solution spectrum, a significant amount of the TSP was not detected in the HR-MAS experiment.

Discussion

In this study, the ERETIC method was used to generate a stable and robust electronic quantitative reference signal for HR-MAS NMR spectroscopy applications. The ERETIC signal was then added reproducibly to prostate tissue data acquisitions at a consistent frequency and in phase with other metabolites. Modifications for the addition of ERETIC were minimal and used only standard components found on many modern

spectrometers and a commercially available directional coupler. Even though ERETIC has been used successfully in solution and solid state NMR applications (97, 98), little work has been done showing its feasibility as a quantitative reference standard for HR-MAS spectroscopy of tissue.

The ERETIC peak area was found to be stable in solution over the short term (weekly intervals) and long term (5 months), with a RSD of 3.69% over all experiments. This level of stability was comparable to that observed with TSP using the same acquisition parameters. However, the stability of ERETIC signal was slightly lower than previously reported (78). The lower stability was not surprising because the amplitude of the ERETIC signal was chosen to be relatively low to mimic the intensity of the metabolite signals observed in tissue. The lower amplitude produced a signal-to-noise (SNR) that was more than sufficient for these studies, but lower than what was used in the previous reports. The lower SNR resulted in a higher RSD, as has been published (100). In addition, small differences in the baseline correction applied during post-processing and variations in the probe tuning from sample to sample would also impact the ERETIC peak area stability. Lastly, a small coupling between the ERETIC transmitter and the digital receiver inside the system cabinet was observed on the INOVA spectrometer that contributed to the lower ERETIC peak area stability. Despite all of the small sources of error in the measured ERETIC signal, the variability of the ERETIC signal was much less than the biological variability that exists between samples (35).

Due to differences in volume and sensitivity, the conversion factor (M_E) differed by more than 30% between the 20 µL and 35 µL rotors for ERETIC signals transmitted with the same power. Therefore, the ERETIC response must be calibrated for each rotor. This difference may be explained partly by signal dampening due to increased thickness

of the zirconium walls in the 20 μL rotor. Specifically, the TSP peak area for a comparable amount of TSP was significantly lower when recorded using the 20μL rotors. This decrease in the TSP peak area caused an increase in M_E as expected from Eq. [3.1]. Since the signal from the TSP molecules must propagate through the walls of the zirconium rotors, the decrease in the TSP signal from the 20μL rotors suggests that the thicker walls of the 20μL rotors produced more attenuation of the TSP signal. There was, however, no need to recalibrate M_E during the five-month time frame of the experiments presented here because of the relative long term stability of the ERETIC signal. Relative standard deviations of less than 3.0% and errors of less than 4.2% were found using M_E and the ERETIC peak for quantification of TSP in solution compared to values expected by weight. The fact that these precision and accuracy percentages are higher than the 0.5 – 3% range typically reported in ^{1}H NMR (95) and the 0.25 – 1.3% previously reported for the ERETIC added to solution spectra (78) can be explained by the small errors described above, with the exception of the probe tuning variations. If necessary, the accuracy of quantifications based on ERETIC could be improved by increasing the signal to noise ratio, but this would not affect the metabolite SNR.

The increase in the ERETIC peak area as a function of the ERETIC transmitter power was linear, but the rate of increase was 18.7% higher than the rate of increase expected for an ideal spectrometer. The increase may have been a result of imperfections in the electronics or it may have been designed to compensate for a loss in gain introduced by the amplifier over this voltage range. Since the amplifier was by-passed for the transmission of the ERETIC signal, the effects caused by the amplifier are excluded from these measurements. For the experiments included in this study, an ERETIC power of 0 dB produced a peak with an amplitude comparable to the metabolite peaks from the tissue samples. However, the optimal power depends on the sample

size and the metabolite concentration in the tissue and would likely vary across different spectrometers and probes. While the power can be changed easily, the deviation of the slope of the ERETIC peak area versus power from unity indicates that the ERETIC conversion factor needs to be calibrated at the desired power.

The reproducibility of the ERETIC peak area was comparable in tissue and solution (RSD = 4.07% versus 3.94%, respectively), while the reproducibility of TSP corrected for mass was much poorer in tissue than in solution (RSD = 20.1% and 33.7% in prostate surgical and biopsy, respectively, versus 4.90% in solution). Furthermore, a significant amount of the TSP added to the tissue samples was not observed in the spectra, as indicated by the large error in the amount of TSP measured from the tissue spectra. The presence of this error was confirmed and illustrated in Figure 3.6 by comparing the TSP and ERETIC peaks from a prostate surgical sample and a solution sample acquired using the same HR-MAS procedure and the same amount of TSP. While the increased coil loading created by the tissue sample would decrease the signal from the TSP, the observed decrease in the TSP peak area was much greater than the decrease in the ERETIC peak area and increase in the 90° pulse duration, which should be equivalently affected by the loading changes. The observed error in the TSP peak area would lead to an over-estimation of metabolite concentrations if used as a quantification reference as previously noted (40). Effects such as T_1 saturation and overlap with spinning sidebands could have contributed to the errors observed in the tissue samples. However, the T_1 of TSP when added to HR-MAS tissue experiments at 1°C is ~600 ms (40) leading to a signal loss of 0.13% with a 4 s repetition time. At a spin rate of 2.25kHz, the ERETIC and TSP peaks would overlap with spinning sidebands from molecules resonating at 4.0 and 4.5ppm, respectively. The spectral intensities at these frequencies are small (Figure 3.5), rendering their spinning sidebands almost

undetectable at 0 and -0.5ppm (data not shown). As illustrated in Figure 3.5, with adequate water suppression, spinning sidebands due to residual water were usually not observed. Thus, the tissue HR-MAS experimental design minimized the impact of T_1 saturation and spinning sidebands on the results.

The large measurement error and variation in the TSP peak area may also be attributed to an inhomogeneous distribution of TSP within the rotor, B_0 inhomogeneity, and weighing errors, all of which are avoided with ERETIC. Additionally, the variability and error in the TSP signal observed in both tissue types is consistent with a previous study, which found that when comparable amounts of TSP were added to blood serum samples, the TSP had a very short T_2 due to possible protein binding (96). Regardless of the cause of the TSP errors, the superior reproducibility of ERETIC would reduce the measurement error of metabolite concentrations in tissue, thereby providing values that are more reflective of true biological differences between tissues of different disease states.

While ERETIC shows great promise as a quantitation reference for HR-MAS spectroscopy of tissue, the method has a few limitations. First, the ERETIC phase must be matched to that of the metabolite signals on a per sample basis prior to the data acquisition or else the resulting signal may be out of phase from the metabolite signals. However, within the same day these phase adjustments were often small or negligible when the same rotor was used. In addition, this limitation can be overcome by using a spectral quantification tool that has the ability to quantify peaks with different phases. Second, the ERETIC frequency was offset by a constant amount from the center frequency, chosen to be water. Because of small frequency shifts in the water peak caused by minor temperature fluctuations and variations in determining the center

frequency for the relatively broad water peak, the ERETIC frequency will vary slightly from sample to sample.

In this study, the ERETIC method provided an electronic reference that was stable, accurate, and precise compared to TSP under HR-MAS conditions. In prostate tissue, the ERETIC peak was also shown to have a reproducible area and a shape that was independent of B_0 homogeneity. The ERETIC signal's frequency, linewidth, and amplitude can be optimized for each application; however, the signal must be calibrated at the desired amplitude or power as the system does not behave as an ideal one-to-one system. In addition, the amplitude of the recorded ERETIC signal is sensitive to the rotor volume and must be calibrated for each rotor, even those of the same volume. Once the ERETIC signal was properly calibrated, its variability and accuracy as a quantification reference in HR-MAS spectra from prostate tissue was superior to that of TSP. The enhanced quantification accuracy and precision provided by ERETIC will improve the quantification of absolute metabolite concentrations in individual tissue samples and facilitate comparisons between tissue populations representing various biological conditions and diseases. Beyond quantifying spectra from prostate surgical and biopsy samples, the benefits afforded by ERETIC will be useful for quantifying HR-MAS spectra from other organs, such as brain, breast, liver, or kidney, and other sample sources, such as cell cultures, tissue cultures, or biological fluids.

3.2 Quantification References for ^{13}C HSQC Experiments

As indicated in Chapter 2, the ^{13}C labeling of the reporter metabolites of interest will be measured using an HSQC experiment. In order to interpret and quantify the ^{13}C HSQC spectra, a reference molecule must be present in the spectra. The reference molecule must provide a chemical shift reference to facilitate identification of the molecules producing the HSQC cross-peaks as well as a concentration reference to

permit measurement of concentrations associated with the HSQC cross-peaks. In addition, it will be necessary to calibrate the pulse widths for the carbon pulses in the HSQC experiments. Without calibrated carbon pulses, the HSQC cross-peak volumes will not accurately reflect the concentrations of the molecules they represent. Therefore, the HSQC reference should also support the calibration of the carbon pulses on an individual sample because the metabolite concentrations in the sample will be too low to permit pulse width calibrations. Thus the HSQC reference molecule must serve as a quantification reference, a chemical shift reference, and a calibration reference. For simplicity, the reference molecule will be referred to as a quantification reference from this point forward.

Based on the uses for the quantification reference, it will not be possible to use one of the molecules in the HR-MAS sample as an internal quantification reference for the HSQC because they are of an unknown concentration and their SNR will be too low for pulse width calibrations. As a result, an external reference must be added to the HSQC spectrum. In section 3.1, several important characteristics of an external reference were highlighted. Namely, the reference should be highly reproducible from sample to sample, non-toxic to the tissue or cells in the sample, chemically inert (metabolically inactive), non-volatile, nonhygroscopic, resonate at a frequency that does not overlap with other peaks, possess a sufficiently long T_2 to allow good signal detection, and possess a short enough T_1 to prevent signal saturation when using a repetition time (TR) appropriate for the tissue. In addition to these requirements, the HSQC quantification reference must produce a cross-peak in the HSQC spectrum. Since a ^{13}C HSQC only detects ^{1}H's bound to ^{13}C nuclei, the quantification reference needs to contain a ^{13}C nucleus with a directly attached ^{1}H nucleus. Ideally, the ^{13}C nucleus will resonate between 0 and 100 ppm in the carbon spectrum and have multiple chemically equivalent

^{1}H's attached to it that are not split by other ^{1}H's. The extra ^{1}H's will increase the SNR of the reference's cross-peak. Furthermore, the low natural abundance of ^{13}C will require that the reference compound be synthetically enriched with ^{13}C to further improve the SNR of its HSQC cross-peak. Therefore, the compound must be commercially available in a ^{13}C enriched form at a reasonable price. Clearly, the long list of requirements for the quantification reference limits the number of compounds that could used as a reference.

One easy way to satisfy these requirements would be to use an electronic reference as was done for the 1D ^{1}H experiments. The ERETIC method provides a very accurate quantification reference for HR-MAS spectroscopy and is fairly easy to implement on modern multi-channel spectrometers for one-dimensional experiments as shown in the previous section. Unfortunately, even though it has been demonstrated that ERETIC can also be applied to two dimensional experiments (101), the limited memory available in the hardware of many multi-channel spectrometers makes it significantly more difficult to use ERETIC as a quantification reference for two-dimensional experiments. Since an electronic reference is not a practical option for the HSQC quantification reference, a suitable reference chemical must be identified.

Historically, several quantification references have been used for ^{13}C metabolic studies. Lactate and myo-inositol have both been used as references for natural abundance ^{13}C studies (102, 103). However, neither would be appropriate as an external reference for HR-MAS studies on prostate tissue because they are already present in prostate tissue. Dioxanne was used as a reference for extract studies (104, 105). While it is highly soluble in water, it is a known animal carcinogen and a "reasonably anticipated" human carcinogen. Therefore, it was excluded from consideration because it posed a possible health hazard to the experimentalist and, it would likely be harmful to the tissue sample as well. Ethylene glycol also was ruled out

because it costs $668 per gram, even though it was previously used for ^{13}C NMR studies on cells (106). Fortunately, two other compounds seemed to be more promising options for a quantification reference. Both ^{13}C labeled glycine and formic acid are commercially available and are more reasonably priced at approximately $220 per gram. While formic acid has been used as an external reference, there are some concerns that it may be toxic to human tissue and its carbon chemical shift is 166 ppm. Since its carbon chemical shift was greater than 100 ppm and its toxicity would have to be investigated, formic acid was eliminated from consideration. On a more positive note, the ^{13}C chemical shift of C-2 glycine is 42.56 ppm and it is not toxic to human tissue as it is a naturally occurring amino acid. Even though it is naturally occurring, its concentration is virtually undetectable in prostate tissue and it is metabolically inactive. As an added benefit, glycine has 2 chemically equivalent ^{1}H's that are not split. It does slightly overlap with C-1 and C-3 myo-inositol. However, it was used in such high concentration for the HR-MAS experiments that the overlap did not affect the quantification of the glycine reference. Therefore, synthetically enriched ^{13}C-2 glycine was used as the HSQC quantification reference for the HR-MAS experiments included in this project.

3.3 Decoupling Optimization

While ^{13}C labeling of metabolites of interest and their products provides a powerful tool for studying product formation and the pathways linking the products to their precursors, it increases the complexity of the HR-MAS spectra. The primary difference in the spectra is caused by the J-coupling that exists between the ^{13}C nuclei and the neighboring nuclei, in many cases the attached ^{1}H nuclei. The proton-carbon J- coupling (J_{CH}) affects both the ^{1}H and ^{13}C spectra of these metabolites by splitting the spectral peaks of the coupled nuclei into additional peaks. The extra information provided by the J_{CH} splitting in a one-dimensional spectrum can be used to separate the ^{13}C labeled pool of the metabolite from the ^{12}C labeled pool. In addition, the spins of the ^{13}C labeled

metabolite pool can be manipulated using the J_{CH} coupling so that only the signal from the ^{13}C pool is recorded, as is done with the HSQC sequence. These benefits come with some disadvantages as well. Since the ^{1}H spectra of prostate tissue is already rather densely populated, the additional peaks produced by the J_{CH} splitting lead to even more complex and crowded spectra and often increase the number of metabolites with overlapping peaks. In the case of Lactate, Alanine, and Glutamate at 11.7T, most of the new peaks overlap with other metabolite peaks making it difficult to quantify these peaks. In addition, the J_{CH} splitting divides the signal from the chemically equivalent nuclei into separate, smaller peaks resulting in a lower signal-to-noise for the individual peaks. Fortunately, the complications caused by the J_{CH} coupling can be eliminated by decoupling the ^{13}C nuclei from the ^{1}H nuclei while the spectrum is being recorded.

Over the years, several schemes have been developed for decoupling neighboring nuclei from one another. Naturally, each scheme has advantages and disadvantages relative to the other schemes. In order to select the scheme appropriate for the proposed studies, it is necessary to define the requirements for the decoupling. The HR-MAS protocol described in Chapter 2 relies on carbon decoupled proton ($^{1}H[^{13}C]$) spectra to measure the total metabolite concentration and HSQC spectra to measure the ^{13}C labeled metabolite concentration. Both of these experiments will be used to record the ^{1}H signal from compounds that have been labeled with ^{13}C. Therefore, both experiments require ^{13}C decoupling. Even though the ^{13}C NMR spectrum spans a huge range from 0 – 220ppm, only the ^{13}C nuclei attached to ^{1}H nuclei need to be decoupled, reducing the decoupling range to 0 – 100ppm. At 11.7T, this decoupling range corresponds to a decoupling bandwidth of 12.5kHz. In addition, it is important to limit the amount of power used for the decoupling to avoid heating the sample during the HR-MAS experiment. As was described in Chapter 2, in order to minimize the metabolic

activity during the HR-MAS experiment, it is necessary to keep the sample cold for the entire experiment. The last requirement for the decoupling is that the noise produced by the decoupling, mainly decoupling sidebands, be minimal. If the decoupling noise becomes too large, two problems arise. First, the spectral noise spikes created by one metabolite may overlap with the peaks of another metabolite leading to an inaccurate area or volume measurement for the second metabolite. Second, the spectral noise includes a portion of signal produced by the metabolite. If a significant percentage of a metabolite's signal is lost to decoupling noise, the area or volume measurements for that metabolite will lead to inaccurate estimations of the metabolite's concentration. Thus, there are three requirements for the ^{13}C decoupling necessary for these studies: 1) a bandwidth greater than 12.5kHz, 2) low enough power to avoid sample heating, and 3) minimal decoupling noise or decoupling sidebands.

After surveying the various decoupling schemes, continuous wave (CW) and WALTZ decoupling could be ruled out because they do not satisfy the first requirement. CW decoupling is effective for decoupling a narrow frequency range because it does not require large amounts of power and provides good quality decoupling across the frequency range. Unfortunately, the decoupling bandwidth is far too narrow for the HR-MAS studies proposed here. WALTZ decoupling works very well for ^{1}H decoupling where the bandwidths are approximately 2.5kHz at 11.7T. However, WALTZ does not work well for ^{13}C decoupling because the bandwidth required is much larger than for ^{1}H. Fortunately, there are two other decoupling schemes that work very well for ^{13}C decoupling, namely GARP decoupling and adiabatic decoupling. In an attempt to evaluate these two decoupling schemes against the three requirements presented in the previous paragraph, several experiments were conducted on a concentrated solution of ^{13}C-2 glycine with a small amount of TSP added as a reference. The decoupling

bandwidth was measured by varying the decoupling offset frequency (DOF) from -18.5kHz to 6kHz in increments of 500Hz. As a side note, the DOF controls the center frequency of the decoupling channel. By varying the DOF, the decoupling window or absolute frequency range that was successfully decoupled was also adjusted. Since the spins from the glycine molecules resonant at a fixed frequency for a given magnetic field strength (125.6540 MHz at 11.7T, DOF of -6.3kHz), the decoupling bandwidth, the width of the decoupling window, was measured by shifting the decoupling window across the resonant frequency of the ^{13}C-2 glycine. The decoupling bandwidth was calculated by taking the difference between the largest and smallest DOF that produced a fully decoupled peak for ^{13}C-2 glycine. The heating of the sample for the two decoupling schemes was monitored by measuring the chemical shift of the TSP in the ^{13}C-2 glycine solution relative to the lock while the sample was decoupled 36 times using a 2 second data acquisition time, a 6 second TR, and 90° excitation pulse. Since the resonant frequency of the TSP is temperature dependent, the chemical shift will change as the sample temperature changes. The amount of decoupling noise was quantified by measuring the peak height of the decoupling sidebands relative to the decoupled peak height for ^{13}C-2 glycine.

Before the decoupling scheme comparison experiments could be performed, the 90° pulse width had to be measured for the ^{13}C channel. Since the ^{13}C RF coil is the outer coil in the Varian Nanoprobe, the sensitivity of the coil is much poorer than the inner ^{1}H coil. As a result, the ^{13}C pulse was calibrated using the indirect method depicted in Figure 3.7. The sequence, named PWXCAL on the Varian console, uses a spin echo pulse combination on the ^{1}H channel with an echo time of $1/J_{CH}$ and ^{13}C excitation pulse synchronized with the ^{1}H 180° pulse. Since the coupling constants for ^{13}C-2 glycine was 143Hz, the inter-pulse delay was 3.50msec ($1/2J_{CH}$). When the flip

angle of the ^{13}C pulse is 90°, the two peaks from $^{1`3}C$-2 glycine will be nulled. Therefore, the sequence was used to calibrate the ^{13}C pulse width by varying the width of the ^{13}C pulse in the PWXCAL sequence and determining which value produced a null in the ^{13}C-2 glycine peaks.

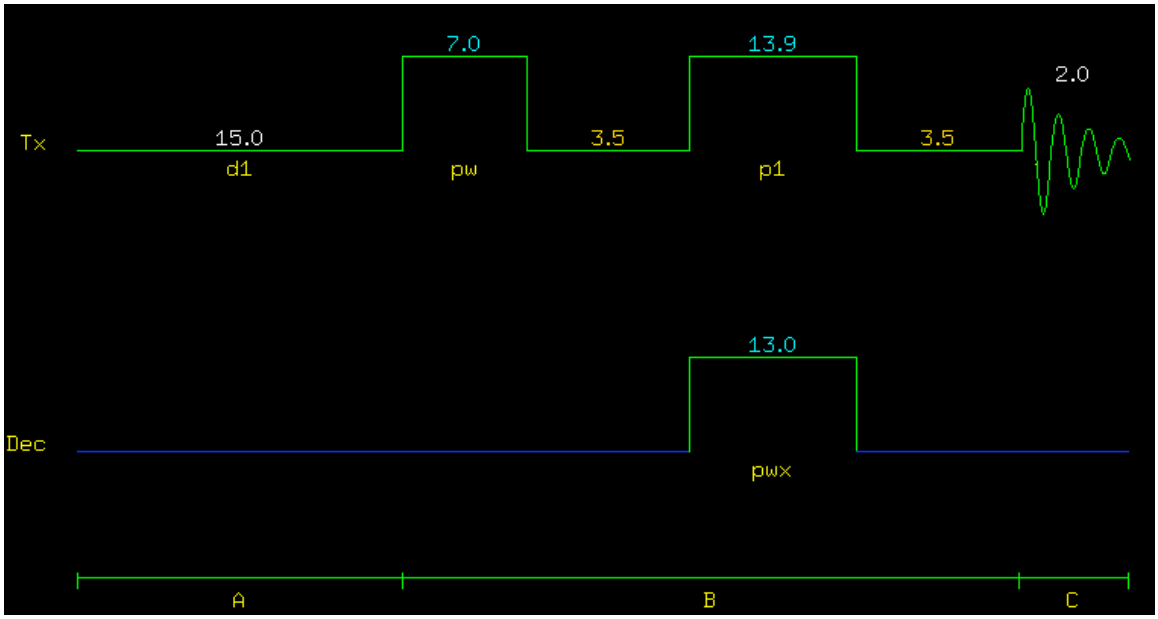

Figure 3.7 A diagram of the PWXCAL pulse sequence used to perform an indirect calibration of the ^{13}C 90° pulse width. The numbers in white are in seconds, the numbers in yellow are in milliseconds, and the numbers in light blue are in microseconds. The ^{1}H channel is displayed at the top of the diagram, labeled as Tx, and the ^{13}C channel is displayed at the bottom of the diagram, labeled as Dec.

Equipped with a calibrated ^{13}C pulse, the GARP decoupling scheme was implemented using Varian's standard GARP waveform by setting the dmm parameter to ccg and using the attval macro to calculate the pulse-width that would produce a 90° pulse on the ^{13}C channel at the desired power level. The GARP scheme was characterized using three different power levels, 41, 42, and 43dB. The adiabatic schemes utilized a WURST-40 adiabatic pulse (107) and were generated using a customized version of Varian's makeCshp macro. The makeCshp macro employed Pbox to create a Varian shape file for the adiabatic decoupling sequence that theoretically exhibited the desired decoupling bandwidth and pulse length and was

based on the specified adiabatic pulse and calibrated ^{13}C pulse width. For most of the adiabatic pulses, a 15kHz bandwidth was requested to ensure that they provided complete decoupling of the carbon nuclei spanning a 12.5kHz range. The pulse length for the individual pulses was varied from the default of 1,400μsec to 444μsec, a duration equivalent to one rotation of the HR-MAS rotor, as well as 222μsec. The spectrometer was configured to use the adiabatic decoupling sequence by setting dmm to ccp and dseq to the name of the shape file created by the makeCshp macro. The dres, dmf, and the power parameters were set based on the information provided by Pbox in the shape file. The DOF was arrayed as described above for both the GARP and the adiabatic decoupling schemes.

The data in Figure 3.8 show the decoupling profile and bandwidth achieved on ^{13}C-2 glycine with various permutations of the GARP and adiabatic schemes. The variation in the peak height of the decoupled glycine peak revealed that the there was some variation in the decoupling across the decoupling window for all the decoupling sequences. The decoupling bandwidth of the GARP sequences and the adiabatic sequence with 1,400μsec pulses satisfied the 12.5kHz decoupling bandwidth requirement. However, the adiabatic sequences with 222 and 444μsec pulses did not provide a 12.5kHz decoupling bandwidth unless the bandwidth used to design the pulse was increased above 15kHz as can be seen by the data in Table 3.3 and Figure 3.8. As expected, the frequency shift of the TSP peak increased with the decoupling power and the overall duty cycle of the decoupling, indicating that the amount of sample heating was directly proportional to the decoupling power and duty cycle. When using decoupling powers of 47 dB or more the TSP peak shifted by at least 10 Hz. After decreasing the power to 41 dB, the TSP peak only shifted by a couple Hertz. The decoupling sidebands were largest for the adiabatic decoupling sequence that used

1,400μsec long pulses. Although, the amplitude of the decoupling sidebands decreased as the pulse length was shortened to the point that the sidebands were almost nonexistent with 222μsec long pulses (Figure 3.9). The GARP decoupling sequences in general had lower decoupling sidebands as compared to the adiabatic sequences. Furthermore, the decoupling sidebands decrease for the GARP sequences as the decoupling power was increased from 41dB to 43dB. Out of the decoupling options that provided sufficient decoupling bandwidth, the GARP decoupling sequence with a pulse power of 43dB provided best combination of low power deposition and minimal decoupling noise. Thus, the GARP sequence with 43dB pulse power was used to decouple the ^{13}C nuclei from the ^{1}H nuclei for all the HR-MAS studies presented in Chapter 4. In an attempt to further reduce the power deposition and corresponding sample heating, the decoupling duty cycle was slightly reduced for these experiments by decreasing the data acquisition time to 1.5 s and increasing the TR to 7 s.

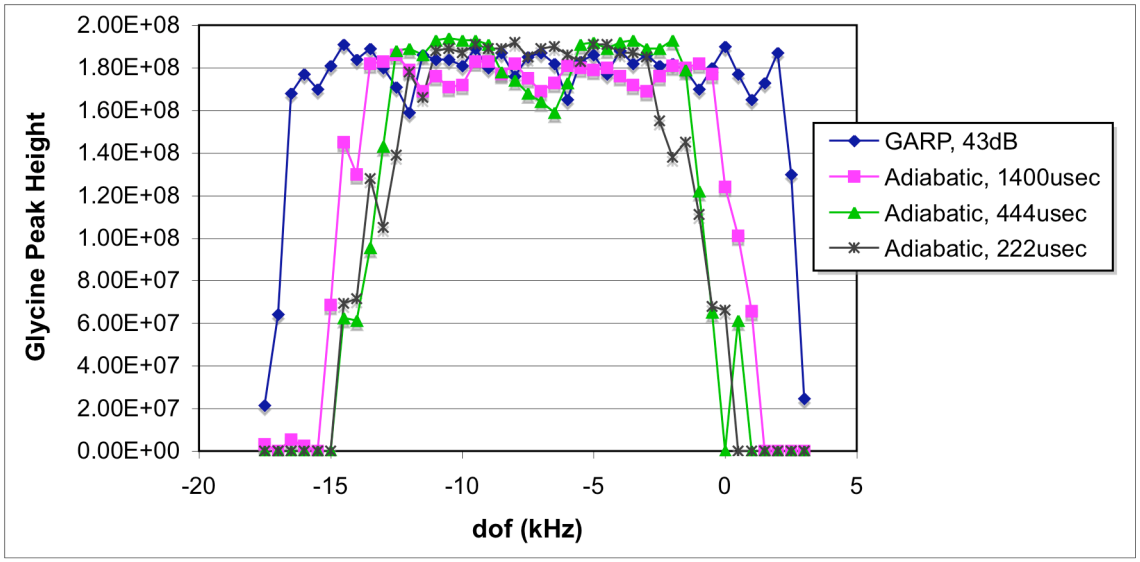

(A)

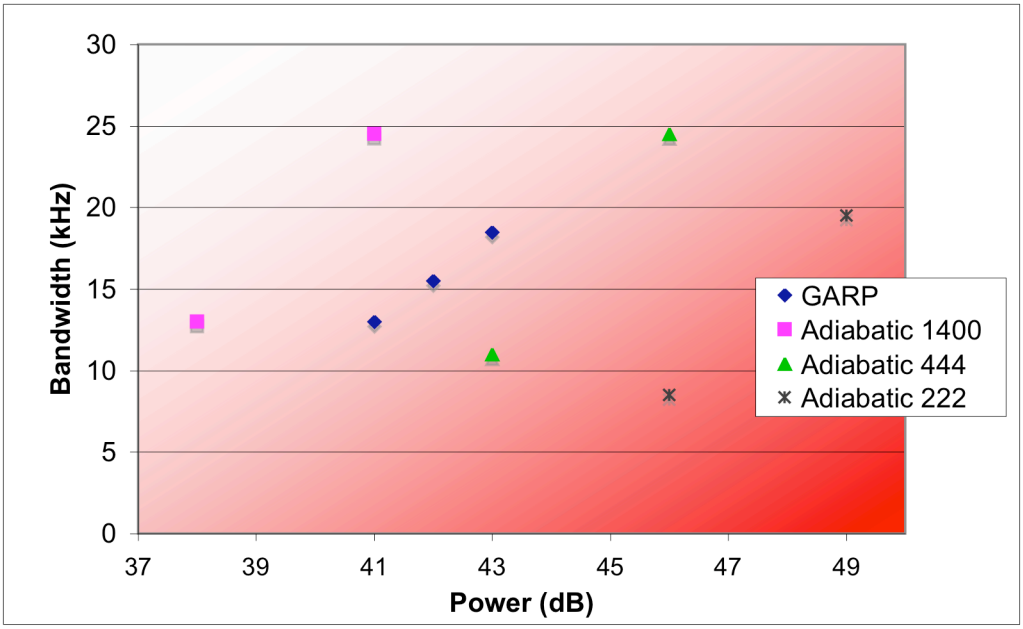

(B)

Figure 3.8 **(A)** Carbon decoupling profile plot and **(B)** decoupling bandwidth vs. decoupling power plot for several permutations of GARP and adiabatic decoupling. All the data are taking from $^{1}H[^{13}C]$ spectra collected from a solution sample of ^{13}C-2 glycine. The top panel depicts how well the glycine was decoupled as function of the decoupler offset frequency. The small depressions in the flattops of the profiles indicate that the decoupling performance was slightly degraded at certain frequencies. The bottom panel illustrates the tradeoff between the decoupling bandwidth and the decoupling power. The best combination, large bandwidth and low power, is shaded white on the plot and the worst combination is shaded red. The adiabatic scheme with 1,400μsec pulses exhibited the largest decoupling bandwidth with the least amount of decoupling power.

Decoupling Scheme	Pulse Width *(µsec)*	Design Bandwidth *(kHz)*	Power	Measured Bandwidth *(kHz)*
GARP			41	13
GARP			42	15.5
GARP			43	18.5
Adiabatic	1400	15	38	13
Adiabatic	444	15	43	11
Adiabatic	222	15	46	8.5
Adiabatic	1400	25	41	24.5
Adiabatic	444	25	46	24.5
Adiabatic	222	25	49	19.5

Table 3.3 The measured decoupling bandwidth for various permutation of the GARP and adiabatic decoupling schemes.

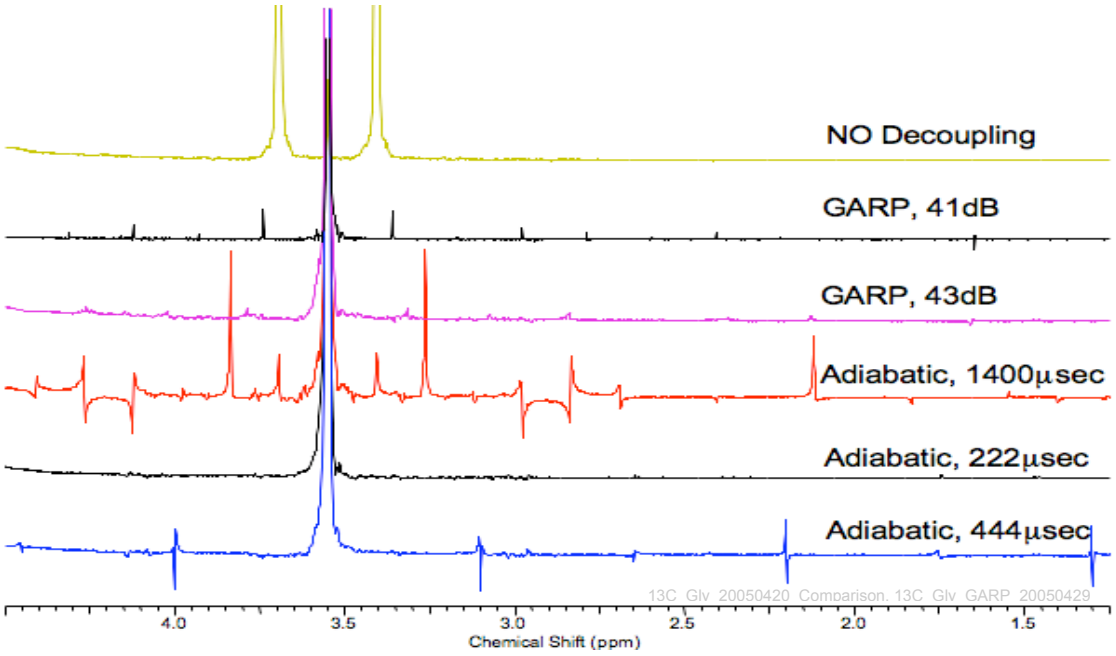

Figure 3.9 Decoupling sidebands for various decoupling schemes. The $^{1}H[^{13}C]$ spectra were obtained from a solution of ^{13}C-2 glycine.

Chapter 4
Investigating Metabolic Changes in New Human Prostate Cancer Model Systems with ^{13}C Labeling

4.1 Requirements for a Model System of Prostate Metabolism

Nuclear magnetic resonance has been used to study intermediary metabolism in an effort to characterize the metabolic changes associated with the evolution and progression of a variety of human diseases. One clinically relevant disease, prostate cancer, has been shown in *in-vivo* and in vitro studies to undergo unique metabolic changes as the healthy prostate tissue is neoplastically transformed into prostate cancer. *In-vivo*, proton magnetic resonance spectroscopic imaging has confirmed that the healthy glandular tissue in the peripheral zone of the prostate has a uniquely high concentration of citrate and that it is significantly diminished in prostate cancer (46, 108, 109). In vitro, proton NMR spectroscopic studies performed on extracts of transurethral resection specimens (44) and high-resolution magic angle spinning (HR-MAS) spectroscopic studies of intact surgical (40) and biopsy (47) samples taken from human prostate tissue have demonstrated that prostate cancer samples contain significantly higher levels of lactate and alanine than normal prostate samples. Interestingly, the reduction in citrate that occurs with the development of prostate cancer may be related to the higher lactate and alanine observed in prostate cancer. In particular, an increase in glycolytic lactate production may provide the parasitic cancer cells with an energy source that is independent of its oxygen supply, a carbon source for the biosynthesis of cell membranes that begins with lipogenesis (62), and/or an acid source that likely enables the cells to invade neighboring tissue (69). Since the glandular secretory cells in the peripheral zone of the prostate use pyruvate to synthesize and secrete large amounts of citrate, an increase in the conversion of pyruvate to lactate would cause a decrease in citrate production. Alternatively, it has been suggested that the parasitic prostate cancer cells may generate the extra energy they need to grow and proliferate

by increasing citric acid cycle utilization of citrate. The complete oxidation of citrate provides the cancer cells with 171% more ATP per molecule than when citrate is secreted into the prostatic lumen, as it is in healthy peripheral zone tissue. Additionally, an increase in the biosynthesis of fatty acids through lipogenesis would reduce the cytosolic concentration of citrate (62). Turning to alanine, the higher alanine levels may indicate an increase in the conversion of pyruvate to alanine. The increased alanine levels suggest that the cancer cells rely on the oxidation of glutamate, as opposed to the oxidation of pyruvate, to provide the additional carbons required for lipogenesis or that they need the alanine for protein synthesis. Since there is evidence that all of these changes occur with prostate cancer, it would be beneficial to understand the relative importance of these changes in prostate cancer cells or tissue. This knowledge could be used to identify better metabolic biomarkers of prostate cancer evolution, progression, and response to therapy, as well as potentially elucidate new therapeutic targets.

The most reliable way to measure the relative importance of these pathways would be to conduct an experiment that examines all the pathways simultaneously in a controlled environment. Since all the metabolic pathways of interest start with glycolysis, it would be possible to measure the relative activity in these pathways by labeling one of the glycolytic intermediates with ^{13}C and following the label through the pathways. More specifically, by delivering ^{13}C-3 pyruvate to prostate cells or tissue and monitoring the incorporation of the label in downstream metabolites, it may be possible to simultaneously evaluate all the proposed metabolic adaptations that affect alanine, lactate, and citrate production in prostate cancer. While there are many metabolites downstream of pyruvate in the pathways of interest, monitoring the activity in these pathways with NMR techniques requires measurement of metabolites that are outside the cells' mitochondria, unless the cells are extracted prior to the NMR experiments.

The metabolites within the mitochondria typically have very short T_2's, likely due to binding or limited mobility, making them difficult to detect with NMR. Nonetheless, if there is an increase in glycolytic lactate or alanine production, ^{13}C-3 lactate or alanine will be produced. Similarly, an increase in citrate oxidation by the citric acid cycle would cause an increase in ^{13}C-4 and ^{13}C-3 glutamate. An increase in lipogenesis and fatty acid synthesis would produce more ^{13}C labeled cytosolic acetyl-CoA and fatty acids. In addition, the sparsity of the ^{13}C NMR spectrum makes identification and quantitation of peaks easier than for the proton spectrum, which is relatively crowded with significant overlap between peaks. Therefore, the relative significance of the pertinent metabolic pathways was assessed by delivering ^{13}C-3 pyruvate to the primary cultured human prostate cells or tissue and analyzing the sample with ^{13}C HR-MAS spectroscopy.

In order to use ^{13}C-3 pyruvate to investigate the metabolic adaptations that occur with the evolution of prostate cancer, the prostate cancer model system must accumulate a sufficient amount of ^{13}C label in the reporter metabolite for each pathway of interest. Since the flux through some of these pathways is relatively low, such as fatty acid synthesis for example, the model system must be viable for multiple days. Ideally, the model system will yield 15-30 mg of cells or tissue per sample for the HR-MAS analysis. The larger samples will increase the amount ^{13}C labeled compound present in each sample, which will increase the SNR of the ^{13}C HR-MAS spectra. Since these sample sizes are relatively large (typical HR-MAS samples range from 3-30 mg for prostate tissue), the model system must yield a relatively large amount of prostate cells or tissue without dramatically increasing the time and effort required to produce the sample. As a result, the model system must be widely available or easily derived from a wide range of patients. In the following section, the labeling patterns following exposure

to ^{13}C-3 pyruvate were investigated in two prostate cancer model systems that use tissue specimens from surgically removed human prostates.

4.2 Primary Cultured Epithelial Cells

In an attempt to better understand the metabolic adaptations that occur *in-vivo* with prostate cancer, it would be ideal to conduct the ^{13}C labeling experiments in pure human prostate cancer cells. One difficulty with the assessment of prostate cancer *in-vivo* and of prostate biopsies in vitro is that stromal and benign glandular tissue can be mixed with cancerous tissue. While significant advances have been made in spectroscopic imaging of the prostate, imaging resolution is not sufficient to produce voxels that contain only one type of tissue (110). Similarly, in vitro studies of prostate cancer biopsies followed by histological examination have shown that there is significant presence of these benign tissues in the cancer biopsy samples as well (35, 111). However, during the past two decades, the procedures and conditions required to isolate and culture unaltered human prostate cancer cells have been established and are typically referred to as primary cultures. The primary cultures are grown from a small population of parent cells that have been histologically classified using the clinically accepted Gleason Grading system, and thereby provide a uniform population of cells for experimentation. Furthermore, the reproducibility of the results can be assessed because multiple NMR samples can be grown from the same parent population. As an added benefit, cell cultures provide the ability to directly control and vary the concentration of ^{13}C labeled substrate available to the cells and the amount of time they are exposed to the substrate. Whereas, *in-vivo* the substrate concentration in the extra-cellular space can only be indirectly controlled. Primary cultured cells are preferred over immortalized cells because the immortalization of the cells can directly affect their function and metabolism. Therefore, the primary cultures provide an opportunity to investigate how human

prostate cancer cells, which have been classified using the clinical histological grading system, behave as they grow and proliferate.

The measurement of the ^{13}C labeled metabolites requires very sensitive NMR techniques for the following reasons. The NMR measurements must be capable of detecting the ^{13}C labeling in approximately 2e6 cells because the primary cultured prostate cells are only viable for a limited number of population doublings and their availability is somewhat limited. While NMR extraction protocols often require 1e8 cells for a single sample, HR-MAS spectroscopy has the ability to record spectra from smaller samples. HR-MAS spectroscopy is a rapidly developing technique that allows solution-like NMR spectra to be obtained from intact tissue and cell specimens while preserving the tissue for further pathologic and genetic study (35-42). The solution-like linewidths are achieved by spinning the sample at a rate sufficient to remove much of the chemical shift anisotropy present in intact cell and tissue samples. The sensitivity of the HR-MAS is very high because it employs an RF coil with a very small diameter, making it a very sensitive detector. Additionally, since the HR-MAS experiments are performed on intact samples, the measurements are unaffected by any artifacts the extraction process may introduce. On the negative side, the intact samples make it possible for metabolic conversion to occur during the HR-MAS experiments because the samples still contain all their enzymes. As a result, the samples are usually cooled to 1°C during the HR-MAS experiment in an attempt to minimize the metabolic activity that occurs during the HR-MAS experiment, a time when the sample is not provided with physiological levels of nutrients or oxygen.

The goal of this study was to develop a method for studying metabolism of intact primary cultured prostate cancer cells using HR-MAS and to evaluate how well the cells incorporated ^{13}C-3 pyruvate into the metabolic pathways implicated in the citrate, lactate,

and alanine changes that occur with the formation and evolution of prostate cancer. As part of the study, a cell culture protocol was developed that successfully incorporated the label from ^{13}C-3 pyruvate into many of the reporter metabolites of interest. In addition, the culture protocol was optimized to permit measurement of ^{13}C labeling in intact cells with HR-MAS spectroscopy. This required making changes to the medium near the end of the cell culture's life and determining how to prepare the cells for the HR-MAS experiment (harvesting the cells, removing the media, freezing the cells, and transferring them to the HR-MAS rotor) while maintaining the metabolic integrity of the cells. An HR-MAS spectroscopy protocol was established that provided a measurement of the amount of metabolite present in the cells, the fractional enrichment of the metabolites, and the concentration of the ^{13}C labeled pool for the metabolites. Finally, an initial comparison was made between the metabolic adaptations proposed to occur with prostate cancer and a preliminary comparison was made between Gleason grade 3+3 and 4+3 primary cultured prostate cancer cells.

Materials and Methods

Cell Culture and Labeling Procedure

In this study, cancers from 5 different prostate cancer patients were studied. Two of the cancers were from Gleason grade 4+3 prostate cancer samples, while three were Gleason grade 3+3. The primary cultured prostate cancer cells were isolated and cultured based on a technique previously developed by Peehl et al (112, 113). Briefly, cells were harvested using ultrasound-guided needle biopsy or from radical prostatectomy specimens and then incubated in specialized media. PFMR-4A medium, which was used to culture the cells once they reached 50% confluency, was a serum free medium that was supplemented with cholera toxin, bovine pituitary extract, epidermal growth factor, insulin, phosphoethanolamine, hydrocortisone (1 pg/ml),

selenous acid, retinoic acid and gentamicin. Cells were passaged twice, and grown until they reached 80% confluency, resulting in 5 to 8 HR-MAS samples for each cancer. Since the PFMR-4A medium resulted in significant contamination of the proton spectrum, even after washing the cells three times in phosphate buffered saline (PBS), a modification was made to the cell culture protocol described in (112). The majority of the spectral contamination shown in Figure 4.2, which overlapped with aspartate at 2.8 ppm, creatine at ~3.0 ppm, choline at ~3.2 ppm, and the glx C-2 peaks at 3.75ppm, was traced to the HEPES buffering system in the PFMR-4A medium. For this reason, Dulbecco's Modified Eagle's (DME) medium, which results in less contamination, was used for the final 24 hours of cell culture. The supplements to the PFMR-4A medium mentioned above were added to the DME medium along with 1mM glucose and 1mM pyruvate. Additionally, threonine was excluded from the DME medium because the threonine resonance at 1.33 ppm significantly overlaps the lactate resonance at 1.31 ppm and was detected in the ^{1}H spectra when it was present in the medium.

Following incubation in DME for 24 hours, the DME medium was aspirated from the cell culture plate. Then DME medium containing 5 mM ^{13}C-3 pyruvate and 1 mM unlabelled glucose was added to the cells, and they were returned to the incubator. For one set of cells, several different labeling durations were used: 30 min, 60 min, 90 min. It was determined that after 60 minutes, the glutamate C-4 enrichment had reached a maximum. For the remainder of the cells, therefore, a 60 minute labeling duration was implemented.

Harvesting the Cells

Following incubation in labeled medium, the conditioned medium was aspirated from the plate. Plates were washed in 25 mL of phosphate buffered saline (PBS), which was then aspirated. Tryp-LE was added to the plate, and the plate was returned to the

incubator for 6 minutes. Following trypsinization, the cells were maintained at a maximum of 1˚C in order to minimize degradation and further metabolism. The cells were washed by adding 25 mL of PBS, previously cooled to 1˚C, to the plate. The cell suspension was transferred into a 50 mL conical tube and centrifuged at 1˚C and 400 RCF for 5 minutes. The supernatant was then aspirated.

Cells were washed a second time by resuspending them in 2 mL of 1˚C PBS. The suspension was pipetted into a sample tube as described below and centrifuged for 5 minutes at 1˚C and 400 RCF again. The sample tube was broken at the point at which it had been scored, and the top part of the apparatus was discarded. The supernatant was aspirated from the remaining portion of the tube. The tube was capped at the top, transferred to a cryo-container, and cooled to -80˚C for storage.

Preparation of Sample Tubes

For HR-MAS studies, a sample must be placed in a rotor (sample holder) that is 3 mm in diameter. In order to minimize metabolic activity and breakdown of the cells during the transfer to the rotor, the harvested cells must be stored in such a way that they can be transferred to the rotor without thawing. A specialized apparatus was constructed for this purpose. The narrow end of a shortened Pasteur pipette was inserted into a modified blood Caraway Tube (2.8 mm inner diameter, Chase Scientific Glass, Inc., Rockwood, TN). The two glass components were fused together using an epoxy to seal the joint between them. A rubber cap was placed at the bottom of the blood capillary tube, and the tube was scored with a metal file approximately 3 cm from the bottom so that it could later be broken. A fully assembled sample tube is shown in Figure 4.1.

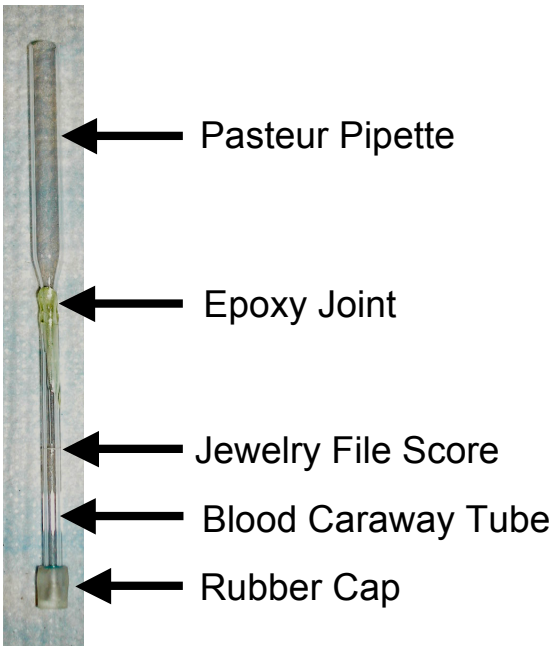

Figure 4.1 A photograph of a sample tube just after fabrication. The sample tube was assembled from a modified Pasteur pipette and a modified blood caraway tube.

HR-MAS Experiments, Data Acquisition and Processing

A sample tube containing frozen cells was removed from the freezer and placed on dry ice. A 35-µL leakproof zirconium HR-MAS rotor (Varian Inc, Palo Alto, CA) was weighed using a balance capable of 0.01 mg accuracy. Three microliters of D2O+TSP was pipetted into the rotor and provided a frequency reference. Three microliters of 101.24 mM ^{13}C-2 glycine was then added to the rotor to enable calibration of the ^{13}C pulses and provide a quantification reference for the HSQC spectra. The sample tube was removed from the dry ice, and its two rubber caps were cut off. The frozen cell sample was transferred to the HR-MAS rotor by holding the sample tube above the rotor and pushing the cells out the sample tube into the rotor using a small plastic rod. Following the insertion of each solution or cell sample, the rotor was weighed in order to determine the mass of the most recently added substance. The HR-MAS rotor was then assembled and closed as previously described by Swanson et al. (40).

The cell sample was analyzed using Varian INOVA 11.7 T (500 MHz for ^{1}H) spectrometer equipped with a 4 mm gHX nanoprobe, previously cooled to 1˚C. Once the rotor was loaded into the HR-MAS nanoprobe which held the sample at the magic angle, the sample was spun at 2,250 Hz and maintained at 1˚C. A pulse-acquire sequence was used to obtain a 1H[13C] spectrum with a 90˚ flip angle, 30,000 complex points, 20 kHz bandwidth, TR = 7 s, 128 averages, and 10 dead scans for a total scan time of 16.1 minutes. As described in Chapter 3, the carbon decoupling was implemented using the GARP scheme with a pulse power of 43dB. The result spectrum was zero-filled to 131,072 points and Fourier transformed.

To obtain information from ^{13}C labeled metabolites, a HSQC experiment was performed, allowing detection of signal only from those protons that were attached to ^{13}C nuclei. The evolution times were set to a single bond scalar coupling (J_{CH}) of 143 Hz, which corresponds to the J-coupling constant for the C-2 labeled glycine reference. This choice necessarily resulted in incomplete polarization transfer for ^{13}C labeled metabolites of the pyruvate substrate, including glutamate C-4 (J_{CH} = 127 Hz), glutamate C-3 (J_{CH} = 130 Hz), aspartate C-3 (J_{CH} = 129 Hz) (J_{CH} = 130 Hz), alanine C-3 (J_{CH} = 130 Hz), and lactate C-3 (J_{CH} = 128 Hz). However, correction was made for the incomplete transfer, as described below. HSQC spectra were acquired with 4096 points and a 10 kHz spectral width along the proton dimension, 256 complex increments and a 15 kHz spectral width along the carbon dimension, GARP ^{13}C decoupling during the data acquisition, a TR of 2.41 s, 32 dead scans, and 8 averages for each increment leading to a total scan time of 2.78 hrs. Linear prediction was used along the ^{13}C dimension to produce an additional 512 points resulting in a matrix size of 4,096 X 768 points. This matrix was then zero-filled to 16,384 X 4,096 points and multiplied by Gaussian apodizations in both dimensions before Fourier transformation. Following the HSQC

experiment, a second 1H[13C] spectrum was recorded to determine whether the metabolite concentrations had changed during the course of the HR-MAS experiment.

Quantitation

Metabolites were quantified by integrating the peaks in the 1D and 2D spectra. For the ^{1}H data, the spectra were baseline corrected and integrated using the frequencies whose intensities are 5% of the peak height as the integration limits. The amount of each metabolite ($Moles_X$) was calculated using the ^{13}C-2 glycine reference as follows:

Eq. [4.1]
$$Moles_x = \frac{Area_x}{Area_{Gly}} * \frac{NEP_{Gly}}{NEP_x} * Moles_{Gly}$$

where $Area_X$ and $Area_{Gly}$ are the peak areas in the ^{1}H spectrum for the metabolite of interest (X) and glycine, respectively; NEP_X and NEP_{Gly} are the number of equivalent protons for X and the glycine reference; $Moles_{Gly}$ is the number of moles of the glycine reference that were added to the HR-MAS sample. A similar method was used to calculate the amount of ^{13}C labeled metabolite ($Moles_{13Cx}$) from volumes of the cross peaks in the HSQC data, with a small correction factor included to account for incomplete polarization transfer as shown in Eq. [4.2].

Eq. [4.2]
$$Moles_{13Cx} = \frac{Vol_{13Cx}}{Vol_{13C-Gly}} * \frac{NEP_{Gly}}{NEP_X} * \frac{1}{\cos\left(2\pi \frac{J_{CHx}}{143}\right)} * Moles_{13C-Gly}$$

where Vol_{13Cx} and $Vol_{13C\text{-}Gly}$ are the peak volumes in the HSQC spectrum for the metabolite of interest (X) and ^{13}C-2 glycine, respectively; J_{CHx} is the J-coupling in hertz for X; $Moles_{13C\text{-}Gly}$ is the number of moles of the ^{13}C-2 glycine reference that were added to the HR-MAS sample. The concentration of the ^{13}C labeled metabolites was calculated by dividing $Moles_{13Cx}$ from Eq. [4.2] by the mass of the HR-MAS sample.

The fractional enrichment of the metabolite (FE_X) was calculated by computing the ratio of the two quantities calculated in Eq. [4.1] and Eq. [4.2]:

Eq. [4.3] $$FE_x = \frac{Moles_{13Cx}}{Moles_X}$$

For this calculation, the $Moles_X$ was determined from the first $^1H[^{13}C]$ spectrum recorded for each cell sample.

Results

Reducing Contamination

The ^1H spectra in Figure 4.2 illustrate that the PFMR-4A medium produced several large peaks. While the glutamine concentration was much higher in the PFMR-4A medium, it was present in both media (Figure 4.2), resulting in uncertainty in the quantitation of glutamine in the proton spectra from the cells. Most of the other large peaks (highlighted with black stars at 2.6, 2.87, 3.15, and 3.75 ppm in Figure 4.2A) present in the PFMR-4A medium spectrum were absent from the DME medium and were produced by the HEPES component of the PFMR-4A medium. When the cells were cultured in this medium and washed three time with cold PBS, high concentrations of glutamine were observed in the proton spectra along with spectral contaminants at ~3.0, ~3.2, ~3.8, and ~3.9 ppm as shown in Figure 4.2B. Because of these observations, the medium was switched to DME for the final 24 hours of the experiment. The proton spectra in Figure 4.2B from the cells cultured in the complete DME medium for the last 24 hours of the culture demonstrated a reduction in the glutamine concentration and all of the spectral contaminants. The final adjustment to the cell culture protocol was made by optimizing the number of times the cells were washed in cold PBS after they were harvested. Figure 4.3 demonstrates the tradeoff between

residual medium contamination and the number of washes performed during the cell harvesting process. The third wash further reduced the spectral contamination caused by the PFMR-4A medium. However, it also washed away the metabolites of interest, as evident from the reduction in PC and myo-inositol seen in Figure 4.3. While the spectral contamination at ~3.2 ppm was slightly higher with two washes, it did not obscure the peaks from the choline containing compounds. In addition, the metabolite intensities were higher with two washes and the other spectral contaminants were virtually unchanged. Therefore, the cell cultures were washed only two times for the remaining experiments.

The Proton Spectrum

Similar to the published spectral profiles for prostate cancer tissue, the representative $^{1}H[^{13}C]$ HR-MAS spectrum in Figure 4.4 contains high levels of phosphocholine (PC) and lactate and no citrate. In addition, the high spectral resolution of these intact cell samples readily permits identification of alanine, creatine, choline, glycerophosphocholine (GPC), and myo-inositol (mI) in the spectra, many of which are the subject of current prostate cancer research. Very important to the ^{13}C labeling experiments included in this study, aspartate and glutamate have very prominent resonances in the spectra, along with glutamine, glutathione, and an n-acetyl moiety. The strong glycine resonance was produced by the ^{13}C-2 glycine reference added to the HR-MAS sample. While there are still contamination peaks present in the $^{1}H[^{13}C]$ spectra, they are small enough and isolated enough that most of the metabolites are easily identified and quantified. The high PC levels suggest that the cells were actively growing and proliferating, indicating the cells cultures were viable when they were harvested. The high lactate levels are little more difficult to interpret, particularly since the lactate levels change significantly during the course of the HR-MAS experiments as

summarized below. Also, as noted above, glutamine was present in the modified DME medium that was used for the final 24 hours of incubation and for the 60-minute labeling experiment. Therefore, it is unknown if recorded glutamine levels are representative of the intrinsic cellular concentrations or if they have been biased by the presence of glutamine in the medium.

The HSQC Spectrum

The representative ^{13}C HSQC spectrum presented in Figure 4.5 clearly demonstrates that it is possible to measure ^{13}C enrichment of metabolites in an intact prostate cancer cell sample using HR-MAS. The most prominently labeled metabolites were C-3 lactate, C-3 alanine, C-4 glutamate, C-2 glutamate, C-3 aspartate, and C-2 aspartate. Also labeled were an N-acetyl peak, C-2 glutamine, C-3 glutamine, C-4 glutamine, and C-4 glutathione. While the PC was observed in the HSQC spectrum, its peak represents natural abundance enrichment. The large peak at 3.54 ppm was from the ^{13}C-2 glycine reference compound. As a side note, the spectrum in Figure 4.5 was graphically modified by removing the T_1 noise from the ^{13}C-2 glycine peak in the carbon dimension. This was done to facilitate easy viewing of the 2D spectrum and its projections. Very importantly, since lactate, alanine, and glutamate, three of the reporter metabolites of interest, were significantly labeled with ^{13}C after the cells were offered ^{13}C-3 pyruvate for just two hours, it is clear that the ^{13}C labeling experiments will provide a mechanism for comparing the metabolic adaptation proposed to occur with prostate cancer evolution.

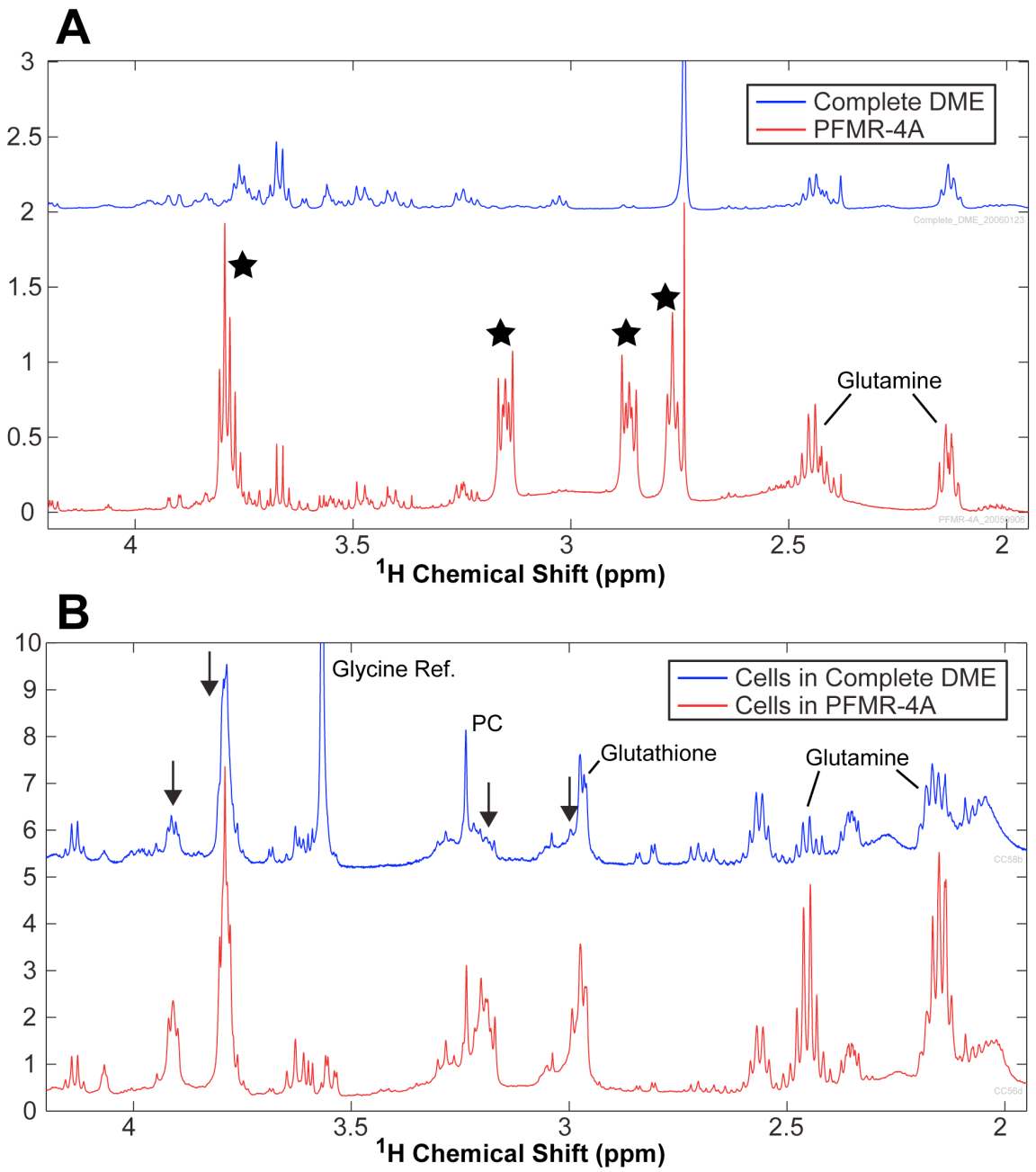

Figure 4.2 **(A)** Proton HR-MAS spectra of DME medium *(TOP)* and PFMR-4A medium *(BOTTOM)*. The PFMR-4A spectrum contains several large peaks (★) that ultimately contaminated the spectra of the cells cultured in this medium prior to harvesting the cells as shown in the bottom of **(B)**. By culturing the cells in DME for the last 24 hours *(TOP of B)*, the spectral contamination caused by the PFMR-4A medium was significantly reduced as indicated by the black arrows. In addition, the glutamine levels were significantly reduced because the DME medium contained less glutamine. Note the large glycine peak in the DME cell spectrum was produced by the reference compound added for the HR-MAS experiment. Also, the chemical shifts of the contaminants were slightly different in the cells than in the medium solution, which was likely caused by binding differences.

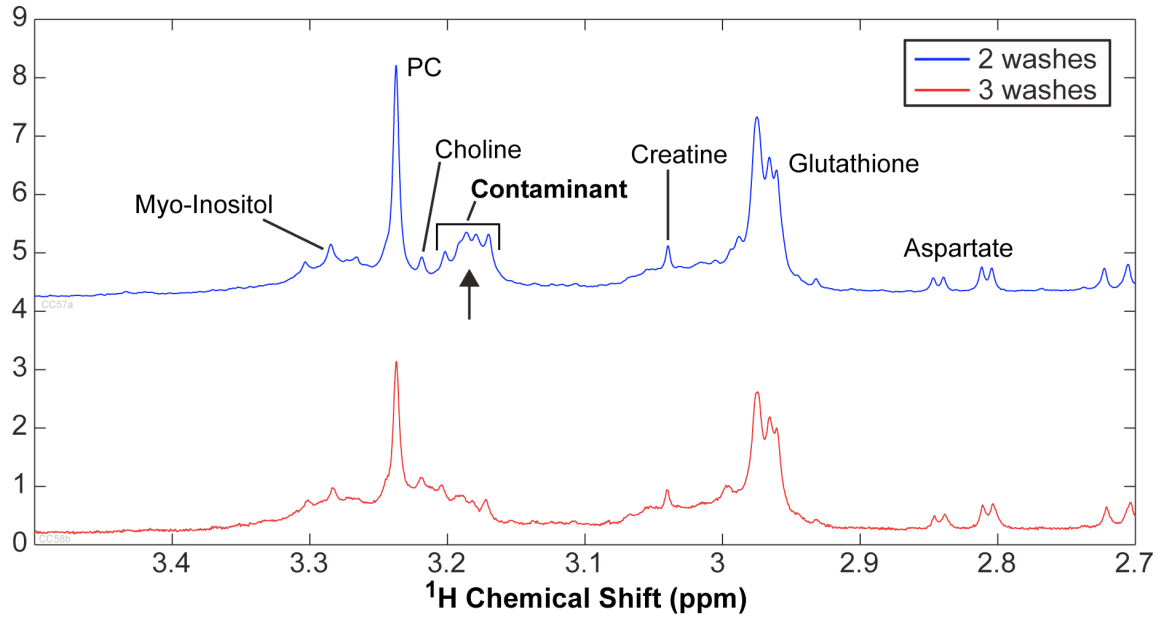

Figure 4.3 $^{1}H[^{13}C]$ HR-MAS spectra of primary cultured prostate cancer cells after the cells were washed with cold PBS twice *(TOP)* and three times *(BOTTOM)*. The contaminant at 3.18 ppm was residual contamination from PFMR-4A medium and was slightly higher when the cells were only washed twice. However, the PC peak was also larger with two washes, suggesting that the additional wash removed metabolites as well. Ultimately, two washes were used in the experiments in order to avoid washing away metabolites at the expense of some minor additional contamination.

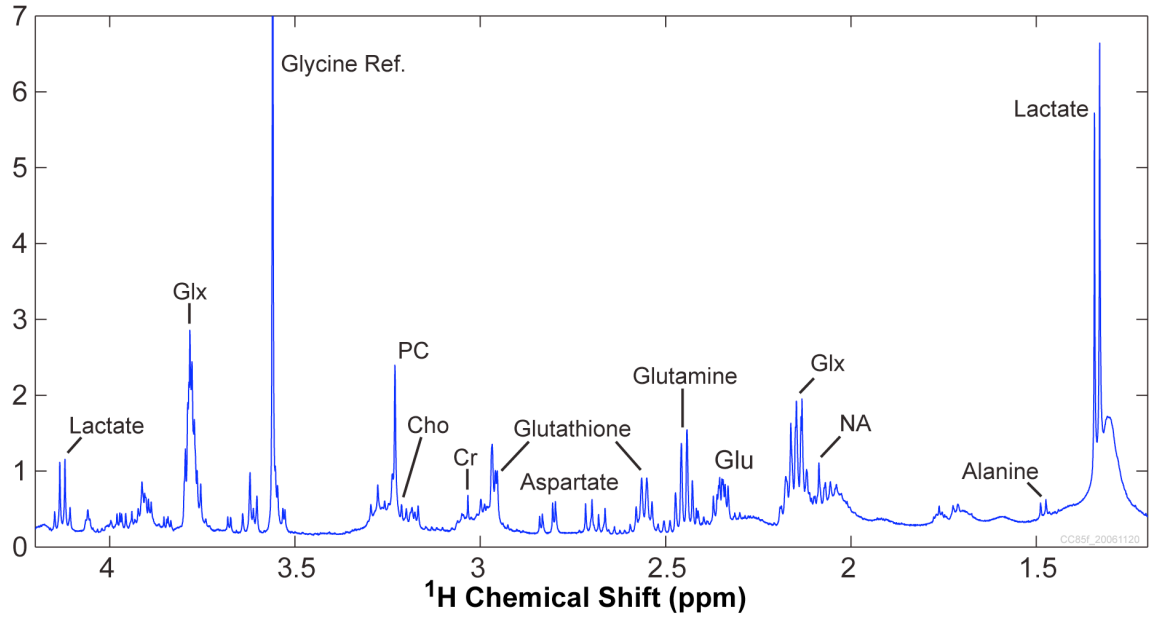

Figure 4.4 Representative $^1H[^{13}C]$ HR-MAS spectrum from primary cultured prostate cancer cells. The spectrum was acquired from 25.6 mg of cells in 16.1 min. Prominent peaks include the glycine reference, lactate, phosphocholine (PC), aspartate, glutathione, glutamine, glutamate (Glu), and Glx (composite of glutamate, glutamine, and glutathione). Cho: choline; Cr: creatine; NA: N-acetyl peak.

Comparison of $^1H[^{13}C]$ spectra obtained before and after the HSQC experiment demonstrated that lactate was the only metabolite that changed during the HSQC experiment. Thus, with the exception of lactate, the duration of the HSQC experiment had no affect on the results of the metabolic measurements because the metabolism reflected in these measurements took place during the cell-labeling portion of the experiment rather than during the HR-MAS measurements. Lactate, however, increased in concentration by approximately 80% in the 2.78 hours between the first and second one-dimensional acquisitions. The significant evolution of lactate during the HR-MAS experiment, indicating there was significant LDH activity even at 1˚C, precluded the precise quantitative evaluation of lactate in these experiments. Nonetheless, the lactate FE computed using the first $^1H[^{13}C]$ experiment provided an estimate of the upper limit for the FE of the primary cultured prostate cancer cells.

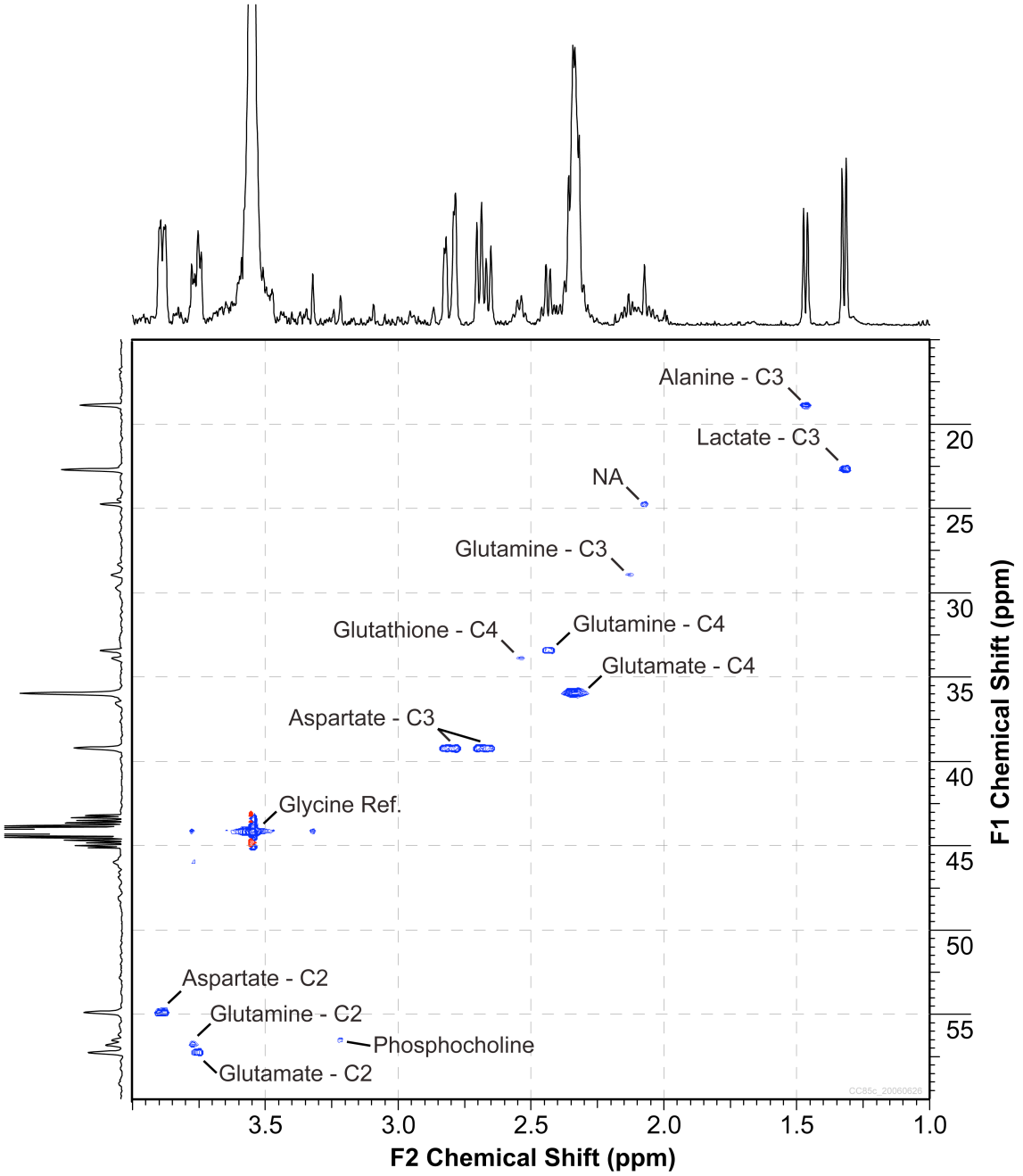

Figure 4.5 Representative ^{13}C HSQC spectrum from primary cultured prostate cancer cells using HR-MAS. Maximum intensity projections along ^{1}H and ^{13}C dimensions are shown at the top and left, respectively. The spectrum was acquired from 26.5 mg of cells in 2.78 hrs. It contains strong ^{13}C labeled signals from Glutamate-C4, Aspartate-C3, Alanine-C3, Lactate-C3, Aspartat-C2, and Glutamate-C2. Since the relative peak intensities for the prominent peaks in this spectrum are greater than their relative intensities in $^{1}H[^{13}C]$ spectrum (Figure 4.4), it is clear that the ^{13}C label is incorporated into the pathways of interest.

Quantitative Results:

As demonstrated by the fractional enrichment plot in Figure 4.6A, the C-3 of alanine, the C-4 of glutamate, C-3 of glutamate, and the C-3 of aspartate were enriched well above the natural enrichment of 1.1% along with a slight enrichment of the C-3 of lactate for all the prostate cancer patients' cells. The metabolite enrichment values for the samples from the first three patients were from Gleason grade 3+3 cancers and the last two were from Gleason grade 4+3 cancers. The average relative standard deviations for the fractional enrichments for each cancer were 12.6, 11, 9.4, and 22% for C-3 alanine, C-4 glutamate, C-3 aspartate, and C-3 lactate, respectively. While there was no significant difference between the 3+3 and 4+3 cancers, there was a difference in the FE for the various metabolites. Average enrichment across all cancers was 32.4 ± 5.4% for C-3 alanine, 24.5 ± 5.4% for C-4 glutamate, 9.1 ± 2.5% for C-3 glutamate, 25.2 ± 5.7% for C-3 aspartate, and a maximum of 4.2 ± 1.0% for C-3 lactate. Even more striking, there was a substantial difference in the amount of ^{13}C labeled metabolite that was produced for each of the reporter metabolites following the two hour incubation of the cells with medium containing ^{13}C-3 pyruvate. In particular, the amount of ^{13}C-4 glutamate was produced during the labeling experiment was substantially more than amount of ^{13}C compound produced for the other reporter metabolites. Combing all of the samples, the prostate cancer cells produced an average of 0.115 ± 0.061 mM of C-3 alanine, 1.21 ± 0.29 mM of C-4 glutamate, 0.440 ± 0.11 mM of C-3 glutamate, 0.308 ± 0.12 mM of C-3 aspartate, and 0.154 ± 0.031 mM of C-3 lactate.

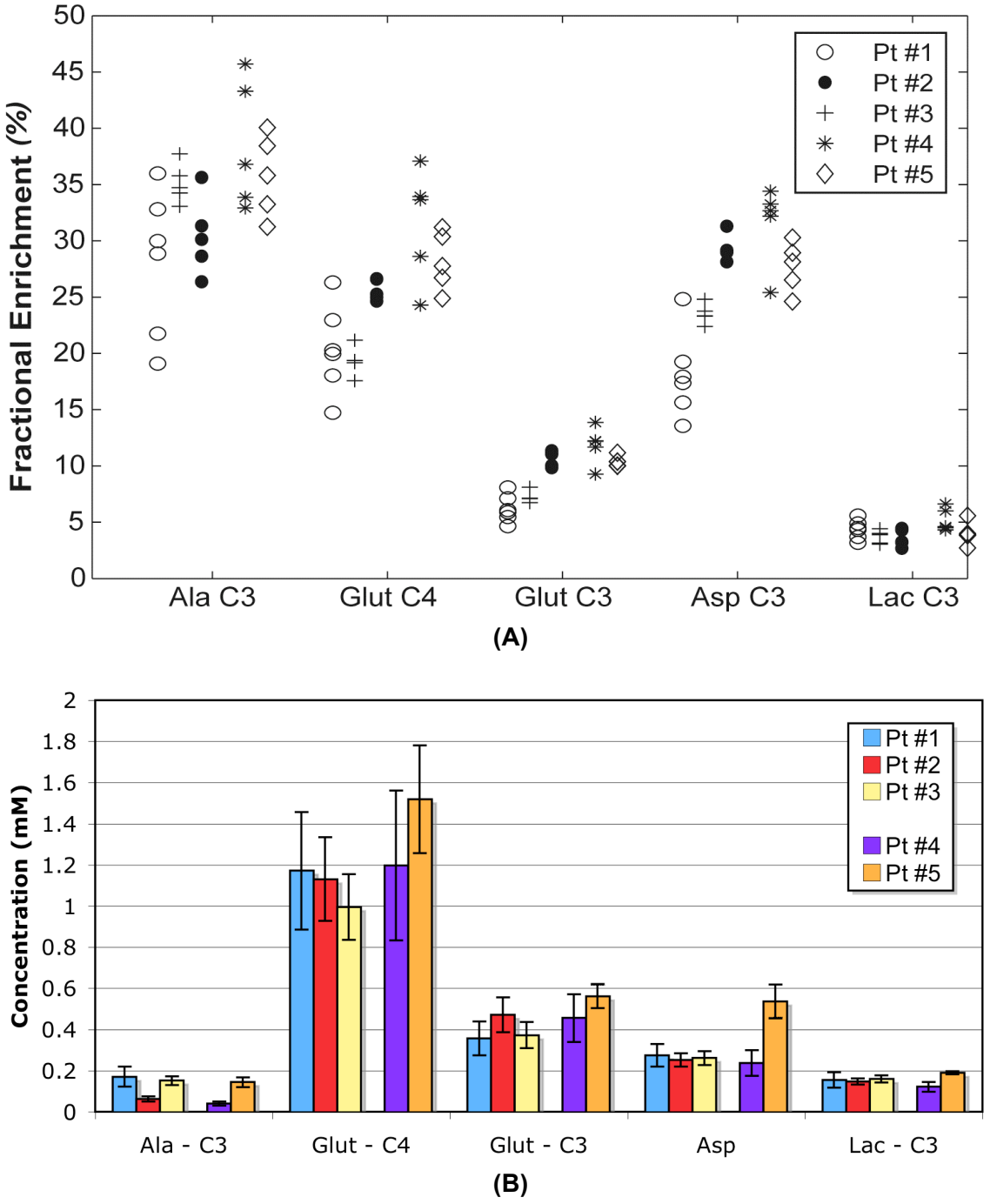

Figure 4.6 **(A)** Fractional enrichment of the several metabolites following the delivery of ^{13}C-3 pyruvate to primary cultured prostate cancer cells derived from five different prostate cancer patients. The prostate cancers from patients 1-3 had a Gleason score of 3+3 and the patients 4 and 5 had a Gleason score of 4+3. **(B)** The average and standard deviation of the concentration of the ^{13}C pool for each of the metabolites is also presented. While all the metabolites were enriched above natural abundance, the ^{13}C-3 pyruvate was converted to glutamate more than any of the other metabolites during a 2 hour exposure to the pyruvate. Pt: Patient; Ala: Alanine; Glut: Glutamate; Asp: Aspartate; Lac: Lactate.

Discussion

This work describes a new method for performing HR-MAS spectroscopy on intact prostate epithelial cells grown in primary culture, and provides a method to analyze their metabolism using information obtained from both ^{1}H and ^{13}C spectra. By performing the experiment using intact cells rather than extracts, fewer cells were necessary to produce a single HR-MAS sample; cell samples were estimated to include approximately 10^6 cells while cell extracts require 10^7 (114) or more cells. In optimizing the cell harvesting procedure, a simple device was employed for centrifugation of the cells, and it was determined that two washes of the cells in PBS were sufficient. Although an additional wash is usually performed on cultured cells before NMR experimentation, experiments showed that there was some loss of signal from metabolites when three washes were used rather than two. Although this resulted in greater contamination of the spectrum with elements of the PFMR-4A medium, it was determined that two washes represented a reasonable compromise between spectral contamination and preservation of the metabolites.

The results of the one-dimensional experiments yielded several new conclusions, which can best be appreciated by comparison to prior work. Yacoe et al (114) previously studied high resolution NMR of prostate cancer cells in primary culture. A number of conclusions of that study are corrected here. First, the large complex peaks that were found at 2.87 and 3.15 ppm in that study were assigned to α-ketoglutarate. This was a somewhat surprising observation because this metabolite is usually present in tissue in low concentrations, and is indirectly observed as its conjugate amino acid, glutamate. In our study of the cell culture media, it was found that these peaks were in fact not from the cells but rather from the medium. Similarly, the large unidentified triplet found at 2.73 ppm was seen to come from the PFMR-4A medium as well. The absence of these spurious peaks in the cell spectra described in this work, because of the use of

a modified DME medium for the final 24 hours of incubation, enabled observation of aspartate in the $^{1}H[^{13}C]$ spectra. This is of interest because aspartate is hypothesized to play a significant role in the metabolism of both normal and diseased prostate (115, 116), and we confirmed that although the peaks are relatively small, it is nonetheless present. Furthermore, it is significantly enriched upon incubation with ^{13}C-3 pyruvate.

The N-acetyl peak has been observed previously in some proton spectra. Schiebler et al (117) performed in vitro studies of human adenocarcinoma and benign prostatic hyperplasia using proton NMR spectroscopy and noted a significant N-acetyl peak at 2.05 ppm in a minority of samples. The peak was tentatively but not definitively assigned to N-acetyl neuraminic acid. In all of our studies, we observed the same resonance, albeit in lower concentrations. The peak was easily observed in the HSQC spectra, where it was well separated from other metabolites. In the one-dimensional proton data, it was partially obscured by the strong C-3 resonances of glutamate, glutamine and the glutamyl moiety of glutathione. Because quantitation of the N-acetyl peak in the $^{1}H[^{13}C]$ experiment was difficult due to overlap with other resonances, fractional enrichment of this peak could not be calculated. In the cell samples from at least one of the cancers (patient 4), however, significant fractional enrichment of the N-acetyl resonance was present. This claim is evidenced by the fact that the N-acetyl peak was far higher than that of the glutamate C-3 peak in the HSQC spectrum, while in the $^{1}H[^{13}C]$ spectrum the N-acetyl peak was too low to distinguish from the glutamate C-3 peak. Therefore, it seems likely that a metabolic pathway from pyruvate to the N-acetyl molecule exists, likely via the PDH enzyme, which produces acetyl CoA from pyruvate. Polymorphisms in the N-acetylase enzymes, NAT1 and NAT2, have been associated with several cancers, including prostate cancer in particular (118, 119). The

method of metabolic profiling described in this work will allow further characterization of this association.

The ^{13}C HSQC spectra recorded from intact primary cultured cells under HR-MAS conditions provided a robust measurement of ^{13}C labeling in all the metabolites observed in the $^{1}H[^{13}C]$ spectra from the cell samples. Although the duration of the HSQC experiment was relatively long at 2.78 hours, the resulting spectra obtained from these experiments demonstrated high SNR and easily identifiable peaks. Acquisition of $^{1}H[^{13}C]$ spectra before and after the HSQC data demonstrated that with the exception of lactate, the other metabolites of interest were stable throughout the HR-MAS experiment. This supports the conclusion that the quantitation of these metabolites reflects metabolism that occurred during the incubation of cells in medium rather than during the HR-MAS measurements. Although lactate enrichment cannot be absolutely quantified because of the lactate synthesis that occurred while the cells were in the HR-MAS spectrometer, an upper bound on the lactate ^{13}C enrichment can be determined using the HSQC peak volume and the peak area of the first $^{1}H[^{13}C]$ experiment. Finally, the method used for quantifying enrichment demonstrates sufficient reproducibility that enrichments of glutamate and aspartate can be measured with 10% precision, and alanine within 12%. In fact, the precision of the FE was superior to the precision of the metabolite concentrations calculated using the values from Eq. [4.1] and the samples' masses (data not shown). The poor precision in the metabolite concentrations was likely caused by an error in the accuracy of the reference compound added (in this case glycine) or by a variation in the hydration of the cells when they were weighed. An increase in the hydration of cells would have lowered the measured metabolite concentration because the additional water would have increased the sample's mass.

The fractional enrichment estimates avoided both of these problems because it did not use the sample's mass and the amount of glycine canceled out in Eq. [4.3].

By virtue of the excellent reproducibility of the fractional enrichment calculations between different samples taken from the same cancer, the results of the experiments indicate that the percent enrichment calculated for a single sample is in fact representative of the cells from that sample. The metabolites that show the greatest degree of enrichment in our combined proton and HSQC experiments are alanine, glutamate C-4, and aspartate C-3. Comparing the Gleason grade 3+3 and 4+3 cancers, there was no obvious difference in percent enrichment of any metabolite between the cells with the higher Gleason score and those with a lower Gleason score. The lack of a statistically significant difference was likely due to the small sample size. With a larger sample size, significant differences may emerge between the different grades of prostate cancer.

Combining all the sample from the five cancers, alanine was the most enriched, while glutamate and aspartate also exhibited significant enrichment. However, the fractional enrichment did not permit comparison of the amount of each metabolite that was produced from the ^{13}C-3 pyruvate because the FE was biased by the concentration of metabolite that existed prior to the labeling experiment as well as any amount of the metabolite that was derived from other substrates. However, it was possible to make relative comparisons of the conversion of pyruvate through the pathways of interest by analyzing the concentration of the ^{13}C labeled pool for each metabolite. Based on the data in Figure 4.6B, it is clear that more pyruvate was converted to glutamate than other metabolite, evidence of progression of pyruvate into the citric acid cycle. Interestingly, the amount of pyruvate converted to lactate and alanine was an order of magnitude less

than the glutamate conversion, with lactate conversion being slightly greater than the alanine conversion.

Comparing these result to other ^{13}C studies of cancer cells, Wehrle used ^{13}C-1 glucose to probe metabolism in EMT6 tumor cell spheroids and found that the glucose was metabolized almost entirely to ^{13}C-3 lactate (120). Singer used ^{13}C-1 glucose to probe metabolism of HCT-116 cells on microcarrier beads and concluded that they exhibited a high level of aerobic glycolysis because 63% of glucose was shunted to lactate (121). In the present study, some pyruvate was metabolized to lactate but, far more was converted to glutamate. The low lactate evolution relative to glutamate evolution suggests that prostate cancer exhibits significant citric acid cycle metabolism. This would be consistent with a large body of work by Costello and Franklin (62, 122-127), who have studied the loss of the citrate production in secretory prostatic cells, which occurs when the cells become cancerous. Their bioenergetic theory suggests that the secretory prostatic cells transform from citrate producing cells to citrate oxidizing cells to provide the energy the prostate cancer cells need for the activities of carcinogenesis (60). This transformation would provide the cells with 171% more ATP per glucose molecule.

In addition to increase citrate oxidation, there are other plausible explanations for the difference in flux to lactate seen in the primary cultured prostate cancer cells and the other cell lines. First, the other studies used ^{13}C-1 glucose as a substrate while a high concentration of pyruvate was used in this study. When traversing the pathway from glucose to lactate, no net NADH is produced or consumed. However, when pyruvate is converted to lactate, one net NADH molecule is consumed and NAD+ is produced. Since NADH was not present in the medium in excess concentration, it is possible that the production of lactate was artificially low because of the absence of the cofactor.

Further experimentation will be necessary to determine if the conversion of pyruvate to lactate was limited by the availability of NADH. Nonetheless, the current results suggest that probing TCA cycle metabolism of prostate cancer by using high levels of pyruvate, may show unique metabolism of prostate cancer. A second possible reason for the difference is the experimental setup. In the previous studies, cells were not cultured on plates but rather on beads or as spheroids. It is possible that a difference in mechanical or structural queues lead to a difference in lactate production. A third explanation for the difference in lactate synthesis between the prostate cancer cells and the other cell lines is that the different cell types have different metabolic behaviors. Since the healthy secretory cells of the prostate already have a unique metabolism, their malignant counterparts may also have a metabolism that is different from other human cells.

The method described here will be used in future work to provide quantitative information about metabolic fluxes. For a system that is in metabolic and isotopic steady state, fractional enrichment measurements of the metabolites described here can be used to calculate citric acid cycle flux, anaplerotic flux, as well as others (128-130). These will be useful in characterizing the change of prostate cells from citrate producing to citrate oxidizing cells when they undergo neoplastic transformation. Further studies of the nature that were described here will be necessary to determine what the appropriate labeling duration is for prostate cancer cells to reach metabolic and isotopic steady state. For a system that is in metabolic but not isotopic steady state, metabolic flux information can be derived from serial enrichment measurements of a single population of cells that are perfused inside a spectrometer (131, 132). Such an apparatus for prostate cancer cells in primary cultures has not yet been developed. However, the reproducibility demonstrated in this work indicates that reliable enrichment measurements can be made

from multiple cell groups grown from the same parent population. By labeling these groups for different durations, kinetic information can be derived.

One shortcoming of this method is the inability to culture normal secretory prostate epithelial cells capable of synthesizing citrate. While metabolic differences between neoplastic cells and normal secretory prostatic cells would likely be apparent in cell cultures, the inability to culture normal cells that produce citrate prevents this observation. This shortcoming likely arises from the absence of stromal cells in the model system, which may be necessary to cultivate citrate-production capability. Thus, a previous study that attempted to compare primary cultured normal secretory prostate epithelial cells to neoplastic prostate cells (114) was unable to demonstrate any significant difference in citrate concentration between these groups, despite the apparent difference in studies of in vitro prostate cancer samples and *in-vivo* studies. Future work on metabolic studies of prostate cancer cells will include co-cultures of prostate epithelial and stromal cells, as well as culture of prostate tissue.

Conclusion:

The method presented in this work for studying metabolism of prostate cancer cells in primary culture enabled quantitation of the fractional enrichment and the concentration of the ^{13}C labeled pool for the metabolic products of ^{13}C-3 pyruvate. Fractional enrichment of these metabolites was consistent to within approximately 10% for multiple cancer samples obtained from the same parent population. While alanine demonstrated the highest fractional enrichment in these cells, more ^{13}C-3 pyruvate was converted to glutamate than any other metabolite, indicating that citric acid cycle metabolism may be the dominate consumer of pyruvate in prostate cancer cells.

4.3 Human Tissue Cultures

The current primary culture techniques and protocols developed for prostate epithelial cells have enabled the investigation of prostate cancer in cell cultures that are closer to the *in-vivo* prostate epithelial cells. However, these primary cultured cells are still not completely representative of the *in-vivo* secretory prostatic cells. Since these cells are transitional epithelial cells, they have not completely differentiated into fully functional secretory prostatic cells. As a result, the healthy, primary cultured prostate epithelial cells do not produce citrate, nor do they possess high levels of polyamines. While it is not known why the primary cultured prostate cells do not differentiate into citrate producing cells, it is clear that the primary cultures lack some of the essential features that exist *in-vivo*. It is possible that these essential features are mechanical queues provided by the three-dimensional structure that exists *in-vivo* and/or the cell-to-cell signaling that occurs between the epithelial cells and the neighboring cells, such as stromal cells. An alternative prostate culture technique that uses thin slices of human prostate tissue for the culture specimens and has been maintained for a maximum of 48 hours. Since this culture technique includes much of the three-dimensional structure that exists *in-vivo* as well as most of the other cell types that reside in the human prostate, the model system may accurately represent the *in-vivo* metabolism of prostate tissue. Therefore, the tissue cultures were investigated as a possible improvement over metabolic model system provided by the primary cultured prostate epithelial cells. An overview of the process for culturing these tissue slices and a summary of the preliminary metabolic experiments conducted on them will be presented in this section.

Tissue Culture Procedure

The preparation of the prostate tissue used for the prostate tissue cultures began immediately after the prostate had been surgically removed from the patient. First, an 8 mm diameter cylinder of tissue was harvested from a region of interest in the excised

prostate. Then, the core of tissue was submerged in phosphate buffered saline (PBS) and briefly stored on ice. Next it was positioned in the center of a barrel shaped, stainless steel embedding tube that contained a warm agarose solution. The floor of the embedding tube was the sample holder / plunger for the microtome. After the entire assembly and its contents were carefully cooled on ice, the agarose solidified and adhered to the microtome plunger. The cylinder of agarose gel surrounding the tissue core attached the core to the microtome plunger as shown in Figure 4.7 and supported the core during the cutting process. Using a Krumdieck Tissue Slicer, a microtome manufactured specially for cutting soft tissue (Alabama Research and Development, Munford, Al), the core was sliced into 300 μm thick disks. The excess agarose was removed from the tissue slices using a cold PBS bath and the slices were either saved for subsequent histological analysis or immediately placed on stainless steel screens that were resting in a custom medium. The screens were designed to fit into the wells of a 6-well culture plate. Histology was taken from the first, middle, and last slices for each core after the slices had been preserved in optimal cutting temperature (OCT) compound, frozen, cut into 10 μm thick sections, and stained with Heomatoxylin & Eosin (H&E). Once the slicing of the tissue core was finished, 2.5 mL of fresh medium was placed in each well of a 6-well culture plate and the stainless steel screens were positioned in the wells. The 6-well plates were placed inside an incubator on a slanted surface that slowly rotated about an axis perpendicular to the surface. Since the tissue slices were raised above the bottom of the culture plate wells by the screens, the rotation of the plates cycled the slices through a period of submersion in the medium followed by exposure to air. The air was warmed to 37°C by the incubator and infused with 5% CO_2. For the preliminary studies presented here, the tissue slices were cultured in this environment for two hours.

Figure 4.7 Photograph of prostate tissue core *(Green Open Arrow)* after it has been embedded in agarose gel *(White Solid Arrow)* to attach it to a stainless steel microtome plunger *(White Star)*.

The tissue slices were cultured in a custom medium that was originally developed for the primary culture of the human prostate epithelial cells. For longer-term experiments, the tissues were maintained in the supplemented PFMR-4a medium that was described in section 4.2. However, as was the case for the HR-MAS spectroscopic studies on the primary cultured prostate epithelial cells, the medium produced many unwanted peaks in the ^{1}H spectra, making it difficult to quantify the metabolites of interest. As a result, for the two hour experiments, the tissue slices were cultured in the same threonine free DME medium after it was mixed with the custom formulation of supplements as was done for the cell cultures. In addition, the tissue culture medium was supplemented with androgens by adding 10nM R1881 to the medium. The glucose concentration was 1mM.

Once the culturing of the tissue slices was complete, they were quickly rinsed in a bath of cold PBS to remove any residual medium that was coating the tissue slices. By culturing the slices in DME and rinsing them with PBS, the ^{1}H spectra obtained from them were almost totally free of contamination. After the slices were carefully strained from the PBS bath, they were placed in a customized sample tube, developed specifically for the tissue slices. The sample tube shown in Figure 4.8 was fabricated by

modifying a transfer pipette. It was designed to from the tissue slices into a cylindrical shape with a 3mm diameter that mimicked the shape of the HR-MAS rotor. By quickly forming them into the shape of the HR-MAS rotor prior to freezing, the slices could be transferred to the HR-MAS rotor at the time of the HR-MAS experiment with minimal effort and without thawing them. Once the tissue slices were collected in the bottom of the sample tube, they were weighed and immediately frozen on dry ice. The frozen samples were stored at -80°C until they were analyzed using an HR-MAS protocol based on the protocol developed for the primary cultured cells. In an attempt to improve the SNR for the spectra from the tissue cultures, the number of averages was doubled for the 1D and 2D HR-MAS experiments resulting in a 31 minute $^{1}H[^{13}C]$ experiment and 5.55 hour HSQC experiment.

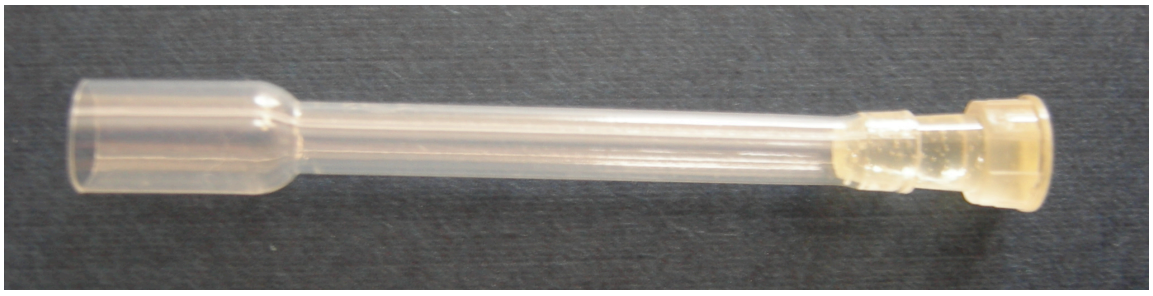

Figure 4.8 A photograph of a sample tube designed for storing tissue cultures. The sample tube was fabricated from a plastic transfer pipette.

Metabolic Accuracy of the Tissue Culture Model System

The representative $^{1}H[^{13}C]$ HR-MAS spectrum presented in Figure 4.9 demonstrates that the tissue culture samples histologically classified as healthy prostate tissue exhibited the characteristic metabolic profile of human prostate tissue with high levels of citrate and polyamines. In addition, the choline containing compounds were similar to *in-vivo* spectra with moderate levels of choline, PC, and GPC. Whereas, the normal primary cultured prostate epithelial cells have exceptionally high levels of PC because they are actively multiplying in the culture environment. Even better, the

representative $^{1}H[^{13}C]$ HR-MAS spectrum from a histologically confirm prostate cancer tissue culture sample exhibited the same metabolic changes observed in *in-vivo* spectra. Namely, PC was higher in the cancer sample and citrate and polyamines were almost eliminated. For comparison, a typical ^{1}H HR-MAS spectrum obtained from a biopsy of healthy prostate tissue and biopsy from cancer are shown in Figure 4.10. Reviewing the histology obtained from the prostate tissue cultures, the H&E stained sections in Figure 4.11 clearly demonstrate that high quality histology can be obtained from the tissue cultures and that loss of the glandular architecture was readily detected in the sections from the cancer samples. Conducting a more comprehensive metabolic comparison across multiple prostate biopsy samples and prostate tissue culture samples, the plots in Figure 4.12 show that there were similar trends between healthy and cancer samples. In particular, there was a decrease in citrate with cancer and an increase in lactate and total choline levels. While the magnitude of the metabolic changes with cancer was somewhat smaller for the tissue culture spectra, the overall accuracy of the tissue cultures as a metabolic model system for prostate tissue was quite good.

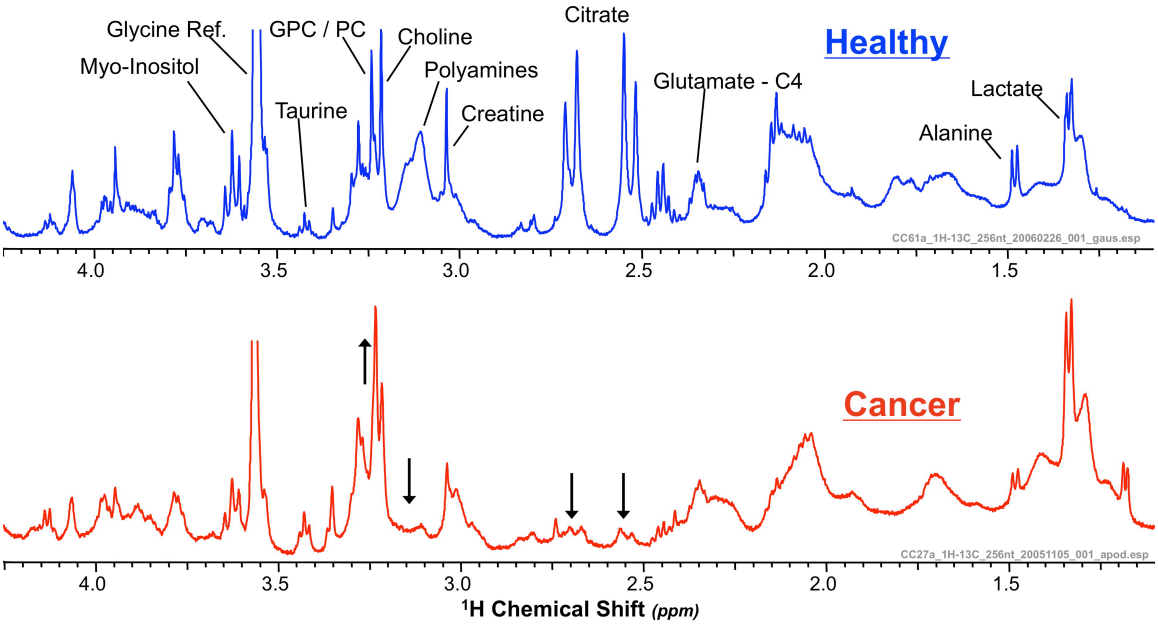

Figure 4.9 $^{1}H[^{13}C]$ spectra acquired from ~25 mg of healthy *(TOP)* and cancerous *(BOTTOM)* prostate tissue slices after being cultured for 2 hours. Similar to *in-vivo* ^{1}H spectra, the healthy sample had high levels of citrate and polyamines and moderate levels of choline. Compare the cancer sample to the healthy sample, it had higher levels of PC and lactate as well as almost no citrate nor polyamines.

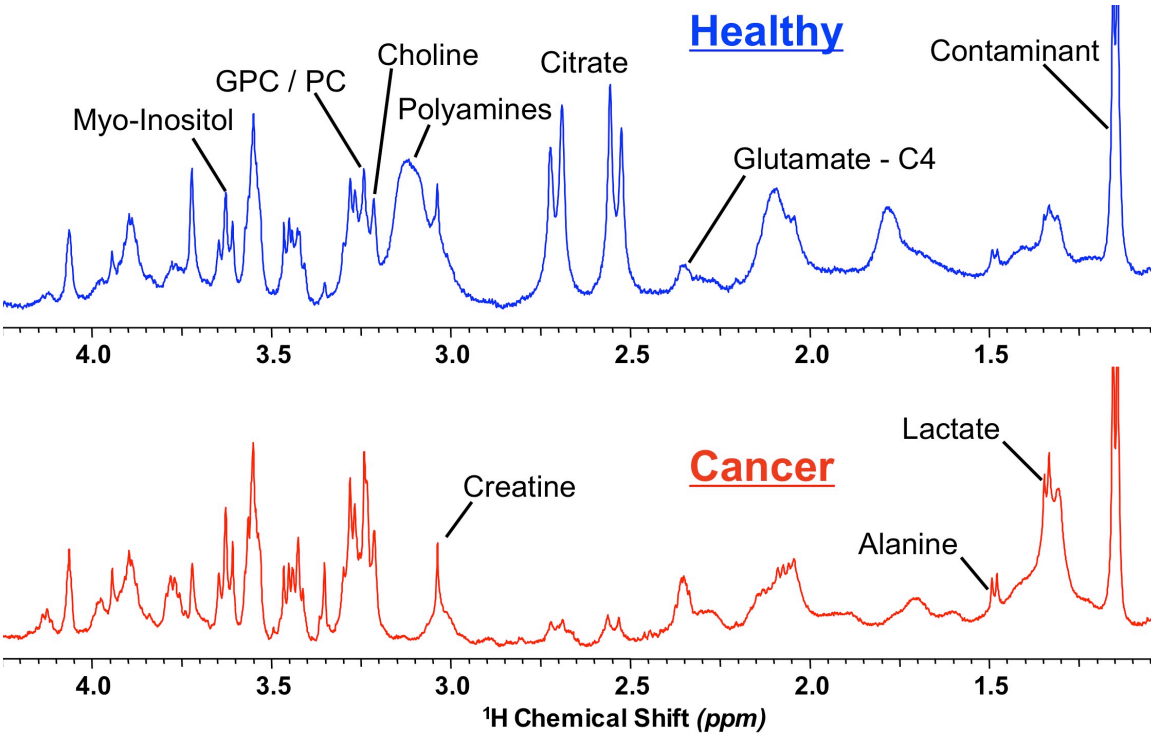

Figure 4.10 Proton spectra acquired from ~5mg of healthy *(TOP)* and cancerous *(BOTTOM)* prostate biopsies. The cancer shows a significant reduction in Citrate, Polyamines, and an increase in GPC / PC and lactate.

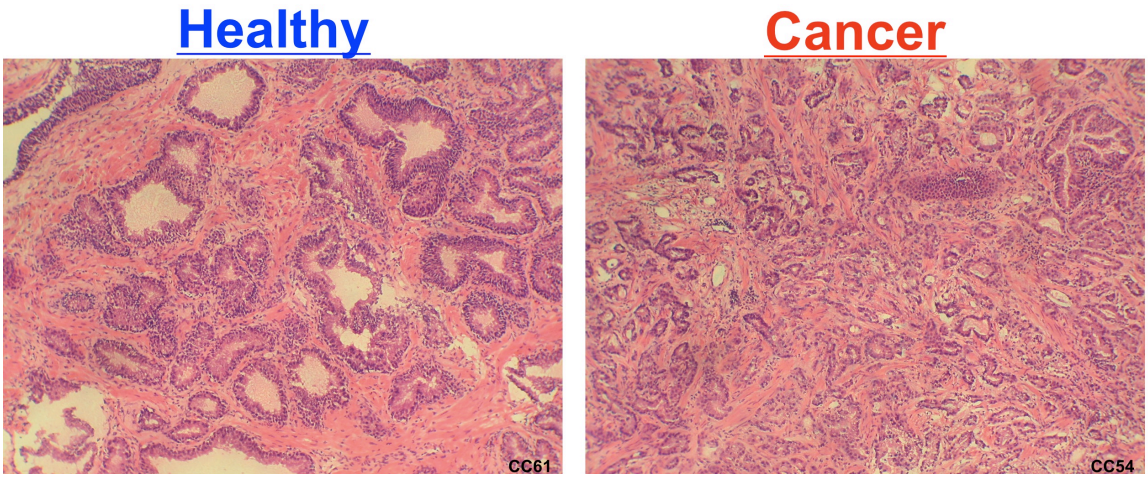

Figure 4.11 Prostate tissue slices viewed under 10X magnification after they were cut into 10μm thick sections and stained with Heomatoxylin & Eosin. Based on the histology, the cancer sample was graded as a Gleason 3+4 cancer.

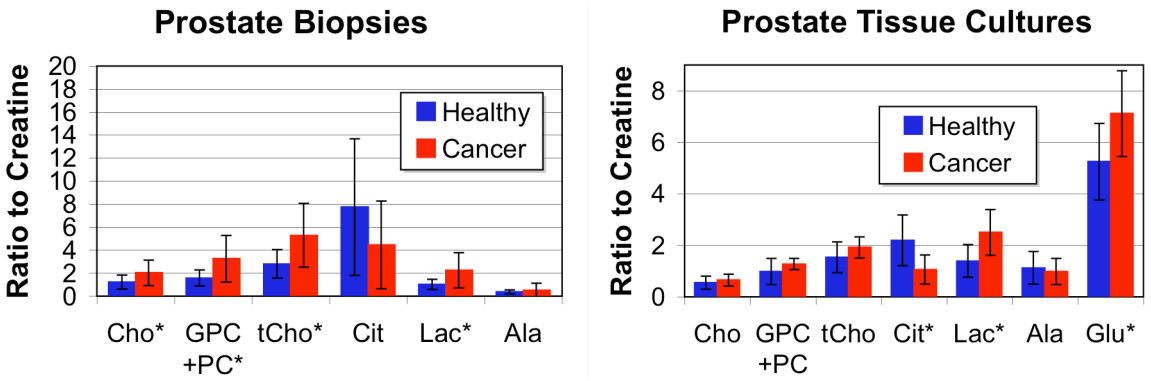

Figure 4.12 Metabolite averages and standard deviations for 10 healthy and 8 cancerous prostate biopsies *(LEFT)*. Averages and standard deviations for 8 healthy and 10 cancerous prostate tissue cultures *(RIGHT)*. Total choline (tCho) was computed by summing choline, PC, and GPC. Asterisks indicate statistical differences.

Investigating Prostate Cancer Metabolic Adaptations with ^{13}C Labeling

Since the prostate tissue cultures provide an accurate metabolic model of healthy and cancerous human prostate tissue, they provide an excellent platform for investigating the metabolic adaptations that have been proposed to occur as the healthy tissue is transformed into cancer. Particularly since the healthy tissue cultures contain high levels of citrate, it may be possible to interrogate the metabolic changes that lead to a reduction in citrate and an increase in lactate and alanine with prostate cancer. Therefore, as part of the preliminary metabolic experiments performed on the prostate tissue cultures, they were labeled with ^{13}C for two hours by adding 5mM ^{13}C-3 pyruvate to the culture medium. The amount of ^{13}C labeling in the metabolic products of pyruvate was measured using an HSQC experiment as was done for the prostate cell cultures. A representative HSQC obtained from a healthy and a cancerous prostate tissue culture are shown in Figure 4.13. Since the fractional enrichments in the healthy sample in Figure 4.13 for glutamate, lactate, and alanine were 6%, 17%, and 38%, respectively, it is clear that the prostate tissue cultures incorporated the ^{13}C-3 pyruvate added in medium into the metabolic pathways of interest. Furthermore, a qualitative comparison of the HSQC spectra in Figure 4.13 indicates that there was increase in the conversion

of ^{13}C-3 pyruvate to ^{13}C-4 glutamate and ^{13}C-3 lactate in the cancerous tissue cultures relative to the healthy tissue cultures. While other changes likely exist in the data, it will require more careful quantitative comparisons of the data to identify those changes.

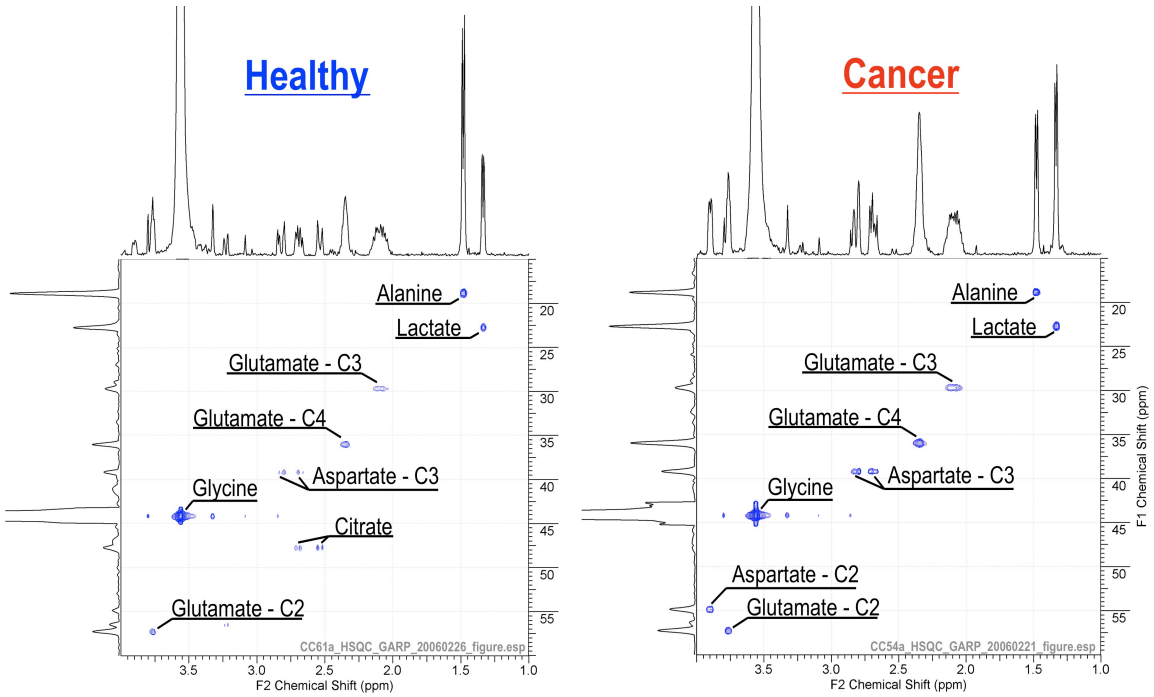

Figure 4.13 ^{13}C HSQC spectra acquired from healthy *(LEFT)* and cancerous *(RIGHT)* prostate tissue slices after being cultured for 2 hours with ^{13}C-3 pyruvate. The cancer sample was graded as a Gleason 3+4 cancer.

As was discussed for the primary cultured prostate cancer cells in section 4.2, the increase in conversion of ^{13}C-3 pyruvate to glutamate strongly supports the hypothesis that citrate oxidation by the citric acid cycle is up-regulated in prostate cancer, referred to as the Bioenergetic Theory of prostate cancer by Costello and Franklin (60). While the primary culture data demonstrated that ^{13}C-3 pyruvate was converted to glutamate more than any of the other reporter metabolites, the preliminary tissue culture data suggests that the pyruvate conversion to glutamate is also much higher in prostate cancer than normal secretory prostate tissue. In addition, the preliminary tissue culture results suggest that there is an increase in the glycolytic lactate production with prostate cancer

since there was more ^{13}C-3 lactate produced in the cancer tissue culture relative to the normal tissue culture. Unfortunately, it is not possible to determine if the increased lactate production was caused by an increased demand for energy, an evolutionary selected adaptation to withstand intermittent hypoxia, an increase need for extracellular acid to invade neighboring tissue, or a need to have extra carbon readily available for fatty acid synthesis. Although, the tissue culture model system may provide an ideal platform for investigating these interesting scientific questions in the future. Perhaps more importantly, the data suggest that the ^{13}C labeling of glutamate and lactate may provide new clinically useful biomarkers. Better yet, recent advances in ^{13}C hyperpolarization techniques may improve the feasibility of performing these time consuming experiments in the clinic.

Chapter 5
Using Hyperpolarized ^{13}C-1 Pyruvate, Lactate, and Alanine to Non-Invasively Detect and Stage Prostate Cancer in Transgenic Mice

The primary cultured human prostate cancer cells and the prostate tissue culture model systems provide the prostate cancer research community with more accurate model systems that can be used for experimental investigations. The results in Chapter 4 indicate that the model systems exhibit metabolic profiles that are very similar, virtually identical in the case of the tissue cultures, to the *in-vivo* metabolic profiles for normal and cancerous human prostate tissue. In addition, the environmental conditions, include access to ^{13}C labeled substrates, can be meticulously controlled for the cultures. Unfortunately, the culturing process and the preparation of the cells and tissue samples for HR-MAS analysis involves many steps and introduces the possibility for increased variability between samples. Furthermore, the measurement of ^{13}C labeling in the HR-MAS samples is rather time consuming because of the small signal produced by the ^{13}C labeled metabolites. Alternatively, one can consider conducting investigational studies on transgenic murine models of prostate cancer, such as the Transgenic Adenocarcinoma of Mouse Prostate (TRAMP) model. While the experimentalist does not have the luxury of directly controlling all the environmental conditions that can be manipulated in the cultures systems, the process for maintaining the system is significantly less involved than that for the cultures. For example, it is no longer necessary to monitor and maintain the pH, temperature, oxygen levels, etc. because the mouse takes care of those issues on its own. Additionally, the process for measuring metabolite levels can be streamlined if they can be measured *in-vivo*. In particular, the sample-to-sample variability introduced by the HR-MAS sample preparation is eliminated. Historically, it has been somewhat technologically demanding to non-invasively measure metabolite levels *in-vivo* because of the limited SNR for these

measurements as was discussed in Chapter 1 and Chapter 2. However, with the new hyperpolarization techniques described in Chapter 2, it may be possible to overcome some of the SNR limitations. While the *in-vivo* metabolic measurements in transgenic mice benefit from some procedural simplifications, they are not perfect. The transgenic mice by definition have a genetic modification that induces the formation of prostate cancer, which may or may not occur with in human prostate cancer. Also, the mice must be anesthetized during the metabolic measurements and they must have a catheter inserted into their vasculature system for delivery of any ^{13}C labeling substrate. Despite these rather minor disadvantages, the transgenic mice provide a unique opportunity to investigate the benefit of using hyperpolarization to measure the metabolic changes that occur with prostate cancer development and evolution.

Recent metabolic studies have indicated that lactate and alanine levels are higher in cancer than in normal tissue (40, 44, 47), and this has been associated with increased glycolysis and cell membrane biosynthesis (62, 69). ^{18}F-2-deoxy-2-fluoro-D-glucose (FdG) positron emission tomography (PET) studies have shown high rates of glucose uptake in several human cancers and that the glucose uptake correlates directly with the aggressiveness of the disease and inversely with the patient's prognosis (133, 134). The high glucose uptake leads to increased lactate production in most tumors even though some of them have sufficient oxygen, a condition know as the Warburg Effect (68) or aerobic glycolysis (69). The increased glycolysis provides the parasitic cancer cells with an energy source that is independent of its oxygen supply, a carbon source for the biosynthesis of cell membranes that begins with lipogenesis (62), and an acid source that likely enables the cells to invade neighboring tissue (69, 135). In the case of prostate cancer, FdG-PET uptake has been shown to correlate with the histological grade and clinical stage of the disease (66, 67). However, FdG-PET has played a

limited role in prostate cancer diagnosis mainly because of the relatively low differential uptake of FdG in most primary prostate tumors and because the bladder produces a very strong FdG signal near the prostate. Meanwhile, proton NMR spectroscopic studies performed on extracts of transurethral resection specimens (44) and HR-MAS spectroscopic studies of intact surgical (40) and biopsy (47) samples from human prostate tissue have demonstrated significantly higher levels of lactate in prostate cancer samples than in normal prostate samples. Based on the FdG-PET studies and the spectroscopic studies, it seems likely that prostate cancer causes or is dependent upon an increase in glycolytic rates as has been suggested for other cancers (69). In addition, the spectroscopic studies found higher alanine levels in prostate cancer samples relative to the normal prostate tissue samples. The extra alanine might be a byproduct of lipogenesis because alanine transamination would support the oxidation of glutamate to α-ketoglutarate, which could provide the carbon molecules required for lipogenesis instead of pyruvate/lactate oxidation (136, 137) or, it may be used directly for protein synthesis. Whatever the biological mechanism may be for the enhanced lactate and alanine production, lactate and alanine levels have yet to be measured non-invasively *in-vivo* because the low concentrations of lactate and alanine in prostate tissue make the detection of these metabolites difficult. Furthermore, the need to suppress large fat signals from lipids surrounding the prostate (138) has made it difficult to observe lactate and alanine with *in vivo* ^{1}H MRSI studies as the lipids resonate at frequencies near lactate and alanine. However, new hyperpolarized ^{13}C spectroscopic imaging techniques (79, 90, 139) may provide an opportunity to observe the changes in lactate and alanine in a clinical MR imaging exam.

^{13}C labeled substrates have recently been polarized using dynamic nuclear polarization (DNP) techniques to obtain tens of thousands fold enhancement of the ^{13}C

NMR signals from the substrate as well as its metabolic products (79, 140, 141). Preliminary DNP studies in rats, rat xenograft tumors, mouse lymphoma tumors, and a transgenic mouse model of prostate cancer have demonstrated greater than 50,000-fold enhancements in the polarization of ^{13}C pyruvate and its metabolic products, lactate and alanine, providing sufficient MR signal for high spatial and temporal resolution spectroscopic imaging of the metabolites (83, 90-92). Pyruvate is ideal for these studies because the hyperpolarized MR signal from the C-1 carbon relaxes very slowly as a result of its long T_1 and it is at the entry point to several important energy and biosynthesis pathways. In particular, it is converted to lactate in glycolysis, to alanine for protein synthesis and/or lipogenesis, and to acetyl-CoA and oxaloacetate to support the TCA cycle and biosynthesis of membrane lipids. Based on the published success of DNP and its application to pyruvate (83, 90, 91), hyperpolarization of ^{13}C-1 pyruvate provides an excellent opportunity to non-invasively measure the lactate and alanine differences that likely exist between the various stages of prostate cancer.

The aim of this study was to quantify the differences in hyperpolarized ^{13}C-1 pyruvate and its metabolic products between the various stages of prostate cancer in the Transgenic Adenocarcinoma of Mouse Prostate (TRAMP) model. The TRAMP model is particularly useful for studying the metabolic changes that occur with prostate cancer evolution and progression since TRAMP mice demonstrate a histopathologic disease progression (142) and the associated metabolic changes that mimic the human disease. Furthermore, preliminary studies have shown that TRAMP mice tumors exhibited significant lactate and alanine signals following the injection of hyperpolarized ^{13}C-1 pyruvate (83). In the present study, normal mice, early stage TRAMP mice, and late stage TRAMP mice were injected with hyperpolarized ^{13}C-1 pyruvate and imaged using a custom 3D ^{13}C MRSI technique. The histopathological findings from the resected

tumors were used to stage the disease and to classify the mice into the three groups. The results from this study provided a 3D visualization of the distribution of hyperpolarized pyruvate and its metabolic products throughout the tumors and the surrounding anatomy. The differences in hyperpolarized lactate levels were so distinct that it would have been possible to non-invasively stage the disease in all but one of the mice included in this study.

Materials and Methods

Animal Preparation and MR System Configuration

All the mice were bred by crossing C57BL6 and FVB mice and were studied under a protocol approved by the UCSF Institutional Animal Care and Utilization Committee. The four TRAMP mice histologically classified as early stage mice (21 - 28 weeks old) and the three late stage mice (27 - 40 weeks old) were imaged a total of 6 times and 5 times, respectively. The five normal mice (17 to 39 weeks old) were imaged a total of 7 times. For all the mice, a 28 gauge catheter that extended from the dorsal surface of their neck was surgically implanted into one of their jugular veins at least one day before the hyperpolarized MR study. At the time of the MR experiment, the mice were anesthetized with 1-1.5% isoflurane and a 90 cm long, 24 gauge extension tube was connected to the jugular vein port (Strategic Applications, Libertyville, IL). This special extension tube made it possible to quickly inject the hyperpolarized agent into a mouse inside a human MR scanner while maintaining a low dead volume in the tubing. Next, the mice were placed on a water-filled, temperature-controlled pad that was heated to approximately 37°C and positioned inside of custom built dual-tuned proton-carbon Transmit/Receive coil. The entire setup was positioned in the bore of a 3T human GE scanner equipped with the multinuclear spectroscopy package (GE Healthcare, Milwaukee, WI).

MR Imaging and Hyperpolarization Studies

All the mice were scanned following a previously published protocol (139). In brief, T_2-weighted ^{1}H anatomical MR images were acquired in sagittal, axial and coronal views. A mixture of ^{13}C-1 pyruvic acid and the trityl radical (tris(8-carboxy-2,2,6,6,-tetra(methoxyethyl)benzo[1,2-d:4,5d′]bis(1,3)dithiole-4-yl)methyl sodium salt) (GE Healthcare, Oslo, Norway) were polarized to 21.7±2.0% using a prototype polarizer developed by GE Healthcare (79). After the mixture was polarized, it was rapidly dissolved into a pH balanced TRIS buffer solution using previously published techniques (79) and yielded a hyperpolarized 79mM pyruvate solution with a pH of 7.9 ± 0.2 (90, 139). Next, the solution was quickly transported to the MR scanner and 350 ± 50μL (28 μmoles of pyruvate) of it was injected into the mouse during a 12 second interval, resulting in a blood concentration of approximately 9mM pyruvate. The hyperpolarized pyruvate was immediately cleared from the injection tubing using a 150 μL saline flush. For the hyperpolarized dynamic study, a ^{13}C spectrum was acquired every 3 seconds from a 10mm thick slab centered on the primary tumor in a late stage TRAMP mouse. The spectra were recorded using a 5° excitation pulse, 2048 points, and a 5 kHz bandwidth. For the hyperpolarized MR spectroscopic imaging studies, a double spin-echo pulse sequence with a small, variable flip-angle excitation pulse, adiabatic refocusing pulses, and a flyback echo-planar readout trajectory was used to acquire *in-vivo* 3D ^{13}C MRSI data in 14 seconds (143). Based on the time course in Figure 5.1, the imaging data acquisition was initiated 35 seconds after the start of the pyruvate injection because the hyperpolarized lactate signal was relatively constant from 35 to 49 seconds. 3D-MRSI data were acquired from the abdomen of the mice using a TE/TR of 140/215msec, an 8x8x16 matrix, a 40x40x86.4mm field of view (0.135 cc spatial resolution), 59 points per spectrum, and a 581 Hz bandwidth.

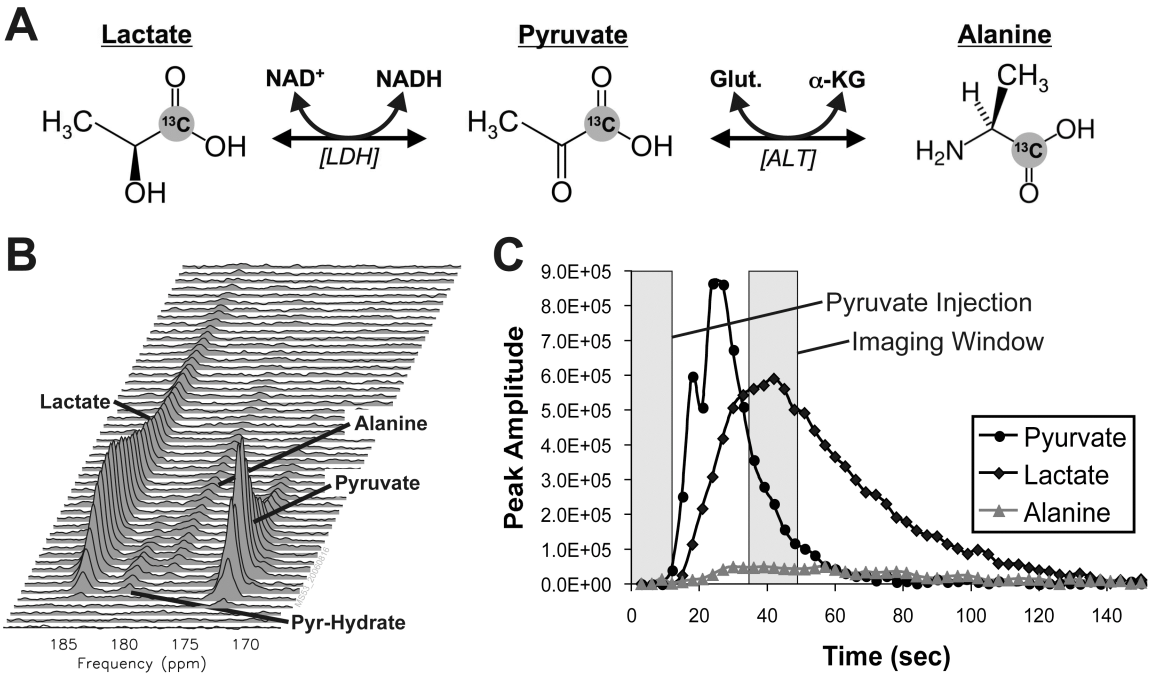

Figure 5.1 Diagram of the ^{13}C-1 pyruvate and the metabolic pathways relevant to this study **(A)**. The hyperpolarized ^{13}C spectra **(B)** and peak height plots **(C)** show the time course for the hyperpolarized ^{13}C-1 pyruvate and its metabolic products following the injection of 350 μL of hyperpolarized pyruvate. The pyruvate was injected at a constant rate from 0 to 12 seconds. The MR spectra were acquired every 3 seconds from a 28 week old TRAMP mouse with a late stage tumor using a 5° flip angle and a 10 mm thick slice. The peak height plot was corrected for the amount of magnetization used to record the previous n spectra by dividing each peak height by $\cos^n(5°)$. The hyperpolarized pyruvate quickly reached a maximum at 24 seconds before being converted to lactate and alanine. Based on this time course, the subsequent MRSI data were recorded between 35 and 49 seconds, a time when the hyperpolarized lactate signal was roughly constant. Glut: Glutamate; α-KG: α-ketoglutarate; LDH: Lactate Dehydrogenase; ALT: Alanine Transaminase.

Histopathological Analysis

The pathology was correlated with the anatomical images by displaying the sagittal, coronal and axial images of the TRAMP mice on a laptop computer during the dissection using OsiriX (Open Source™, Los Angeles, CA). Furthermore, digital photographs and videos were taken during the dissection and subsequently reviewed. The excised tissues were immediately fixed in 10% buffered formalin. Fixed tissue specimens were subsequently transitioned into ethanol and embedded in paraffin

blocks. Tissue blocks were cut into 5 μm thick sections on a Leica microtome. Sections were dried onto glass slides and stained using a standard hemotoxylin and eosin protocol. The percentage of normal, well differentiated (WD), moderately well differentiated (MWD) and poorly differentiated (PD) tissue was estimated from microscopic examination and was used to classify the primary tumors into early and late stage categories (Table 5.1). The percentage of necrosis was also estimated for the early stage tumors and lymph node metastases (Table 5.1). Using these percentages, a histology index was determined for each of the tumors by assigning the normal, WD, MWD, and PD tissue with a value of 0, 1, 2, and 3, respectively. The index was computed by multiplying the volume percentages by these values and summing the weighted percentages. For tumors smaller than 0.2 cc (volume of cylinder containing a 0.135 cc square cuboid), the percentages were adjusted to represent a 0.2 cc volume for the index calculation by assuming the non-tumor tissue in this volume was normal.

Data Processing

The primary and metastatic regions of prostate cancer identified during dissection were traced on the corresponding anatomic images using custom software that reported the volumes for the traced regions. For the hyperpolarized dynamic study, the peak height of pyruvate, lactate, and alanine were measured in the ^{13}C spectrum at each time point, after the spectrum was apodized with a 11.4 Hz Gaussian filter. The metabolite peak heights were then corrected for the magnetization used to acquire the previous time points and plotted as a function of time. For the hyperpolarized carbon imaging studies, the MRSI data were spatially zero-filled to a 16x16x32 matrix, spectrally apodized with a 4 Hz Gaussian filter, frequency referenced to ^{13}C-1 lactate (144), and aligned with anatomical images using custom software. Since the metabolite peak area is proportional to the amount of the metabolite present in the voxel, all of the

spectroscopic voxels were integrated over a predetermined frequency range for each of the metabolites. Images of the lactate integrals were created by spatially interpolating the lactate data to the resolution of the anatomical images using a sinc kernel and overlaying the lactate image onto the anatomical image with 60% opacity.

Data Analysis

For each study, the integrals for a given metabolite from voxels containing the same tissue type were scaled by the noise calculated from a region of the spectrum that did not contain any metabolites and were averaged together. The sum of the lactate, alanine, and pyruvate integrals, labeled Total Hyperpolarized Carbon (THC), was computed and was used as an estimate of the amount of hyperpolarized compounds taken up by the tissue. Using SAS, an Analysis of Variance was computed for each metabolite and for THC along with pair-wise t-Tests across the four groups that were corrected for multiple comparisons with the Tukey correction. A Random Effects model was incorporated into the statistical tests to correct for any correlation that may have been caused by including multiple studies from the same animal (145). Next, the saturation of the conversion of the hyperpolarized compounds to lactate was evaluated for each tissue type by fitting the lactate vs. THC data with a linear function and comparing the slope to one. A slope of one would indicate complete conversion to lactate. Last of all, a correlation coefficient was computed for the histological index and the lactate levels in Table 5.1 as well as the lactate levels in Figure 5.5.

Mouse	Gross Tissue Designation	Histological Classification *(%)*						Volume *(cc)*	Average Metabolite SNR		
		Normal	WD*	MWD*	PD*	Necrotic	Index[&]		Lactate	Alanine	Pyruvate
MS46	Normal	100[§]	0	0	0	0	0	0.068	29	15	32
MS47	Normal	100[§]	0	0	0	0	0	0.051	36	10	24
MS43	Normal	100[§]	0	0	0	0	0	0.038	39	17	64
MS45	Normal	100[§]	0	0	0	0	0	0.058	43	19	72
MS67	Normal	100[§]	0	0	0	0	0	0.043	48	15	46
MS44	Early Tumor	1	94	5	0	0	0.74	0.14	63	20	55
MS72	Early Tumor	15	78	7	0	0	0.92	0.35	61	16	78
MS36	Early Tumor	1	33	1	65	0	1.76	0.15	83	23	52
MS54	Early Tumor	2	35	35	30	0	1.95	0.26	86	18	86
MS61	Late Tumor	0	0	0	81[†]	19[††]	2.43	12.4	128	17	30
MS51	Late Tumor	0	0	1[†]	88[†]	11[††]	2.66	4.0	147	22	50
MS53	Late Tumor	0	0	0	94.5[†]	5.5[††]	2.84	4.3	173	21	78
MS51	LN Metastasis	1	0	0	64	35	1.40	0.14	75	17	48
MS53	LN Metastasis	2	0	0	93	5	1.45	0.10	91	19	60
MS61	LN Metastasis	4	0	0	76	20	2.28	0.99	131	19	31

Table 5.1: Histological classification and average hyperpolarized 13C metabolite SNR for each mouse. *The histological classifications were defined as Well Differentiated (WD), Moderately Well Differentiated (MWD), and Poorly Differentiated (PD). [&]The histological index ranges between 0 and 3, where 0 indicates that 100% of the tissue was normal and 3 indicates that 100% of the tissue was PD. The values for the small tumors were corrected for partial volume effects. [§]The normal mice were assumed to have a 100% normal prostate based on histological analysis of separate mice. [†]Due to the large size of the late stage tumors, the histological classification for these tumors was estimated from 3-5 sections taken from the tumor. [††]The percentage of necrosis for the late stage tumors was estimated from the anatomical MR images because it was not practical to estimate it from the histology.

Results

The hyperpolarization of ^{13}C-1 pyruvate provided ample signal-to-noise for measuring the time course of the delivery of the labeled pyruvate as well as it metabolic conversion to lactate and alanine in a 10mm thick slab from an anaesthetized TRAMP mouse with a late stage tumor as shown in Figure 5.1. The hyperpolarized pyruvate (173 ppm) was detected in the slab approximately 12 seconds after the start of the injection, and it reached its maximum level approximately 12 seconds later, as expected from a 12 second long injection of pyruvate. Hyperpolarized ^{13}C-1 lactate (185 ppm) was observed in the axial slab from the mouse almost immediately following the arrival

of the labeled pyruvate and increased in concentration at a slightly slower rate than the labeled pyruvate. Since the labeled lactate was reduced from the labeled pyruvate by lactate dehydrogenase (LDH), the signal from the hyperpolarized pyruvate rapidly decreased from its maximum until the lactate and pyruvate approached isotopic equilibrium at approximately 45 seconds. At this point, both lactate and pyruvate decreased at a slower rate as result of T_1 relaxation, utilization of the hyperpolarized signal for the MR experiment, and possibly metabolic conversation to other compounds. The slow decrease allowed the labeled lactate signal to persist for over two minutes. Hyperpolarized ^{13}C-1 alanine (178.5 ppm) was also observed in the slab through the TRAMP tumor and exhibited a behavior analogous to lactate, except the conversion from pyruvate to alanine was controlled by alanine transaminase and the amount of hyperpolarized alanine produced was an order of magnitude lower than that of lactate. The pyruvate-hydrate (181 ppm) present in the spectra followed the same time course as pyruvate because it was in equilibrium with the pyruvate. However, it had a substantially lower signal level. While the time course of the hyperpolarized pyruvate and its metabolic products contained a wealth of biological information, it was mainly used to plan the timing of the spectroscopic imaging experiments for this study.

Out of the seven TRAMP mice included in the hyperpolarized imaging experiments, three were histologically classified with late stage tumors and four were classified with early stage tumors. The late stage TRAMP mice had very large primary tumors and peri-aortic lymph node metastases that were 6.9 ± 4.8 and 0.41 ± 0.50 cm^3, respectively. As indicated in Table 5.1, the late stage primary tumors were almost exclusively poorly differentiated cells with a histological index between 2.4 and 2.8. The lymph node metastases were mostly poorly differentiated cells along with some necrosis and had a histological index between 1.4 and 2.3. A representative TRAMP mouse with

a late stage 4.3 cm^3 tumor and a right peri-aortic lymph node metastasis is shown in axial cross-section in the anatomical image in Figure 5.2A. The spatially interpolated hyperpolarized lactate image from this mouse presented in Figure 5.2B shows a very strong lactate signal (165 ± 34) from the active region of the primary tumor and a moderately strong lactate signal (104 ± 6.5) from the lymph node metastasis. The remaining tissue, including the necrotic regions in the anterior aspect of the tumor, yielded orders of magnitude lower lactate. The grid of ^{13}C spectra taken from the 3D MRSI shows a high lactate-to-pyruvate ratio across the tumor (2.2 ± 0.48) and in the lymph node metastasis (2.0 ± 0.03) along with low alanine levels relative to pyruvate. All the metabolite levels in the spectra located outside of the tumors were substantially lower.

The early stage TRAMP mice had primary tumors that were 0.23 ± 0.10 cm^3 and were comprised of well differentiated, moderate well differentiated, and poorly differentiated tumor tissue along with a few normal epithelial areas (Table 5.1). Their tumors had histological indices ranging from 0.7 to 1.9. As illustrated by the representative case in Figure 5.3A and Figure 5.3B, the early stage primary tumors were clearly visualized on the anatomical images and exhibited higher hyperpolarized lactate levels (75) than the surrounding tissue. The carbon spectrum taken from the 3D MRSI shows that the hyperpolarized lactate and pyruvate levels were comparable in the early stage tumors, whereas the alanine levels were again much lower.

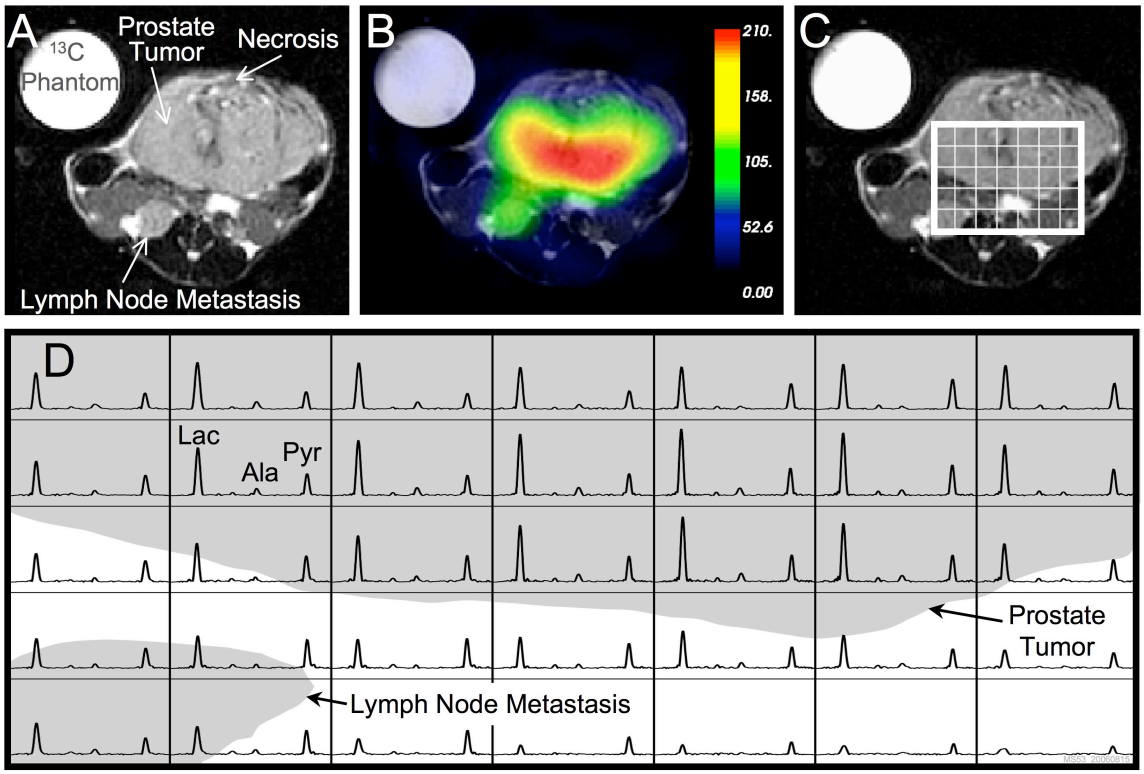

Figure 5.2 Axial T_2 weighted ^{1}H image depicting the primary tumor and lymph node metastasis from a Late Stage TRMP mouse **(A)** and the overlay of an interpolated hyperpolarized ^{13}C lactate image following the injection of 350 μL of hyperpolarized ^{13}C-1 pyruvate **(B)**. After spatially zero-filling and voxel shifting the ^{13}C spectra to maximize the amount of tumor in the voxels, a subset of the spectral grid was selected **(C)** and displayed **(D)**. The 3D MRSI was acquired with a nominal voxel resolution of 135 mm^3 and zerofilled to a resolution of 17 mm^3. The spectra show substantially elevated lactate in the late stage tumor as compared to the early stage tumor shown in **Figure 5.3**. In addition, the metabolite signal is significantly lower in the necrotic regions of the primary tumor. Lac: Lactate, Ala: Alanine, Pyr: Pyruvate.

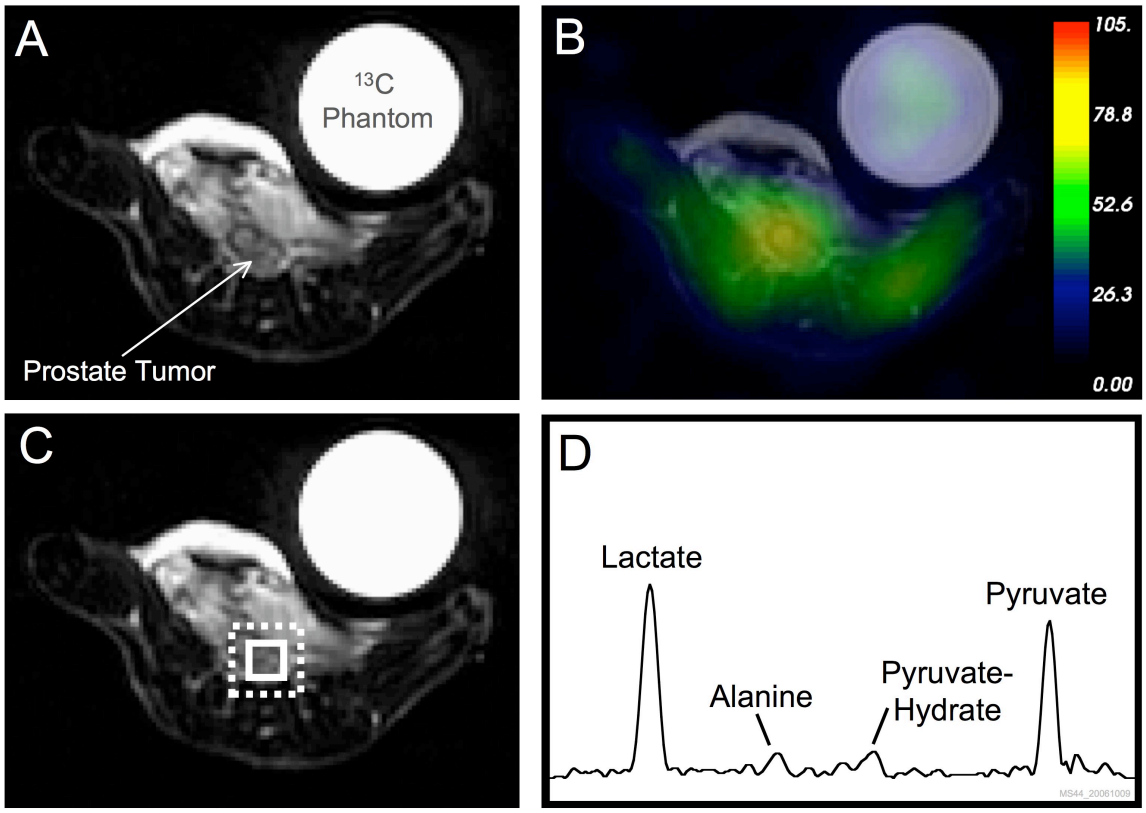

Figure 5.3 Axial T_2 weighted ^{1}H image depicting the primary tumor from an Early Stage TRMP mouse **(A)** and the overlay of an interpolated hyperpolarized ^{13}C lactate image following the injection of 350 μL of hyperpolarized ^{13}C-1 pyruvate **(B)**. The numerical range of the color map in the lactate image was reduced to half the range used in Figure 5.2 to allow visualization of the lower hyperpolarized lactate levels. After spatially zero-filling and voxel shifting the ^{13}C spectra to maximize the amount of tumor in the voxels, one voxel from the primary tumor was selected **(C)** and displayed **(D)**. The 3D MRSI was acquired with a nominal voxel resolution of 135 mm^3 (dashed white box) and zerofilled to a resolution of 17 mm^3 (solid white box). The spectrum shows prominent signals from lactate and pyruvate and smaller signals from alanine and pyruvate-hydrate.

After comparing the hyperpolarized lactate levels with the histological index determined from the H&E stained sections, the lactate levels and histological index had a correlation coefficient of 0.95 when using the average lactate values in Table 5.1 and 0.92 when using the individual lactate values in Figure 5.5. The representative hyperpolarized carbon spectra and H&E stained sections from each of histologically defined groups shown in Figure 5.4 illustrate this strong correlation. The hyperpolarized spectrum from the normal murine prostate exhibited the lowest lactate level out of all the

representative spectra, while pyruvate produced the largest peak in the normal spectrum. As a side note, the normal prostate spectra also included metabolic signals from surrounding tissues since the spectroscopic voxel was larger than the normal mouse prostate. Similar to the healthy human prostate, the murine prostate histology was very glandular with secretory epithelial cells lining the glands and stromal tissue supporting the glands as shown in Figure 5.4A. The histological sections from the early and late stage tumors depict the gradual replacement of the secretory epithelial cells by less differentiated epithelial cells until the glands are completely eliminated and only anaplastic sheets of pleomorphic cells with irregular nuclei remain in the late stage tumors. The carbon spectra showed significant higher hyperpolarized lactate levels in the early and late stage tumors, with the late stage tumors having the highest lactate levels. Pyruvate levels in the early and late stage tumors were similar and were comparable to the normal prostates and lymph node metastases (Figure 5.4). Lactate levels in the lymph node metastases fell between those of the early and late stage tumors. Histologically, the lymphocytes in the lymph nodes were almost completely replaced by poorly differentiate epithelial cells.

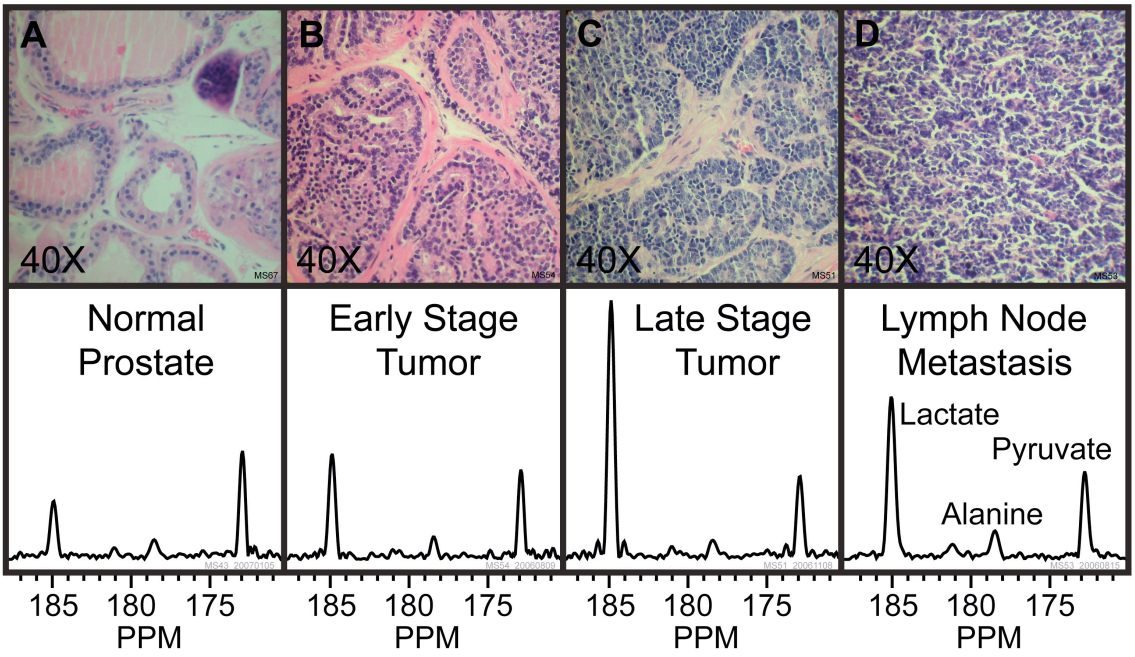

Figure 5.4 Representative H&E stained sections and hyperpolarized ^{13}C spectra for one case from each of the histologically defined groups. The histology slides were processed using 5 μm thick sections and photographed with 40X magnification. The hyperpolarized ^{13}C spectra represent voxels taken from MRSI datasets and normalized to correct for differences in polarization and receiver sensitivity. The normalized spectra illustrate the strong correlation that exists between the amount of hyperpolarized ^{13}C lactate and the progression of the disease from the normal prostates to the early stage tumors and the late stage tumors.

Evaluating all of the samples collectively, statistical comparisons revealed that the lactate levels between all the groups were different with the exception that early stage tumors were not different from lymph node metastases ($p<0.05$). Very importantly, there was almost no overlap between the normal prostates, early stage tumors, and late stage tumors, an essential characteristic of an accurate staging tool. In fact, the lactate levels from 6 of the 7 normal prostates were lower than the lactate levels measured in all the tumors as shown in Figure 5.5. Using the THC as a rough measure of uptake of the hyperpolarized substrates, it was clear that the seventh normal mouse prostate also received much more hyperpolarized carbon. Despite the higher uptake, the lactate levels were only slightly higher, indicating that a small amount of additional

hyperpolarized carbons present in the prostate had been converted to lactate. Whereas, the late stage tumors had much higher THC relative to the normal prostates and much higher hyperpolarized lactate. As a rough measure of the conversion to lactate, the lactate versus THC data for the groups plotted in Figure 5.5D were fit with linear functions. The slopes of the lines were 0.27, 0.41, and 0.53 for the normal prostates, early, and late stage tumors, respectively. Since the slope increased with stage, it suggests that the ability to convert pyruvate to lactate increased with stage or the demand for converted lactate increased with stage. Furthermore, the increase in THC with stage indicates that the uptake of the hyperpolarized compounds increased with stage as well. Statistically, THC levels in the late stage tumors were different from all of the other groups ($p<0.05$). The difference in THC levels between early stage tumors and normal prostates was approaching statistical significance with $p=0.08$. Meanwhile hyperpolarized alanine levels were only marginally different from a statistical standpoint with the comparison between late stage tumors and normal prostates yielding $p=0.05$. Nonetheless, alanine levels exhibited trends that were similar to the trends in lactate levels but with smaller differences and standard deviations as shown in Figure 5.5. The individual hyperpolarized pyruvate values had significant overlap between the groups (plot not shown) and were not statistically different across the groups.

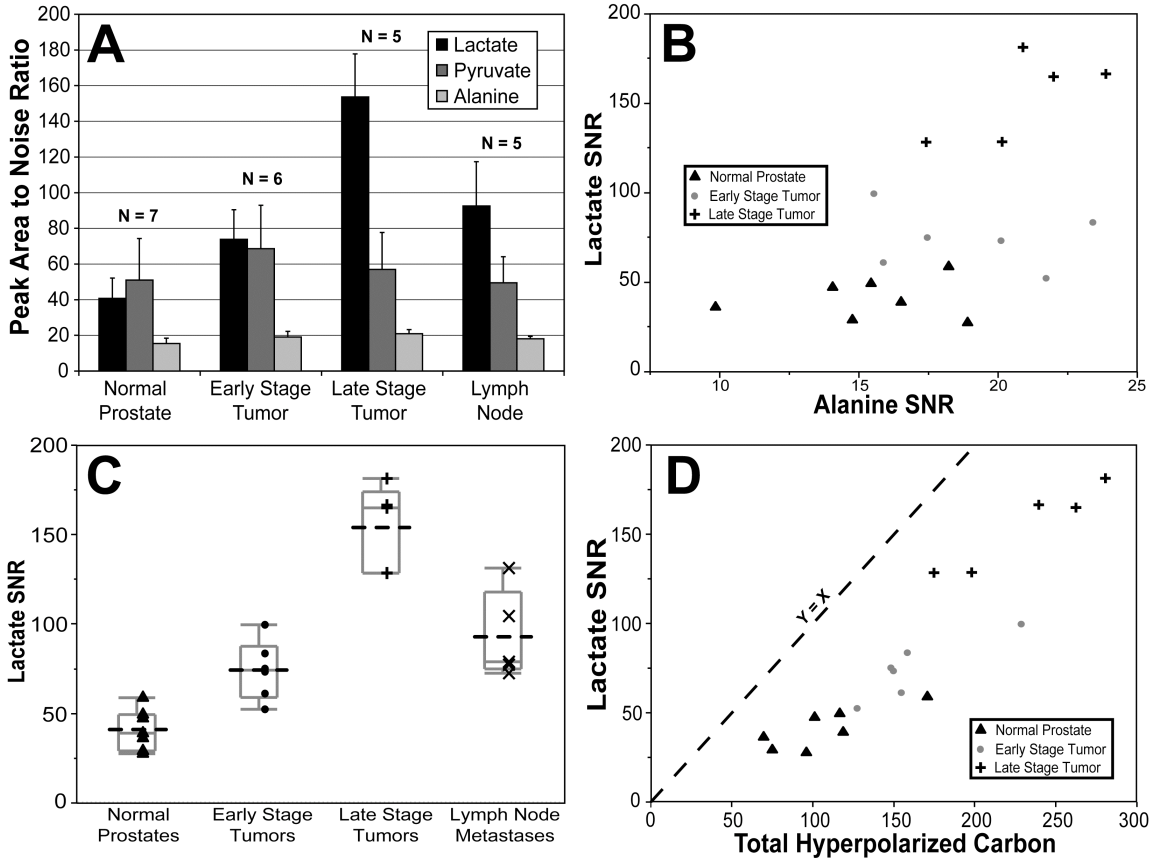

Figure 5.5 Numerical comparisons of hyperpolarized ^{13}C metabolites with the pathologically defined groups. A bar plot summarizes the peak area to noise ratios (average $\pm$ standard deviation) of the ^{13}C labeled lactate, pyruvate, and alanine for the four histologically defined groups **(A)**. The lactate peak area SNR values were statistically different for all four groups, except that early stage tumors were not different from lymph node metastases ($p < 0.05$). While the alanine SNR values were not quite statistically different, they exhibited similar trends to the lactate values as shown by the lactate versus alanine plot **(B)**. The box plot of the individual values for the lactate SNR **(C)** shows that there was almost no overlap between the normal prostates, early stage tumors, and late stage tumors. The plot of lactate versus total hyperpolarized carbon **(D)** suggests that much of the within group scatter of the lactate SNR may be related to variability in the amount of hyperpolarized carbon delivered to the tissue.

Discussion

The data from this study demonstrate that hyperpolarized ^{13}C-1 lactate levels measured after the injection of hyperpolarized ^{13}C-1 pyruvate provide a non-invasive measure of the histological stage (analogous to Gleason grade employed in humans) of prostate cancer in TRAMP mice. Not only were the lactate levels stage dependent, the lactate levels in the tumor were higher than those from the surrounding anatomy

indicating that hyperpolarized lactate has the potential to be a very sensitive biomarker for prostate cancer localization and detection. In addition, the overlap between the normal prostates, early stage tumors, and late stage tumors was minimal with just one normal prostate having a lactate level that overlapped with the early stage tumors.

The hyperpolarized lactate levels were strongly correlated with the cancer's histological index (0.95), which was determined from the amount of well, moderately well and poorly differentiated epithelial tissue present in the tumor. Since the same histological data was used to determine the histological stage, the hyperpolarized lactate levels also correlated with the tumor's stage. Early stage tumors, analogous to low grade tumors in humans, contained a significant percentage of well differentiated epithelium and produced tumors that were slightly larger than the normal murine prostate. Late stage tumors, analogous to advanced, high grade tumors in humans, consisted of mostly poorly differentiated epithelium and coexisted with significant lymph node metastases. The disease progression in the TRAMP mice included in this study was consistent with a previous study, which showed that the TRAMP transgene causes the glandular architecture of the murine prostate to gradually be replaced by less differentiated epithelial cells resulting in primary tumors that are almost entirely poorly differentiated cells in the advanced stages of the disease (146). In addition, the investigators demonstrated that as the primary tumors progressed, the TRAMP mice also develop metastases that first appeared in the regional lymph nodes.

The higher lactate levels found in the tumors are consistent with lactate measurements made on human prostate tissue samples (40, 44, 47) as well as hyperpolarized lactate measurements made in rat tumor xenografts (147) and mouse lymphoma tumors (92). These findings support the hypothesis that the cellular evolution associated with carcinogenesis selects for lactate-producing glycolytic cells because

they can withstand the intermittent hypoxia that malignant cells likely endure and it supports the microenvironmental acidosis they need to breakdown and invade the surrounding healthy tissues (69, 135). Additionally, the larger lactate pool may be a carbon source for the lipogenesis that is required to sustain cellular proliferation (62). Since LDH is the only known mechanism for converting pyruvate to lactate, the hyperpolarized lactate levels reported in this study are likely a reflection of LDH activity within the region of interest. Furthermore, the increase in the slope of the lactate versus THC data indicates that the LDH activity increased as a function of prostate cancer stage. While it is possible that the pyruvate to lactate conversion occurred prior to its delivery to the tumor tissue, the fact that the pyruvate signal buildup preceded the lactate signal buildup in the time course data suggests that the pyruvate was delivered to the tumor tissue. In addition, the hyperpolarized lactate-to-pyruvate ratio was found to be much less than one in the blood of rats with tumor xenografts (91) and the blood of mice with lymphoma tumors (92) that were examined using a similar hyperpolarized imaging protocol. Naturally, these assertions need to be verified in future TRAMP mice studies by directly measuring the LDH activity levels in the tumors and by developing a hyperpolarized imaging technique capable of measuring the time course of the hyperpolarized metabolites in smaller regions of interest.

Differences in hyperpolarized alanine and pyruvate were not as substantial as the changes in lactate across the various tumor stages. Although, the differences were much smaller for alanine, it did show a trend for the same stage dependent changes observed for lactate. A study performed on isolated mitochondria demonstrated that tumor cell mitochondria produced alanine in the presence of pyruvate to support the conversion of glutamate to citrate, which would enable the biosynthesis of new cell membranes (136). These findings along with the elevated alanine levels measured in

human prostate cancer samples (40, 44, 47) suggest that the hyperpolarized alanine differences from this study are real and would have reached statistical significance with a larger sample size. The pyruvate levels were more variable than the lactate and alanine levels and gave no indication of a difference between the groups. Since the hyperpolarized pyruvate signal was rapidly decreasing while the ^{13}C MRSI data were being recorded (Figure 5.1), the large variability was likely caused by the timing of the data acquisition. If one assumes that most of the lactate and alanine were converted from the pyruvate after it arrived in the tissue of interest, then the THC levels provide a good estimate of the amount of pyruvate taken up by the tissue. As it turned out, the THC levels increased with the cancer's stage and suggest that the amount of pyruvate uptake was stage dependent as well. The higher pyruvate uptake in cancer is consistent with a cellular study which demonstrated that a monocarboxylate transporter (MCT-2) had high affinity for pyruvate and had higher m-RNA expression in epithelial tumor cell lines (147). Although the THC levels increased with stage, there was slightly more overlap in the individual THC levels between stages as compared to the lactate levels. However, the THC levels helped explain the variation in lactate levels within each tumor type.

In the clinic, the detailed information obtained from the spectroscopic imaging of hyperpolarized pyruvate and its metabolic products may improve prostate cancer patient care by providing a method to non-invasively characterize cancer throughout the entire prostate with a single procedure. The hyperpolarized MRSI procedures presented here allowed 3D visualization of the distribution of lactate, pyruvate, and alanine throughout the prostate tumor and surrounding anatomy. With this technique, it was possible to non-invasively detect small aggressive tumors as well as regional lymph node metastases. As part of current clinical practice, TRUS guided pattern biopsies, a more

invasive approach, are employed to diagnose prostate cancer, but the procedures are limited by the ability of TRUS to locate the tumor and the small percentage of the prostate that is sampled. Clearly, a more comprehensive non-invasive measurement would be superior. In addition, the strong correlation between the hyperpolarized lactate levels and the tumor's stage, along with the minimal overlap in lactate levels between stages, suggest that physicians could use the information to chose the best therapy and treatment schedule for an individual patient, or improve TRUS guided biopsy planning. For the murine studies presented here, the THC levels did not improve the accuracy of the tumor staging. However, the combination of lactate levels and THC levels may prove even more beneficial than lactate alone for *in-vivo* human exams. From a biological standpoint, the highly reproducible difference in the hyperpolarized lactate levels suggest that the hyperpolarization assay augmented with the appropriate experimental conditions may provide a non-invasive technique for monitoring changes in LDH activity.

Conclusion

In summary, the stage dependence of hyperpolarized lactate levels was measured for the first time in a transgenic mouse model of prostate cancer. The amount of hyperpolarized lactate measured after injection of hyperpolarized ^{13}C-pyruvate demonstrated great potential as a new biomarker capable of non-invasively staging prostate cancer in mice and great potential for future studies of prostate cancer patients. The amount of THC was also stage dependent, but the THC levels in individual tumors produced slightly more overlap between the different tumor stages than the individual lactate levels. However, the THC explained some of the within group variation in hyperpolarized lactate suggesting that a combination of these biomarkers will likely provide the best characterization of prostate cancer aggressiveness in patients.

Chapter 6
References

1. American Cancer Society [homepage on the Internet]. Atlanta (GA): American Cancer Society; c2007 [updated 2007; cited Cancer Facts & Figures 2007. Available from: http://www.cancer.org/docroot/STT/STT_0.asp
2. Carroll PR. Early stage prostate cancer--do we have a problem with over-detection, overtreatment or both? J Urol. 2005 Apr;173: 1061-1062.
3. McNeal JE, Bostwick DG, Kindrachuk RA, Redwine EA, Freiha FS, Stamey TA. Patterns of progression in prostate cancer. Lancet. 1986 Jan 11;1: 60-63.
4. Stamey TA. Cancer of the Prostate: An analysis of some important contributions and dilemmas. Mono Urol. 1982;3: 67-94.
5. Quinlan DM, Partin AW, Walsh PC. Can aggressive prostatic carcinomas be identified and can their natural history be altered by treatment? Urology. 1995;46: 77-82.
6. Jewett HJ. The present status of radical prostatectomy for stages A and B prostatic cancer. Urol Clin North Am. 1975;2: 105-124.
7. Carroll PR, Presti JJ, Small E, Roach Mr. Focal therapy for prostate cancer 1996: maximizing outcome. Urology. 1997: 84-94.
8. Johansson JE, Adami HO, Andersson SO, Bergstrom R, Holmberg L, Krusemo UB. High 10-year survival rate in patients with early, untreated prostatic cancer [see comments]. Jama. 1992;267: 2191-2196.
9. Krongrad A, Lai H, Lai S. Variation in prostate cancer survival explained by significant prognostic factors. J Urol. 1997;158: 1487-1490.
10. Hricak H, White S, Vigneron D, et al. Carcinoma of the prostate gland: MR imaging with pelvic phased-array coils versus integrated endorectal--pelvic phased-array coils. Radiology. 1994;193: 703-709.
11. Hricak H. The prostate gland. *In:* H. Hricak and B. M. Carrington (eds.), MRI of the pelvis, pp. 249-311. London, England: Dunitz, 1991.
12. Kurhanewicz J, Swanson MG, Nelson SJ, Vigneron DB. Combined magnetic resonance imaging and spectroscopic imaging approach to molecular imaging of prostate cancer. J Magn Reson Imaging. 2002 Oct;16: 451-463.
13. Kurhanewicz J, Vigneron DB, Hricak H, Narayan P, Carroll P, Nelson SJ. Three-dimensional H-1 MR spectroscopic imaging of the in situ human prostate with high (0.24-0.7-cm3) spatial resolution. Radiology. 1996 Mar;198: 795-805.
14. Hasumi M, Suzuki K, Taketomi A, et al. The combination of multi-voxel MR spectroscopy with MR imaging improve the diagnostic accuracy for localization of prostate cancer. Anticancer Res. 2003 Sep-Oct;23: 4223-4227.
15. Portalez D, Malavaud B, Herigault G, et al. [Predicting prostate cancer with dynamic endorectal coil MR and proton spectroscopic MR imaging]. J Radiol. 2004 Dec;85: 1999-2004.
16. Scheidler J, Hricak H, Vigneron DB, et al. Prostate cancer: localization with three-dimensional proton MR spectroscopic imaging--clinicopathologic study. Radiology. 1999 Nov;213: 473-480.
17. Squillaci E, Manenti G, Mancino S, et al. MR spectroscopy of prostate cancer. Initial clinical experience. J Exp Clin Cancer Res. 2005 Dec;24: 523-530.
18. Vilanova JC, Barcelo J. Prostate cancer detection: MR spectroscopic imaging. Abdom Imaging. 2005 Dec 5.

19. Wefer AE, Hricak H, Vigneron DB, et al. Sextant localization of prostate cancer: comparison of sextant biopsy, magnetic resonance imaging and magnetic resonance spectroscopic imaging with step section histology. J Urol. 2000 Aug;164: 400-404.
20. Yu KK, Scheidler J, Hricak H, et al. Prostate cancer: prediction of extracapsular extension with endorectal MR imaging and three-dimensional proton MR spectroscopic imaging. Radiology. 1999 Nov;213: 481-488.
21. Wang L, Hricak H, Kattan MW, Chen HN, Scardino PT, Kuroiwa K. Prediction of organ-confined prostate cancer: incremental value of MR imaging and MR spectroscopic imaging to staging nomograms. Radiology. 2006 Feb;238: 597-603.
22. Kurhanewicz J, Vigneron DB, Males RG, Swanson MG, Yu KK, Hricak H. The prostate: MR imaging and spectroscopy. Present and future. Radiol Clin North Am. 2000 Jan;38: 115-138, viii-ix.
23. Zakian KL, Sircar K, Hricak H, et al. Correlation of proton MR spectroscopic imaging with gleason score based on step-section pathologic analysis after radical prostatectomy. Radiology. 2005 Mar;234: 804-814.
24. Pickett B, Kurhanewicz J, Fein B, Coakley F, Shinohara K, Roach M. Use of magnetic resonance imaging and spectroscopy in the evaluation of external beam radiation therapy for prostate cancer. Int J Radiat Oncol Biol Phys. 2003 Oct 1;57: S163-164.
25. Pickett B, Ten Haken RK, Kurhanewicz J, et al. Time to metabolic atrophy after permanent prostate seed implantation based on magnetic resonance spectroscopic imaging. Int J Radiat Oncol Biol Phys. 2004 Jul 1;59: 665-673.
26. Roach M, 3rd, Kurhanewicz J, Carroll P. Spectroscopy in prostate cancer: hope or hype? Oncology (Huntingt). 2001 Nov;15: 1399-1410; discussion 1415-1396, 1418.
27. Kurhanewicz J, Vigneron DB, Hricak H, et al. Prostate cancer: metabolic response to cryosurgery as detected with 3D H-1 MR spectroscopic imaging. Radiology. 1996;200: 489-496.
28. Mueller-Lisse UG, Swanson MG, Vigneron DB, et al. Time-dependent effects of hormone-deprivation therapy on prostate metabolism as detected by combined magnetic resonance imaging and 3D magnetic resonance spectroscopic imaging. Magnetic Resonance in Medicine. 2001;46: 49-57.
29. Mueller-Lisse UG, Vigneron DB, Hricak H, et al. Localized prostate cancer: effect of hormone deprivation therapy measured by using combined three-dimensional 1H MR spectroscopy and MR imaging: clinicopathologic case-controlled study. Radiology. 2001 Nov;221: 380-390.
30. Parivar F, Hricak H, Shinohara K, et al. Detection of locally recurrent prostate cancer after cryosurgery: evaluation by transrectal ultrasound, magnetic resonance imaging, and three-dimensional proton magnetic resonance spectroscopy. Urology. 1996;48(4): 594-599.
31. Parivar F, Kurhanewicz J. Detection of recurrent prostate cancer after Cryosurgery. Current Opinion in Urology. 1998;8: 83-86.
32. Coakley FV, Kurhanewicz J, Lu Y, et al. Prostate cancer tumor volume: measurement with endorectal MR and MR spectroscopic imaging. Radiology. 2002 Apr;223: 91-97.
33. Shukla-Dave A, Hricak H, Eberhardt SC, et al. Chronic prostatitis: MR imaging and 1H MR spectroscopic imaging findings--initial observations. Radiology. 2004 Jun;231: 717-724.

34. Zakian KL, Eberhardt S, Hricak H, et al. Transition zone prostate cancer: metabolic characteristics at 1H MR spectroscopic imaging--initial results. Radiology. 2003 Oct;229: 241-247.
35. Swanson MG, Vigneron DB, Tabatabai ZL, et al. Proton HR-MAS spectroscopy and quantitative pathologic analysis of MRI/3D-MRSI-targeted postsurgical prostate tissues. Magn Reson Med. 2003 Nov;50: 944-954.
36. Cheng LL, Wu CL, Smith MR, Gonzalez RG. Non-destructive quantitation of spermine in human prostate tissue samples using HRMAS H-1 NMR spectroscopy at 9.4 T. Febs Letters. 2001 APR 6;494: 112-116.
37. Cheng LL, Chang IW, Louis DN, Gonzalez RG. Correlation of high-resolution magic angle spinning proton magnetic resonance spectroscopy with histopathology of intact human brain tumor specimens. Cancer Research. 1998 MAY 1;58: 1825-1832.
38. Millis K, Weybright P, Campbell N, et al. Classification of human liposarcoma and lipoma using ex vivo proton NMR spectroscopy. Magnetic Resonance in Medicine. 1999 FEB;41: 257-267.
39. Taylor JL, Wu CL, Cory D, Gonzalez RG, Bielecki A, Cheng LL. High-resolution magic angle spinning proton NMR analysis of human prostate tissue with slow spinning rates. Magn Reson Med. 2003 Sep;50: 627-632.
40. Swanson MG, Zektzer AS, Tabatabai ZL, et al. Quantitative analysis of prostate metabolites using 1H HR-MAS spectroscopy. Magn Reson Med. 2006 Jun;55: 1257-1264.
41. Sitter B, Lundgren S, Bathen TF, Halgunset J, Fjosne HE, Gribbestad IS. Comparison of HR MAS MR spectroscopic profiles of breast cancer tissue with clinical parameters. Nmr in Biomedicine. 2006 FEB;19: 30-40.
42. Griffin JL, Blenkiron C, Valonen PK, Caldas C, Kauppinen RA. High-resolution magic angle spinning H-1 NMR spectroscopy and reverse transcription-PCR analysis of apoptosis in a rat glioma. Analytical Chemistry. 2006 MAR 1;78: 1546-1552.
43. Swindle P, McCredie S, Russell P, et al. Pathologic characterization of human prostate tissue with proton MR spectroscopy. Radiology. 2003 Jul;228: 144-151.
44. Cornel EB, Smits GA, Oosterhof GO, et al. Characterization of human prostate cancer, benign prostatic hyperplasia and normal prostate by in vitro 1H and 31P magnetic resonance spectroscopy. J Urol. 1993;150: 2019-2024.
45. Fowler AH, Pappas AA, Holder JC, et al. Differentiation of human prostate cancer from benign hypertrophy by in vitro 1H NMR. Magn Reson Med. 1992;25: 140-147.
46. Kurhanewicz J, Dahiya R, Macdonald JM, Chang LH, James TL, Narayan P. Citrate alterations in primary and metastatic human prostatic adenocarcinomas: 1H magnetic resonance spectroscopy and biochemical study. Magn Reson Med. 1993;29: 149-157.
47. Tessem M-B, Swanson MG, Keshari KR, et al. Evaluation of Lactate and Alanine as Metabolic Biomarkers of Prostate Cancer Using 1H HR-MAS Spectroscopy of Biopsy Tissues. Magn Reson Med. In press 2007.
48. Coakley FV, Hricak H. Radiologic anatomy of the prostate gland: a clinical approach. Radiol Clin North Am. 2000 Jan;38: 15-30.
49. Costello LC, Franklin RB. The intermediary metabolism of the prostate: a key to understanding the pathogenesis and progression of prostate malignancy. Oncology. 2000 Nov;59: 269-282.
50. Costello LC, Franklin RB. Novel role of zinc in the regulation of prostate citrate metabolism and its implications in prostate cancer. Prostate. 1998;35: 285-296.

51. Lahtonen R. Zinc and cadmium concentrations in whole tissue and in separated epithelium and stroma from human benign prostatic hypertrophic glands. Prostate. 1985;6: 177-183.
52. Franklin RB, Ma J, Zou J, et al. Human ZIP1 is a major zinc uptake transporter for the accumulation of zinc in prostate cells. J Inorg Biochem. 2003 Aug 1;96: 435-442.
53. Franklin RB, Feng P, Milon B, et al. hZIP1 zinc uptake transporter down regulation and zinc depletion in prostate cancer. Mol Cancer. 2005;4: 32.
54. Costello LC, Liu Y, Franklin RB, Kennedy MC. Zinc inhibition of mitochondrial aconitase and its importance in citrate metabolism of prostate epithelial cells. J Biol Chem. 1997;272: 28875-28881.
55. Costello LC, Franklin RB, Liu Y, Kennedy MC. Zinc causes a shift toward citrate at equilibrium of the m-aconitase reaction of prostate mitochondria. J Inorg Biochem. 2000 Jan 30;78: 161-165.
56. Halliday KR, Fenoglio PC, Sillerud LO. Differentiation of human tumors from nonmalignant tissue by natural-abundance 13C NMR spectroscopy. Magn Reson Med. 1988;7: 384-411.
57. Costello LC, Franklin RB. Concepts of citrate production and secretion by prostate. 1. Metabolic relationships. Prostate. 1991;18: 25-46.
58. Cooper JF, Farid I. The role of citric acid in the physiology of the prostate: III. lactate/citrate ratios in benign and malignant prostatic homogenates as an index of prostatic malignancy. J Urol. 1964;92: 533.
59. Liang JY, Liu YY, Zou J, Franklin RB, Costello LC, Feng P. Inhibitory effect of zinc on human prostatic carcinoma cell growth. Prostate. 1999;40: 200-207.
60. Costello LC, Franklin RB. Bioenergetic theory of prostate malignancy. Prostate. 1994;25: 162-166.
61. Rossi S, Graner E, Febbo P, et al. Fatty acid synthase expression defines distinct molecular signatures in prostate cancer. Mol Cancer Res. 2003 Aug;1: 707-715.
62. Costello LC, Franklin RB. 'Why do tumour cells glycolyse?': from glycolysis through citrate to lipogenesis. Mol Cell Biochem. 2005 Dec;280: 1-8.
63. Dahiya R, Boyle B, Goldberg BC, et al. Metastasis-associated alterations in phospholipids and fatty acids of human prostatic adenocarcinoma cell lines. Biochem Cell Biol. 1992;70: 548-554.
64. Dahiya R, Park HD, Cassafer G, Cusick J, Narayan P. Downregulation of saturated fatty acid and upregulation of unsaturated fatty acid by 13-cis-retinoic acid in human prostate cancer cells. Biochem Int. 1992;28: 981-987.
65. Dahiya R, Yoon WH, Boyle B, Schoenberg S, Yen TS, Narayan P. Biochemical, cytogenetic, and morphological characteristics of human primary and metastatic prostate cancer cell lines. Biochem Int. 1992;27: 567-577.
66. Oyama N, Akino H, Kanamaru H, Okada K. [Fluorodeoxyglucose positron emission tomography in diagnosis of untreated prostate cancer]. Nippon Rinsho. 1998 Aug;56: 2052-2055.
67. Kanamaru H, Oyama N, Akino H, Okada K. [Evaluation of prostate cancer using FDG-PET]. Hinyokika Kiyo. 2000 Nov;46: 851-853.
68. Warburg O, Wind F, Negelein E. Uber den Stoffwechsel von Tumouren im Korper. Klin Woch. 1926;5: 829-832.
69. Gatenby RA, Gillies RJ. Why do cancers have high aerobic glycolysis? Nat Rev Cancer. 2004 Nov;4: 891-899.
70. Laws DD, Bitter HM, Jerschow A. Solid-state NMR spectroscopic methods in chemistry. Angew Chem Int Ed Engl. 2002 Sep 2;41: 3096-3129.

71. Andrew ER. The narrowing of NMR spectra of solids by high-speed specimen rotation and the resolution of chemical shift and spin multiplet structures for solids. Progress in Nuclear Magnetic Resonance Spectroscopy. 1971;8: 1-39.
72. Lowe IJ. Free Induction Decays of Rotating Solids. Physical Review Letters. 1959;2: 285-287.
73. Andrew ER, Newing RA. The Narrowing of Nuclear Magnetic Resonance Spectra by Molecular Rotation in Solids. Proceedings of the Physical Society of London. 1958;72: 959-972.
74. Peehl DM. Culture of Human Prostatic Epithelial Cells. *In:* R. Fresney (ed.), Culture of Epithelial Cells, pp. 159-180. New York: Wiley-Liss, 1992.
75. Peehl DM. Primary cell cultures as models of prostate cancer development. Endocr Relat Cancer. 2005 Mar;12: 19-47.
76. Schwarze SR, Shi Y, Fu VX, Watson PA, Jarrard DF. Role of cyclin-dependent kinase inhibitors in the growth arrest at senescence in human prostate epithelial and uroepithelial cells. Oncogene. 2001 Dec 13;20: 8184-8192.
77. Parrish AR, Sallam K, Nyman DW, et al. Culturing precision-cut human prostate slices as an in vitro model of prostate pathobiology. Cell Biology and Toxicology. 2002;18: 205-219.
78. Akoka S, Trierweiler M. Improvement of the ERETIC method by digital synthesis of the signal and addition of a broadband antenna inside the NMR probe. Instrumentation Science & Technology. 2002;30: 21-29.
79. Ardenkjaer-Larsen JH, Fridlund B, Gram A, et al. Increase in signal-to-noise ratio of > 10,000 times in liquid-state NMR. Proc Natl Acad Sci U S A. 2003 Sep 2;100: 10158-10163.
80. Golman K, Ardenkjaer-Larsen JH, Petersson JS, Mansson S, Leunbach I. Molecular imaging with endogenous substances. Proc Natl Acad Sci U S A. 2003 Sep 2;100: 10435-10439.
81. Svensson J, Mansson S, Johansson E, Petersson JS, Olsson LE. Hyperpolarized 13C MR angiography using trueFISP. Magn Reson Med. 2003 Aug;50: 256-262.
82. Golman K, in 't Zandt R, Thaning M. Real-time metabolic imaging. Proc Natl Acad Sci U S A. 2006 Jul 25;103: 11270-11275.
83. Chen AP, Albers MJ, Cunningham CH, et al. Hyperpolarized C-13 spectroscopic imaging of the TRAMP mouse at 3T-initial experience. Magn Reson Med. 2007 Dec;58: 1099-1106.
84. Bowers CR, Weitekamp DP. Transformation of symmetrization order to nuclear-spin magnetization by chemical reaction and nuclear magnetic resonance. Phys Rev Lett. 1986 Nov 24;57: 2645-2648.
85. Bowers CR, Weitekamp DP. Para-Hydrogen and Synthesis Allow Dramatically Enhanced Nuclear Alignment. Journal of the American Chemical Society. 1987 Sep;109: 5541-5542.
86. Golman K, Axelsson O, Johannesson H, Mansson S, Olofsson C, Petersson JS. Parahydrogen-induced polarization in imaging: subsecond (13)C angiography. Magn Reson Med. 2001 Jul;46: 1-5.
87. Goldman M, Johannesson H, Axelsson O, Karlsson M. Hyperpolarization of 13C through order transfer from parahydrogen: a new contrast agent for MRI. Magn Reson Imaging. 2005 Feb;23: 153-157.
88. Golman K, Petersson JS. Metabolic imaging and other applications of hyperpolarized 13C. Acad Radiol. 2006 Aug;13: 932-942.

89. Johansson E, Mansson S, Wirestam R, et al. Cerebral perfusion assessment by bolus tracking using hyperpolarized 13C. Magn Reson Med. 2004 Mar;51: 464-472.
90. Kohler SJ, Yen Y, Wolber J, et al. In vivo (13)carbon metabolic imaging at 3T with hyperpolarized (13)C-1-pyruvate. Magn Reson Med. 2007 Jul;58: 65-69.
91. Golman K, Zandt RI, Lerche M, Pehrson R, Ardenkjaer-Larsen JH. Metabolic imaging by hyperpolarized 13C magnetic resonance imaging for in vivo tumor diagnosis. Cancer Res. 2006 Nov 15;66: 10855-10860.
92. Day SE, Kettunen MI, Gallagher FA, et al. Detecting tumor response to treatment using hyperpolarized (13)C magnetic resonance imaging and spectroscopy. Nat Med. 2007 Nov 13;13: 1382-1387.
93. Jonischkeit T, Bommerich U, Stadler J, Woelk K, Niessen HG, Bargon J. Generating long-lasting 1H and 13C hyperpolarization in small molecules with parahydrogen-induced polarization. J Chem Phys. 2006 May 28;124: 201109.
94. Burns MA, He W, Wu CL, Cheng LL. Quantitative pathology in tissue MR spectroscopy based human prostate metabolomics. Technol Cancer Res Treat. 2004 Dec;3: 591-598.
95. Pauli GF, Jaki BU, Lankin DC. Quantitative H-1 NMR: Development and potential of a method for natural products analysis. Journal of Natural Products. 2005 JAN;68: 133-149.
96. Kriat M, Confort-Gouny S, Vion-Dury J, Sciaky M, Viout P, Cozzone PJ. Quantitation of metabolites in human blood serum by proton magnetic resonance spectroscopy. A comparative study of the use of formate and TSP as concentration standards. NMR Biomed. 1992 Jul-Aug;5: 179-184.
97. Ziarelli F, Caldarelli S. Solid-state NMR as an analytical tool: Quantitative aspects. Solid State Nucl Magn Reson. 2006 Feb;29: 214-218.
98. Akoka S, Barantin L, Trierweiler M. Concentration measurement by proton NMR using the ERETIC method. Analytical Chemistry. 1999 JUL 1;71: 2554-2557.
99. Rabenstein DL, Keire DA. Quantitative Chemical Analysis by NMR. *In:* K. H. A. I. Popov (ed.), Modern NMR Techniques and Their Application in Chemistry, pp. 323-369. New York: Marcel Dekker, 1991.
100. Saito T, Nakaie S, Kinoshita M, et al. Practical guide for accurate quantitative solution state NMR analysis. Metrologia. 2004 Jun;41: 213-218.
101. Michel N, Akoka S. The application of the ERETIC method to 2D-NMR. J Magn Reson. 2004 May;168: 118-123.
102. Zwingmann C, Leibfritz D, Hazell AS. Brain energy metabolism in a sub-acute rat model of manganese neurotoxicity: an ex vivo nuclear magnetic resonance study using [1-13C]glucose. Neurotoxicology. 2004 Jun;25: 573-587.
103. Bluml S. In vivo quantitation of cerebral metabolite concentrations using natural abundance 13C MRS at 1.5 T. J Magn Reson. 1999 Feb;136: 219-225.
104. Hassel B, Sonnewald U, Fonnum F. Glial-neuronal interactions as studied by cerebral metabolism of [2-13C]acetate and [1-13C]glucose: an ex vivo 13C NMR spectroscopic study. J Neurochem. 1995 Jun;64: 2773-2782.
105. Mezzarobba V, Bielicki G, Jeffrey FM, et al. Lack of effect of ageing on acetate oxidation in rat skeletal muscle during starvation: a (13)C NMR study. J Exp Biol. 2000 Mar;203: 995-1001.
106. Portais JC, Voisin P, Merle M, Canioni P. Glucose and glutamine metabolism in C6 glioma cells studied by carbon 13 NMR. Biochimie. 1996;78: 155-164.
107. Kupce E, Freeman R. Adiabatic Pulses for Wideband Inversion and Broadband Decoupling. Journal of Magnetic Resonance, Series A. 1995;115: 273-276.

108. Kurhanewicz J, Vigneron DB, Nelson SJ, et al. Citrate as an in vivo marker to discriminate prostate cancer from benign prostatic hyperplasia and normal prostate peripheral zone: detection via localized proton spectroscopy. Urology. 1995 Mar;45: 459-466.
109. Schick F, Bongers H, Kurz S, Jung WI, Pfeffer M, Lutz O. Localized proton MR spectroscopy of citrate in vitro and of the human prostate in vivo at 1.5 T. Magn Reson Med. 1993 Jan;29: 38-43.
110. Cunningham CH, Vigneron DB, Marjanska M, et al. Sequence design for magnetic resonance spectroscopic imaging of prostate cancer at 3 T. Magn Reson Med. 2005 May;53: 1033-1039.
111. Swanson MG, Vigneron DB, Tran TK, Sailasuta N, Hurd RE, Kurhanewicz J. Single-voxel oversampled J-resolved spectroscopy of in vivo human prostate tissue. Magn Reson Med. 2001 Jun;45: 973-980.
112. Peehl DM, Stamey TA. Serial propagation of adult human prostatic epithelial cells with cholera toxin. In Vitro. 1984 Dec;20: 981-986.
113. Peehl DM, Wong ST, Terris MK, Stamey TA. Culture of prostatic epithelial cells from ultrasound-guided needle biopsies. Prostate. 1991;19: 141-147.
114. Yacoe ME, Sommer G, Peehl D. In vitro proton spectroscopy of normal and abnormal prostate. Magn Reson Med. 1991 Jun;19: 429-438.
115. Costello LC, Akuffo V, Franklin RB. Testosterone stimulates net citrate production from aspartate by prostate epithelial cells. Horm Metab Res. 1988 Apr;20: 252-253.
116. Franklin RB, Lao LX, Costello LC. Evidence for two aspartate transport systems in prostate epithelial cells. Prostate. 1990;16: 137-145.
117. Schiebler ML, Miyamoto KK, White M, Maygarden SJ, Mohler JL. In vitro high resolution 1H-spectroscopy of the human prostate: benign prostatic hyperplasia, normal peripheral zone and adenocarcinoma. Magn Reson Med. 1993 Mar;29: 285-291.
118. Hein DW, Leff MA, Ishibe N, et al. Association of prostate cancer with rapid N-acetyltransferase 1 (NAT1*10) in combination with slow N-acetyltransferase 2 acetylator genotypes in a pilot case-control study. Environ Mol Mutagen. 2002;40: 161-167.
119. Hein DW, Rustan TD, Bucher KD, Furman EJ, Martin WJ. Extrahepatic expression of the N-acetylation polymorphism toward arylamine carcinogens in tumor target organs of an inbred rat model. J Pharmacol Exp Ther. 1991 Jul 1;258: 232-236.
120. Wehrle JP, Ng CE, McGovern KA, et al. Metabolism of alternative substrates and the bioenergetic status of EMT6 tumor cell spheroids. NMR Biomed. 2000 Oct;13: 349-360.
121. Singer S, Okunieff P, Gostin C, Thilly WG, Chen LB, Neuringer LJ. 13C- and 31P-NMR studies of human colon cancer in-vitro and in-vivo. Surg Oncol. 1993;2: 7-18.
122. Costello LC, Franklin RB. The clinical relevance of the metabolism of prostate cancer; zinc and tumor suppression: connecting the dots. Mol Cancer. 2006;5: 17.
123. Costello LC, Franklin RB. Tumor cell metabolism: the marriage of molecular genetics and proteomics with cellular intermediary metabolism; proceed with caution! Mol Cancer. 2006;5: 59.
124. Costello LC, Franklin RB, Feng P. Mitochondrial function, zinc, and intermediary metabolism relationships in normal prostate and prostate cancer. Mitochondrion. 2005 Jun;5: 143-153.

125. Costello LC, Guan Z, Kukoyi B, Feng P, Franklin RB. Terminal oxidation and the effects of zinc in prostate versus liver mitochondria. Mitochondrion. 2004 Aug;4: 331-338.
126. Dakubo GD, Parr RL, Costello LC, Franklin RB, Thayer RE. Altered metabolism and mitochondrial genome in prostate cancer. J Clin Pathol. 2006 Jan;59: 10-16.
127. Singh KK, Desouki MM, Franklin RB, Costello LC. Mitochondrial aconitase and citrate metabolism in malignant and nonmalignant human prostate tissues. Mol Cancer. 2006;5: 14.
128. Chance EM, Seeholzer SH, Kobayashi K, Williamson JR. Mathematical analysis of isotope labeling in the citric acid cycle with applications to 13C NMR studies in perfused rat hearts. J Biol Chem. 1983 Nov 25;258: 13785-13794.
129. Malloy CR, Sherry AD, Jeffrey FM. Evaluation of carbon flux and substrate selection through alternate pathways involving the citric acid cycle of the heart by 13C NMR spectroscopy. J Biol Chem. 1988 May 25;263: 6964-6971.
130. Cohen DM, Bergman RN. Estimation of TCA cycle flux, aminotransferase flux, and anaplerosis in heart: validation with syntactic model. Am J Physiol. 1995 Mar;268: E397-409.
131. Mancuso A, Beardsley NJ, Wehrli S, Pickup S, Matschinsky FM, Glickson JD. Real-time detection of 13C NMR labeling kinetics in perfused EMT6 mouse mammary tumor cells and betaHC9 mouse insulinomas. Biotechnol Bioeng. 2004 Sep 30;87: 835-848.
132. Mancuso A, Zhu A, Beardsley NJ, Glickson JD, Wehrli S, Pickup S. Artificial tumor model suitable for monitoring 31P and 13C NMR spectroscopic changes during chemotherapy-induced apoptosis in human glioma cells. Magn Reson Med. 2005 Jul;54: 67-78.
133. Mochiki E, Kuwano H, Katoh H, Asao T, Oriuchi N, Endo K. Evaluation of 18F-2-deoxy-2-fluoro-D-glucose positron emission tomography for gastric cancer. World J Surg. 2004 Mar;28: 247-253.
134. Kunkel M, Reichert TE, Benz P, et al. Overexpression of Glut-1 and increased glucose metabolism in tumors are associated with a poor prognosis in patients with oral squamous cell carcinoma. Cancer. 2003 Feb 15;97: 1015-1024.
135. Gatenby RA, Gawlinski ET, Gmitro AF, Kaylor B, Gillies RJ. Acid-Mediated Tumor Invasion: a Multidisciplinary Study. Cancer Res. 2006 May 15, 2006;66: 5216-5223.
136. Moreadith RW, Lehninger AL. The pathways of glutamate and glutamine oxidation by tumor cell mitochondria. Role of mitochondrial NAD(P)+-dependent malic enzyme. J Biol Chem. 1984 May 25;259: 6215-6221.
137. DeBerardinis RJ, Mancuso A, Daikhin E, et al. Beyond aerobic glycolysis: transformed cells can engage in glutamine metabolism that exceeds the requirement for protein and nucleotide synthesis. Proc Natl Acad Sci U S A. 2007 Dec 4;104: 19345-19350.
138. Nelson SJ, Vigneron DB, Star-Lack J, Kurhanewicz J. High spatial resolution and speed in MRSI. NMR Biomed. 1997 Dec;10: 411-422.
139. Chen AP, Albers MJ, Cunningham CH, et al. High-Resolution Hyperpolarized C-13 Spectroscopic Imaging of TRAMP Mouse at 3T - Initial Experience. In press In press 2007.
140. Golman K, Olsson LE, Axelsson O, Mansson S, Karlsson M, Petersson JS. Molecular imaging using hyperpolarized 13C. Br J Radiol. 2003;76 Spec No 2: S118-127.
141. Mansson S, Johansson E, Magnusson P, et al. 13C imaging-a new diagnostic platform. Eur Radiol. 2006 Jan;16: 57-67.

142. Greenberg NM, DeMayo F, Finegold MJ, et al. Prostate cancer in a transgenic mouse. Proc Natl Acad Sci U S A. 1995;92: 3439-3443.
143. Cunningham CH, Chen AP, Albers MJ, et al. Double spin-echo sequence for rapid spectroscopic imaging of hyperpolarized (13)C. J Magn Reson. 2007 Aug;187: 357-362.
144. Department of Biochemistry. Biological Magnetic Resonance Data Bank [database on the Internet]. Madison, Wisconsin: University of Wisconsin. 2007 [updated 2007 Feb 28; cited 2007 May 1]. Available from: http://www.bmrb.wisc.edu/metabolomics/metabolomics_standards.html
145. Diggle PJ, Liang K-Y, Zeger SL. Parametric Models for Covariance Structure. p. 78-116. 1994.
146. Gingrich JR, Barrios RJ, Foster BA, Greenberg NM. Pathologic progression of autochthonous prostate cancer in the TRAMP model. Prostate Cancer Prostatic Dis. 1999 Mar;2: 70-75.
147. Lin RY, Vera JC, Chaganti RS, Golde DW. Human monocarboxylate transporter 2 (MCT2) is a high affinity pyruvate transporter. J Biol Chem. 1998 Oct 30;273: 28959-28965.

UCSF Library Release

Publishing Agreement

It is the policy of the University to encourage the distribution of all theses and dissertations. Copies of all UCSF theses and dissertations will be routed to the library via the Graduate Division. The library will make all theses and dissertations accessible to the public and will preserve these to the best of their abilities, in perpetuity.

Please sign the following statement:

I hereby grant permission to the Graduate Division of the University of California, San Francisco to release copies of my thesis or dissertation to the Campus Library to provide access and preservation, in whole or in part, in perpetuity.

Mark J Albers — Author Signature

4-1-2008 — Date